



מכון ויצמן למדע

WEIZMANN INSTITUTE OF SCIENCE

Thesis for the degree  
Doctor of Philosophy

עבודת גמר (תזה) לתואר  
דוקטור לפילוסופיה

Submitted to the Scientific  
Council of the  
Weizmann Institute of Science  
Rehovot, Israel

מוגשת למועצה המדעית של  
מכון ויצמן למדע  
רחובות, ישראל

By  
Dan Shaked Renous

מאת  
דן שקד רנו

חקירת קלורימטר הדרוני דיגיטלי מבוסס על גלאי מסוג RPWELL  
Investigation of RPWELL-based Digital Hadronic Calorimeter

Advisor: Shikma Bressler

מנחה: שקמה ברסלר

January 2022

שבט תשפ"ב



*To my guiding light,  
my precious family,  
Lior and Sophie.*



## Declaration

I declare that the presented work summarizes my independent research.

The entire work was conducted in collaboration with colleagues from Weizmann Institute of Science (WIS) and Laboratoire d'Annecy de Physique des Particules (LAPP). In particular:

- I was involved in developing and assembling all the large area RPWELL prototypes, except for Prototype I, which was designed and assembled by Dr. Luca Moleri, Dr. Artur Coimbra, and Dr. Purba Bhattacharya. Dr. Luca Moleri, Dr. Purba Bhattacharya, and I assembled all the other prototypes.
- I executed all the test beam campaigns with Dr. Luca Moleri and Dr. Purba Bhattacharya. Dr. Enrique Kajomovitz Must participated in the test beam of April 2018, and Andrea Tesi joined in November 2018.
- Our colleagues from LAPP (Dr. Max Chefdeville, Cyril Drancourt, and Guillaume Vouters) designed and delivered us the MICROROC-embedded ASU, their firmware, and analysis framework. They also supported us in the operations of the RPWELL DHCAL sampling elements in the test beam and operated with us the small MPGD DHCAL module in November 2018.
- Dr. Max Chefdeville provided the GEANT4 simulation code for the calorimeter modeling. I modified it for our needs and wrote the detector response simulator and its analysis.



## Acknowledgments

I would like to express my deep gratitude to all of those who advised, supported, and helped me carry out this thesis.

I would first like to thank my advisor, **Shikma Bressler**. Without her trust, help, encouragement, patience, and expertise in the field of particle detectors and data analysis, this thesis would not have been possible.

I am also profoundly grateful to **Amos Breskin**, for the kind conversations and his unsurpassed knowledge in the field of radiation and radiation detection physics.

I would like to thank **Max Chefdeville** for the inspiring pleasant collaboration, guidance, and assistance in our joint project and **Cyril Drancourt** and **Guillaume Vouters** for their technical support.

To my colleagues from the WIS, who provided me with support, despite my distant location: to **Luca Moleri** and **Purba Battacharia** for their professional and personal support; to **Eran Erdal**, **Arindam Roy**, **Abhik Jash**, **Andrea Tesi**, **Darina Zavazieva**, and **David Vartsky**, for the valuable conversations; and to **Jonathan Shlomi** and **Sanmay Ganguly**, for sharing with me the secrets of deep learning architectures, I am deeply grateful.

Distant from my home institute, the members of the GDD lab at CERN accepted me to their group and provided me with a second home. I thank **Leszek Ropelewski**, **Eraldo Oliveri**, **Florian Brunbauer**, **Lucian Scharenberg**, **Hans Müller**, **Djunes Janssens**, **Jerome Samarati**, **Dorothea Pfeifer**, **Antonija Utrobičić**, **Rob Veenhof**, **Miranda van Stenis**, **Marta Lisowska**, and **Fabio Sauli** for their warm and kind welcome, their invaluable knowledge, and support.

This research would not have been possible without the financial, academic, and technical support of the Weizmann Institute of Science and of the Particle Physics Department and its staff and the financial assistance of the Chateaubriand Fellowship given by the French Embassy in Israel.

The most grateful acknowledgment goes to my family; to my parents, **Ludovic (Eliezer)** and **Tzila Mandel**, for providing me the support, confidence, and tools to pave my own path; to my parents-in-law **Raphael** and **Silvia Renous**, for the endless encouragement and advice; and most importantly to my wife **Lior**, for lovingly, encouraging, and supporting me every step of the way, and my daughter **Sophia**, for filling my heart with love and reminding me of the importance of playfulness.



## Abstract

In search for beyond the standard model of physics, the foreseen program of the high-energy physics community relies on precision measurements of the Higgs, W, and Z bosons, also in their hadronic decay modes. Thus, future collider experiments would need jet energy resolution superior to the one measured in today's state-of-the-art experiments. Particle flow, i.e., the measurement of each particle separately, is one of the leading approaches studied in this context. It requires high granular detectors and, among others, motivates the development of digital hadronic calorimeter (DHCAL). The DHCAL concept was mostly studied with sampling elements based on Resistive Plate Chambers (RPC). However, recent studies focusing on sampling elements based on Micro-Pattern Gaseous Detector (MPGD) have shown their potential advantages compared to the RPC.

The presented thesis is a part of an ongoing R&D effort towards a particle flow DHCAL based on the Resistive Plate WELL (RPWELL) detector. Our group at WIS has already demonstrated that RPWELL-based sampling elements could meet the DHCAL requirements. It was operated with an environment-friendly gas mixture in test beams of muons and high-rate pion beam, demonstrating 1.1 average pad-multiplicity at 98% MIP detection efficiency in discharge-free conditions.

In this work, we developed, built, and tested the first large ( $50 \times 50$  cm<sup>2</sup>) RPWELL detector with full coverage (no dead area in the gas volume). After demonstrating the effective coupling of the RPWELL to a semi-digital readout system, we could operate the first small MPGD-based DHCAL prototype. This prototype, comprising RPWELL- and Micromegas based-sampling elements, was tested in low energy (2–6 GeV) pion beam; the collected data enabled validating a GEANT4-based DHCAL simulation framework that we developed.

Using that simulation framework, we estimated the expected performance of a 50-layers RPWELL-based DHCAL module. It was tested with pions at the energy of 6-36 GeV, yielding a relative pion energy resolution of  $\frac{\sigma}{E[\text{GeV}]} = \frac{(50.8 \pm 0.3)\%}{\sqrt{E[\text{GeV}]}} \oplus (10.3 \pm 0.06)\%$ , assuming 98% MIP detection efficiency and 1.1 average pad-multiplicity. Thus, suggesting that an optimal RPWELL-based DHCAL could enable the targeted jet-energy resolution using particle flow calorimetry.



# Table of Contents

|  |     |
|--|-----|
| Table of Contents .....  | xi  |
| List of Abbreviations .....  | xiv |
| Chapter 1: Introduction.....   | 19  |
| Chapter 2: Scientific Background .....                                       | 22  |
| 2.1 Detection of Relativistic Particles.....                                 | 22  |
| 2.1.1 Interaction of Relativistic Particles with Matter .....                | 22  |
| Electrically Charged Heavy Particles .....                                   | 23  |
| Electrons and Photons.....   | 24  |
| Hadrons.....   | 25  |
| 2.1.2 Particle Identification in Multi-Purpose Collider Experiments .....    | 26  |
| 2.2 Hadronic Calorimeters .....  | 27  |
| 2.2.1 Particle flow Calorimetry .....  | 28  |
| Analog HCAL (AHCAL) .....  | 30  |
| Digital HCAL (DHCAL) and Semi-Digital HCAL (SDHCAL) .....                    | 32  |
| 2.3 The Resistive-Plate WELL for DHCAL.....                                  | 34  |
| 2.3.1 The Resistive-Plate WELL .....   | 34  |
| 2.3.2 RPWELL as a DHCAL Sampling Element.....                                | 35  |
| 2.3.3 Small MPGD-based DHCAL Prototype.....                                  | 36  |
| Chapter 3: The Development of Large Area RPWELL Sampling Elements .....      | 37  |
| 3.1 RPWELL prototypes with analog strips readout (Prototypes I-III).....     | 38  |
| 3.1.1 Experimental setup .....   | 38  |
| 3.1.2 Prototype I – Mechanical Coupling.....                                 | 39  |
| 3.1.3 Prototype II – Adhesive Coupling (Spray) .....                         | 40  |
| 3.1.4 Prototype III – Adhesive Coupling (Epoxy).....                         | 42  |
| 3.2 RPWELL with Semi-Digital Pads Readout.....                               | 43  |
| 3.2.1 Experimental Setup and Methodology .....                               | 43  |
| The MICROROC/ASU Semi-Digital Readout System.....                            | 43  |
| Experimental setup .....   | 45  |
| Event Cleaning.....  | 46  |
| Methods for MIP Detection Efficiency and Pad-Multiplicity measurements ..... | 46  |
| 3.2.2 Results.....   | 47  |
| 3.3 Discussion and Conclusions .....   | 50  |
| Chapter 4: A Study of a Small MPGD-based DHCAL .....                         | 51  |

|             |  |    |
|-------------|--|----|
| 4.1         | Experimental Setup and Methodology .....                               | 51 |
| 4.1.1       | Experimental Setup.....  | 51 |
| 4.1.2       | Data sample .....  | 52 |
| 4.1.3       | Measuring Detection Efficiency and Pad-Multiplicity .....              | 53 |
| 4.2         | Simulation Framework .....   | 54 |
| 4.2.1       | Calorimeter Modeling.....  | 55 |
| 4.2.2       | Physics Modeling of Pion interactions .....                            | 55 |
| 4.2.3       | Digitization – from Energy Deposits to Digital Signals .....           | 56 |
| 4.2.4       | Validation Methodology .....   | 56 |
| 4.3         | Results.....   | 57 |
| 4.3.1       | Examples of Recorded Events .....                                      | 57 |
| 4.3.2       | Experimental Data vs. Simulation .....                                 | 58 |
| 4.4         | Discussion and Conclusions .....                                       | 62 |
| Chapter 5:  | A Simulation Study of a 50-layers RPWELL-based DHCAL module .....      | 63 |
| 5.1         | Methodology.....   | 63 |
| 5.1.1       | Event selection.....   | 63 |
| 5.1.2       | Energy Reconstruction and Energy Resolution .....                      | 64 |
| 5.1.3       | Uncertainty Estimation .....   | 65 |
| 5.2         | Results.....   | 66 |
| 5.2.1       | An Optimal RPWELL-based DHCAL .....                                    | 66 |
| 5.2.2       | The Effect of MIP Detection Efficiency .....                           | 68 |
| 5.2.3       | The Effect of Pad-Multiplicity.....                                    | 72 |
| 5.3         | Discussion.....  | 73 |
| Chapter 6:  | Conclusions and Outlook.....   | 77 |
| References  | .....  | 81 |
| Appendix A: | Large Area Precision Cathode Boards for ATLAS NSW .....                | 87 |
| Appendix B: | 50×50 cm <sup>2</sup> RPWELL Prototypes Construction Procedure .....   | 93 |
| Appendix C: | Calculation of True Pad-Multiplicity and Hit Detection Efficiency..... | 97 |



# List of Abbreviations

|          |   |
|----------|---|
| ASU      | Active Sensor Unit                              |
| BERT     | Bertini cascade model                           |
| BR       | Branching Ratio                                 |
| BSM      | Beyond the Standard Model                       |
| CEPC     | Circular Electron-Positron Collider             |
| CERN     | the European Organization for Nuclear Research  |
| CLIC     | Compact Linear Collider                         |
| DAQ      | Data Acquisition                                |
| DCC      | Clock-Cycle Distributor                         |
| DHCAL    | Digital Hadronic Calorimeter                    |
| DIF      | Detector Interface Card                         |
| DL       | Deep Learning                                   |
| ECAL     | Electromagnetic Calorimeter                     |
| HCAL     | Hadronic Calorimeter                            |
| EM       | Electromagnetic                                 |
| FCC      | Future Circular Collider                        |
| FTFP     | Fritiof Pre-Compound model                      |
| GEM      | Gaseous Electron Multiplier                     |
| HEP      | High-Energy Physics                             |
| HL-LHC   | High-Luminosity Large Hadron Collider           |
| ILC      | International Linear Collider                   |
| LAPP     | Laboratoire d'Annecy de Physique des Particules |
| LHC      | Large Hadron Collider                           |
| MC       | Monte Carlo                                     |
| MICROROC | Micro-Mesh gaseous structure Readout Chip       |
| MIP      | Minimum Ionizing Particle                       |
| MM       | Micro-Mesh gaseous structure (Micromegas)       |
| MPGD     | Micro-Pattern Gaseous Detector                  |
| NSW      | New Small Wheel                                 |

|        |  |
|--------|--|
| PCB    | Printable Circuit Board                        |
| PS     | Proton-Synchrotron                             |
| QGSP   | Quark-Gluon String Pre-Compound model          |
| SCREAM | Sampling Calorimetry with Resistive Anode MPGD |
| SDHCAL | Semi-Digital Hadronic Calorimeter              |
| SM     | Standard Model                                 |
| SPS    | Super Proton-Synchrotron                       |
| SRS    | Scalable Readout System                        |
| sTGC   | small-strip Thin Gap Chamber                   |
| SW     | Small Wheel                                    |
| RAM    | Random Access Memory                           |
| RICH   | Ring Imaging Cherenkov                         |
| RP     | Resistive-Plate                                |
| RPC    | Resistive-Plate Chamber                        |
| RPWELL | Resistive-Plate WELL                           |
| THGEM  | Thick Gaseous Electron Multiplier              |
| TGC    | Thin Gap Chamber                               |
| QCD    | Quantum Chromo-Dynamic                         |
| WIS    | Weizmann Institute of Science                  |
| ZSF    | Zero Suppression Factor                        |







# Chapter 1: Introduction

Despite its success in describing the elementary particles and their interactions, the Standard Model (SM) is still incomplete, e.g., it does not account for neutrino masses, baryon asymmetry, or dark matter. These shortcomings indicate that the SM must be extended. Thus, the discovery of physics beyond the Standard Model (BSM) is the holy grail of particle physics. The many (hundreds) searches for BSM scenarios, particularly in the general-purpose experiments, ATLAS and CMS, in the Large Hadron Collider (LHC), have not shown to date deviations from the SM predictions.

Precise measurements of the properties of the Higgs boson and the weak interaction bosons, W and Z, are a key ingredient in the foreseen high-energy physics (HEP) program [1]. These could deviate from their SM predicted values hinting towards the nature of the BSM physics. An improved precision, yielding sensitivity to new scenarios, is foreseen with the High Luminosity LHC (HL-LHC) data [2], thus motivating the ongoing upgrade programs of the LHC experiments, including ATLAS [3]. Among others, the first station of the ATLAS muon end-cap system, the two Small Wheels (SW), were replaced in 2021 with two new ones (NSW), each comprising two detector technologies: the small-strip Thin Gap Chambers (sTGC), and the Micro-Mesh Gaseous Structure (Micromegas, MM) [4]. My contribution to the project is further discussed in Appendix A:

Nonetheless, it is already clear that, even with upgraded detectors, the HL-LHC would not be sufficient. The large quantum chromo-dynamic (QCD) background in a hadron collider inherently reduces the sensitivity for measuring the coupling of the Higgs to certain quarks and gluons [5]. These considerations motivate the development of future electron-positron colliders such as the International Linear Collider (ILC) [6], the Compact Linear Collider (CLIC) [7], the Circular Electron-Positron Collider (CEPC) [8], and the Electron-Positron Future Circular Collider (e-e+-FCC) [9]. These will allow reaching a precision higher than the one foreseen at the HL-LHC in some of the key channels and cover larger areas in the parameter space of BSM physics.

The development of new accelerators goes along with that of advanced detectors and instrumentations, without which the potential of these accelerators cannot be fully exploited. Since many scenarios of BSM physics involve hadronic-decay channels, efforts are made to develop modern calorimetric systems. Traditionally, the performance of these systems is characterized in terms of the jet energy resolution; where

a jet is a collimated bundle of particles produced by the hadronization of a quark or a gluon. The target calorimeter performance is currently driven by the requirement for good separation between the W and Z masses in their hadronic decay mode. The targeted relative jet energy resolution is set to at least  $30\%/\sqrt{E_{jet}[GeV]}$ , which corresponds to 3% for 100 GeV jets (see for example [6]) – close to the resolution of the ZEUS calorimetric system [10] and more than two times better than the one measured with the ATLAS and CMS calorimeters [11, 12]. This improved resolution will allow measuring the Branching Ratio (BR) of the Higgs boson’s decay to Z and W with a precision better than 1.9% and 0.44%, respectively [5].

Traditionally, the jet energy is measured as a whole in the electromagnetic and hadronic calorimetry systems (ECAL and HCAL, respectively). Its resolution is limited by the intrinsically poor energy resolution of the HCAL, where  $\sim 70\%$  of total jet energy is measured.

Particle flow [13] is the leading approach towards reaching the required jet energy resolution. It is based on the observation that over 60% of the jet particles are charged hadrons. Hence the tracking system can measure their energy, through their momenta, with higher precision than the HCAL, leaving only the neutral hadrons ( $\sim 10\%$  of the jet energy) to be measured by the HCAL. In the last few years, the particle flow approach to jet-energy measurement has received considerable attention; it is now used by both ATLAS and CMS collaborations and proved to be superior to other techniques in all terms. It is also the subject of development by practically all development groups of future experiments. Particle flow calorimetry systems aim to identify charged particles and associate their energy deposits in the calorimeter with their corresponding tracks in the tracking system. This task requires high transverse and longitudinal granularity for the calorimetry system. It allows discarding the energy deposited by charged particles from the calorimeter measurements, leaving the HCAL to measure only the energy deposits associated with neutral hadrons.

The community working on future particle flow calorimeters (CALICE [14]) develops in parallel HCAL with two different readout concepts: analog (AHCAL) and digital (DHCAL). The AHCAL measures all the energy deposited through electromagnetic (EM) interactions in the HCAL. However, an analog readout (12-bit ADC [15]) is costly – potentially limiting the granularity of the HCAL. On the other hand, a digital readout (1-bit ADC) is cost-effective; thus, a DHCAL can have very high granularity. The digital readout channels record only the existence of measured signals above a predefined threshold (hits) – i.e., a 1-bit ADC information indicates only “hit” or “no-hit”. The DHCAL energy measurement relies on the

underlying assumption of an approximately linear relationship between the energy deposited by a traversing particle and the number of recorded hits. Non-linear effects in the hadronic response are observed at all energies, resulting in degraded energy resolution for high energy hadrons (above 100 GeV).

A typical DHCAL is a sampling calorimeter; i.e., it consists of alternating layers of absorbers and sampling elements. Hadronic showers are primarily formed in the absorber, of which the material defines the total calorimeter's depth. The resulting signals are measured by sampling elements, typically with pad readout. In this work, we studied the Resistive-Plate WELL (RPWELL) detector as a candidate for a DHCAL sampling element. The RPWELL [16] is a robust, industrially mass-produced, single-stage gas-avalanche detector. With a discharge-free operation in harsh radiation conditions, wide dynamic range, close-to-unity MIP detection efficiency, and  $\sim 200 \mu\text{m}$  RMS resolution [17–19], it is an attractive candidate for particle tracking over large-area coverage. As a few-millimeter thin detector, it could become a candidate of choice as a sampling element for (S)DHCAL. While we evaluate the performance of a single sampling element by its efficiency and average pad-multiplicity, the benchmark for assessing the DHCAL performance is the expected single hadron energy resolution, following [20].

The structure of the document is as follows: Chapter 2 presents a brief introduction to the scientific background upon which this work relies. It consists of an introduction to the detection of relativistic particles (section 2.1), hadronic calorimeters (section 2.2), and the performance of the RPWELL detector in the context of DHCAL (section 2.3). The main results of the thesis are presented in Chapters 3–5. Chapter 3 details the development of large ( $50 \times 50 \text{ cm}^2$ ) area RPWELL sampling elements; Chapter 4 describes the first study of a small Micro-Pattern Gaseous Detector (MPGD) based DHCAL; and Chapter 5 reports on a simulation study of a 50-layers RPWELL-based DHCAL module. Chapter 6 concludes this thesis, presenting its main achievements and the outlook of future work in the context of DHCAL R&D.

## Chapter 2: Scientific Background

This chapter briefly introduces the scientific foundations on which the presented research relies. Section 2.1 describes the detection of relativistic particles in multi-purpose high-energy collider experiments. Section 2.2 presents the concept of hadronic calorimetry, the challenges of jet energy measurement, and the proposed particle flow calorimetry solutions. Finally, section 2.3 introduces the RPWELL as a candidate technology for a DHCAL sampling element. This section includes a description of the RPWELL concept and its performance in the context of a DHCAL sampling element, followed by the geometrical requirements set for a first MPGD-based DHCAL.

### 2.1 Detection of Relativistic Particles

Particles are detected by interacting with the detector's material when part of their energy is deposited in EM interactions inducing a measurable signal. In this section, we focus on the interactions relevant to our research.

#### 2.1.1 Interaction of Relativistic Particles with Matter

The physics processes that govern the interaction of particles with matter depend on their type and energy. Following [21], Relativistic heavy charged particles lose their energy through ionization, bremsstrahlung, and Cherenkov radiation. Relativistic electrons and positrons lose their energy through ionization, bremsstrahlung, Cherenkov radiation, Møller scattering, Bhabha scattering, and  $e^+e^-$  annihilation. Photons lose all their energy in single interaction processes like the photoelectric effect, Compton scattering, Rayleigh scattering, photonuclear absorption, and  $e^+e^-$  pair production. In addition, Hadrons can also deposit their energy via nuclear interactions [22]. The following subsections describe the main processes by which relativistic particles deposit their energies when traversing through matter – ionization, bremsstrahlung, Cherenkov radiation, pair production, and nuclear interactions. Table 2.1 summarizes the variables used throughout this section.

**Table 2.1:** Summary of the variable used in section 2.1.1 [21]

| Symbol                | Definition  | Value or Units                                  |
|-----------------------|---|---|
| $M$                   | Traversing particle mass  |   |
| $m_e$                 | Electron mass   | $\approx 0.51 \text{ MeV}$                      |
| $\beta$               | Relativistic velocity $v/c$   |   |
| $\gamma$              | Lorentz factor $(1 - \beta^2)^{-2}$   |   |
| $p$                   | particle's momentum   |   |
| $K$                   | $\langle \frac{dE}{dx} \rangle$ coefficient: $4\pi N_A r_e^2 m_e c^2$   | $0.307 \text{ MeV g}^{-1} \text{ cm}^2$         |
| $N_A$                 | Avogadro's number   | $\approx 6.022 \times 10^{23} \text{ mol}^{-1}$ |
| $r_e$                 | Classical electron radius   | $\approx 2.82 \text{ fm}$                       |
| $z$                   | charge number of incident particle  |   |
| $Z$                   | atomic number of medium   |   |
| $A$                   | atomic mass of medium   | $\text{g mol}^{-1}$                             |
| $T_{max}$             | Maximum energy transfer to an electron in single collision:<br>$\frac{2m_e c^2 \beta^2 \gamma^2}{1 + \frac{2\gamma m_e}{M} + \left(\frac{m_e}{M}\right)^2}$ | MeV   |
| $I$                   | mean excitation energy of medium  | $\approx (10 \text{ eV}) \cdot Z$               |
| $\delta(\beta\gamma)$ | density effect correction to ionization energy loss   |   |

## Electrically Charged Heavy Particles

Electrically charged heavy ( $M \gg m_e$ ) particles interact electromagnetically with matter through ionization and excitation of the atoms. The mean rate of energy loss of such particles by these interactions, known also as the *stopping power*, is approximated by the Bethe-Bloch equation (1) [21].

$$\left\langle \frac{dE}{dx} \right\rangle = -Kz^2 \frac{Z}{A\beta^2} \left[ \frac{1}{2} \ln \frac{2m_e c^2 \beta^2 \gamma^2 T_{max}}{I^2} - \beta^2 - \frac{\delta(\beta\gamma)}{2} \right] \quad (1)$$

This approximation is valid for particles with momentum in the range of  $0.1 \lesssim \beta\gamma = p/Mc \lesssim 1000$ . The stopping power reaches a minimum around  $\beta\gamma \approx 3$ , corresponding to  $\sim 400 \text{ MeV}/c$  pions and muons (Figure 1). Charged particles that lose their energy at this minimum are called minimum ionizing particles (MIPs). The energy deposited along a unit length by a MIP of a fixed energy is distributed according to the Landau distribution. An example of the energy loss distribution of 500 MeV pions in silicon layers of different thicknesses is shown in Figure 22. It demonstrates that the most probable energy loss is much lower than the mean given by eq. 1. MIP tracks are typically reconstructed from the position of their energy deposits.

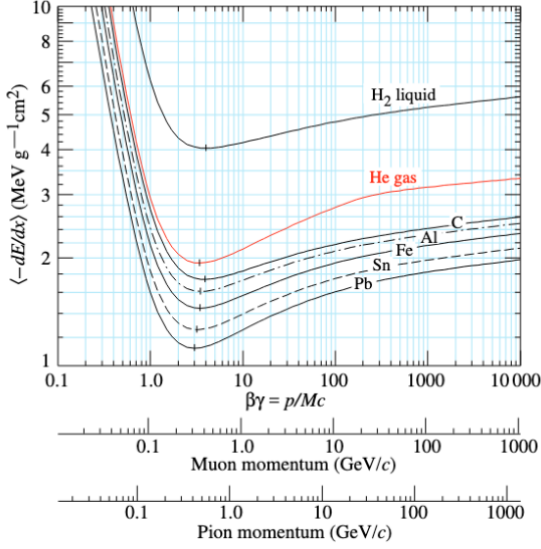


**Figure 1:** Mean rate of energy loss in different media, radiative effects, relevant for muons and pions, are not included. [21]

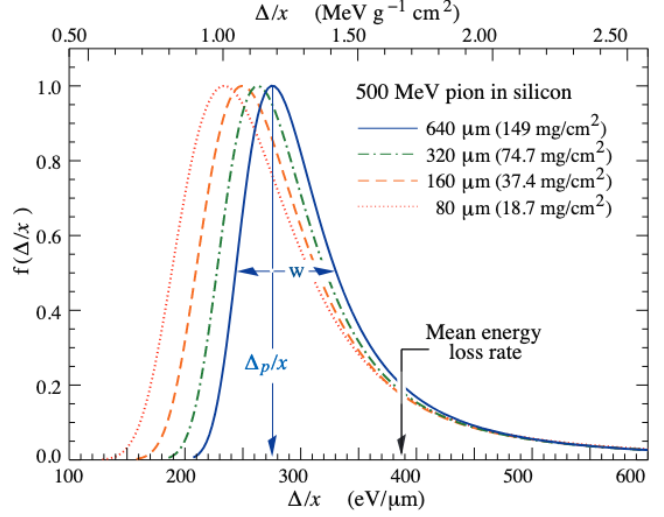


**Figure 22:** Energy loss distribution in silicon for 500 MeV pions, normalized to unity at the most probable value  $\Delta_p/x$ . The width  $w$  is the full width at half maximum. [21]

Charged particle traversing a medium of refractive index  $n$  at speed higher than the phase velocity of light in that medium ( $c/n$ ) emits Cherenkov radiation [21]. This radiation forms a cone with an opening angle of  $\theta_c$  in the direction of the particle's motion. This angle is related to the particle's velocity ( $\beta$ ) following:

$$\cos \theta_c = \frac{1}{n\beta} \quad (2)$$

The energy loss of the emitting particle caused by the Cherenkov radiation is negligible; however, it is very useful for particle identification.

## Electrons and Photons

Electrons and positrons mainly lose energy by ionization and bremsstrahlung (stopping radiation) emission. Other processes, such as the Møller and Bhabha scatterings and annihilation, have lower probability [21]. The mean distance over which a high-energy electron loses about 64% ( $1/e$ ) of its energy by bremsstrahlung is called *the radiation length* (denoted by  $X_0$ ) and measured in  $g \cdot \text{cm}^{-2}$ . The radiation length can be approximated [22] by

$$X_0 = \frac{716.4 A}{Z(Z + 1) \ln(237/\sqrt{Z})} \quad (3)$$

The energy loss through ionization rises logarithmically with the electron energy, while the bremsstrahlung rate rises nearly linearly. The *critical energy* ( $E_c$ ) is the one from which the bremsstrahlung processes are more dominant than ionization. In most materials, it stands on a few tens of MeV.

Photons are detected indirectly, producing electrons and, sometimes, positrons, which interact electromagnetically with the matter. The main processes at photon energy lower than a few MeV are the photoelectric effect and Compton scattering, above which the electron-positron pair production dominates. The pair production, also called *photon conversion*, usually occurs in the EM field of the matter's nucleus or, with a lower probability, in the one of an atom's electron. This process is the main energy deposition of high-energy photons.

High energy electrons (or positrons) and photons traversing a certain material volume will most likely initiate successive alternations of bremsstrahlung emission and pair production, leading to an EM cascade known as EM shower. As the shower develops, the number of particles multiplies until the dominant energy loss is due to ionization for electrons. This shower development transition occurs as the energy of the shower fragments reaches the critical energy, which is lower for larger  $Z$  materials [21]. The critical energy and the radiation length allow the expression of the radius of a cylindrical volume around the shower axis, where ~85-90% of the shower energy is deposited. This radius is called the Molière radius ( $\rho_M$ ) and is expressed by:

$$\rho_M = E_s \frac{X_0}{E_c}; \quad E_s = m_e c \sqrt{\frac{4\pi}{\alpha}} = 21.2 \text{ MeV} \quad (4)$$

## Hadrons

Hadrons traversing matter mainly interact through inelastic strong interactions. High-energy charged hadrons can also lose energy through ionization and excitation, like a MIP (subsection 0), while neutral hadrons have no EM interactions. The nuclear interaction length ( $\lambda_{int}$ ) of a medium is defined as the average distance that an energetic hadron travels inside that medium before a nuclear interaction occurs.

This value depends on the hadron size, such that protons, for example, have shorter interaction length ( $\lambda_p$ ) than pions ( $\lambda_\pi$ ).

The nuclear interactions produce numerous secondary particles (subject to large statistical fluctuations). The majority of them are charged and neutral pions ( $\pi^\pm$  and  $\pi^0$ ) and  $\eta$ . Protons and neutrons can also be released by nuclear reactions. Except for  $\pi^0$  and  $\eta$ , the secondary hadrons traverse the medium until they participate in another nuclear interaction and produce more particles. In nuclear interactions, a large portion of the energy is deposited in nuclei excitation and recoils or absorbed in nuclear binding energy. This *invisible energy* is fundamentally undetectable.

About a third of the secondary particles consist of  $\pi^0$  or  $\eta$  which decay instantly to photons (BRs of 99% and 72%, respectively [21]). The energy carried in these decays is deposited in EM showers. The fraction of the EM component within the hadronic shower highly fluctuates and varies for different types of hadrons. The significant fluctuations of the invisible energy and the fraction of energy deposited in EM showers deteriorate the performance of hadronic calorimeters, as discussed in section 2.2.

### 2.1.2 Particle Identification in Multi-Purpose Collider Experiments

Multi-purpose collider experiments measure directly only particles that are stable or live long enough to interact with the detectors: electrons, muons, photons, protons, neutrons, and light-charged mesons (pions and kaons). Their identification is possible due to the characteristic signature each of them has in the experiment.

Sorted by their distance from the interaction point, a typical multi-purpose collider experiment comprises of the following subsystems:

1. Tracking system – in which charged particles interact electromagnetically with the detectors and leave a set of hits that are later reconstructed into tracks.
2. ECAL – in which electrons, positrons, and photons are prone to deposit all their energy in an EM shower.
3. HCAL – in which hadrons deposit their energy in hadronic showers.
4. Muon spectrometer – a second tracking system to which the muons are the only particles to arrive.

The distinctive signature of each of the directly measured particles is shown in Figure 3. As can be seen, in the ideal case, the unique subdetectors arrangement provides a clear separation between the different particles. Photons will interact only with the ECAL, while electrons will be visible also in the tracker;

neutral hadrons will be visible in the HCAL, while the charged hadrons will also leave a trajectory in the tracker and ECAL. Finally, the muons will show a continuous trajectory through all the detector subsystems.

This particle identification scheme is applicable to isolated particles. Its performance degrades in the presence of nearby and overlapping trajectories. This is often the case in the presence of jets. Thus, as discussed in section 2.2, in traditional HEP experiments, each jet is measured as a single object, and the jet energy is measured in the calorimeters.

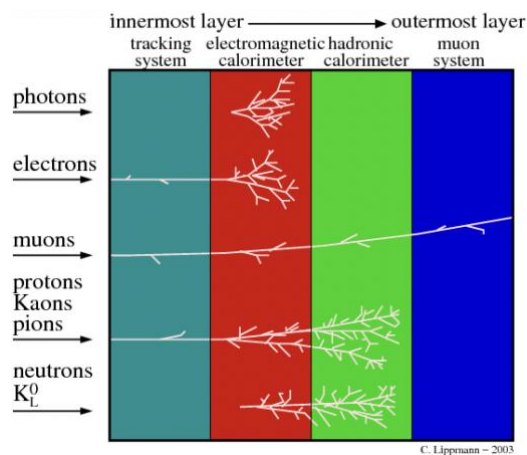


**Figure 3:** Schematic description of particle identification in a typical multipurpose particle experiment. [80].

## 2.2 Hadronic Calorimeters

The term calorimetry in particle physics refers to the measurement of particles' energy through their total absorption in a material. There are two types of calorimeters: homogenous and sampling calorimeters. A homogenous calorimeter contains a single material block that completely absorbs the particle's energy. A sampling calorimeter consists of alternating layers of absorber planes and readout elements that sample the deposited energy. The absorber serves as a dense medium that facilitates the formation of EM or hadronic showers and determines most of the total calorimeter's depth. The sampling elements sample the particles produced in the showers. The transverse granularity of the calorimeter is defined by the readout granularity of the sampling elements and the longitudinal one by the absorber thickness.

Typical HCALs are non-compensating. Within a hadronic shower, they measure the fraction of energy deposited by EM processes with different precision relative to the energy deposited by hadronic interactions. Large fluctuations between the fraction of these components lead to poor resolution of the hadron energy measurement [22]. Consequently, one of the current fronts in hadronic calorimetry is the development of compensation methods to yield an equal response to both [23, 24].

The relative single hadron energy resolution of a hadronic calorimeter is often parametrized by

$$\frac{\sigma}{\langle E \rangle} = \frac{S}{\sqrt{E}} \oplus C \oplus \frac{N}{E} \quad (5)$$

S, C, and N are the stochastic, constant, and noise terms, respectively. The stochastic term represents poisson-like processes, such as quantum and sampling fluctuations. The former consists of the fluctuations of the invisible energy and the EM component fraction, and the latter refers to the fraction of deposited energy in the active material of the sampling elements. The constant term relates to the calorimeter module itself: shower energy leakage (for hadrons that are not fully absorbed by the calorimeter), response non-uniformities, acceptance, and other construction imperfections. The noise term incorporates electronics noise contributions and pile-up interactions that saturates the readout channels [22]. As an example, the relative single pion energy resolution of the ATLAS HCAL is  $\frac{\sigma}{E_{\pi} [GeV]} = \frac{52.9\%}{\sqrt{E_{\pi} [GeV]}} \oplus 5.7\%$  [25].

Current experiments use mostly large calorimeter cells that do not allow distinguishing the energy measurements of two nearby particles. In particular, the energy deposited by all the particles in a jet is measured as a whole. Since hadrons carry on average  $\sim 70\%$  of the jet energy [26], the jet energy resolution is strongly affected by the poor resolution of the energy measured by the HCAL [22]. In addition, the particle constituents in a jet could vary significantly between them. Since the average EM component is different for different hadrons, e.g., that of a proton is smaller than that of a pion, the jet energy resolution degrades even more. As an example, the relative jet energy resolution, in terms of transverse momentum ( $p_T$ ), measured by ATLAS corresponds to  $\sigma_{p_T}/p_T = (8.4 \pm 0.6)\%$  for 100 GeV/c jets, about 2.5 worse than the 3% targeted by future accelerator experiments.

### 2.2.1 Particle flow Calorimetry

Particle flow is a leading approach to mitigate the effect of the poor performance of the HCAL on the jet energy resolution [13, 27, 28]. It is based on the observation that most of the particles forming a jet are

charged, and their momenta can be measured precisely using the tracking system instead of the HCAL. Therefore, the jet energy resolution could be improved by measuring the energy deposited by each particle in the most accurate subsystem for its type. Table 2 (taken from [13]) lists the approximate jet energy fraction carried by charged particles, photons, and neutral hadrons; the assumed single-particle energy resolution of different subdetectors (similar to the ILD design [29]) and their contributions to the jet energy resolution. As can be seen, in the particle flow approach, only  $\sim 10\%$  (instead of  $\sim 70\%$ ) of the jet energy is measured by the HCAL.

**Table 2:** Contributions from the different particle components to the jet-energy resolution (all energies in GeV). The table lists the approximate fractions of charged particles, photons, and neutral hadrons in a jet of energy,  $E_j$ , and the assumed single particle energy resolution by [13].

| Component                     | Jet energy fraction | Detector | Energy Res.           | Jet Energy Resolution       |
|-------------------------------|---------------------|----------|-----------------------|-----------------------------|
| Charged Particles ( $X^\pm$ ) | $\sim 0.6E_j$       | Tracker  | $10^{-4}E_{X^\pm}^2$  | $< 3.6 \times 10^{-5}E_j^2$ |
| Photons ( $\gamma$ )          | $\sim 0.3E_j$       | ECAL     | $0.15\sqrt{E_\gamma}$ | $0.08\sqrt{E_j}$            |
| Neutral Hadrons ( $h^0$ )     | $\sim 0.1E_j$       | HCAL     | $0.55\sqrt{E_h}$      | $0.17\sqrt{E_j}$            |

Particle flow algorithms precisely measure the energy of charged particles in the tracking systems, ignoring their energy deposits in the calorimeter to avoid double counting. Energy deposits in the HCAL that are not associated with a charged particle (not matched to a track) are considered originating from neutral hadrons and measured with the precision of the HCAL. The confusion term refers to energy depositions that could be associated with either a charged or neutral hadron or when a single cell contains energy deposited by both a charged and a neutral hadron [13]. It becomes pronounced in the presence of two overlapping showers. In order to reduce the confusion term, particle flow calorimeters must have high granularity (longitudinal and transverse). This requirement makes sampling calorimeters a natural choice. A few particle flow algorithms were developed; the most studied ones are Pandora [13], ARBOR [27], and GARLIC [28]. In addition, in recent years, the HEP community started investing in deep learning (DL) tools development for particle flow algorithms [30, 31].

Implementing this approach in the CMS experiment resulted in a significant improvement of the jet-energy resolution (Figure 4) while proving itself to be superior to other techniques in terms of higher efficiency, lower fake-rate, and better resolution for the jet and missing transverse momentum [32]. The

ATLAS experiment also implemented particle flow algorithms, demonstrating less pronounced improvement [33].

The community studied three alternative readout approaches in the context of particle flow calorimeters: analog, digital, and semi-digital. The requirement of high granularity over large area coverage results in particle flow HCAL designs comprising tens of millions of readout channels. Since digital and semi-digital electronics is cheaper than analog ones, DHCAL systems could have higher granularity at any fixed price.

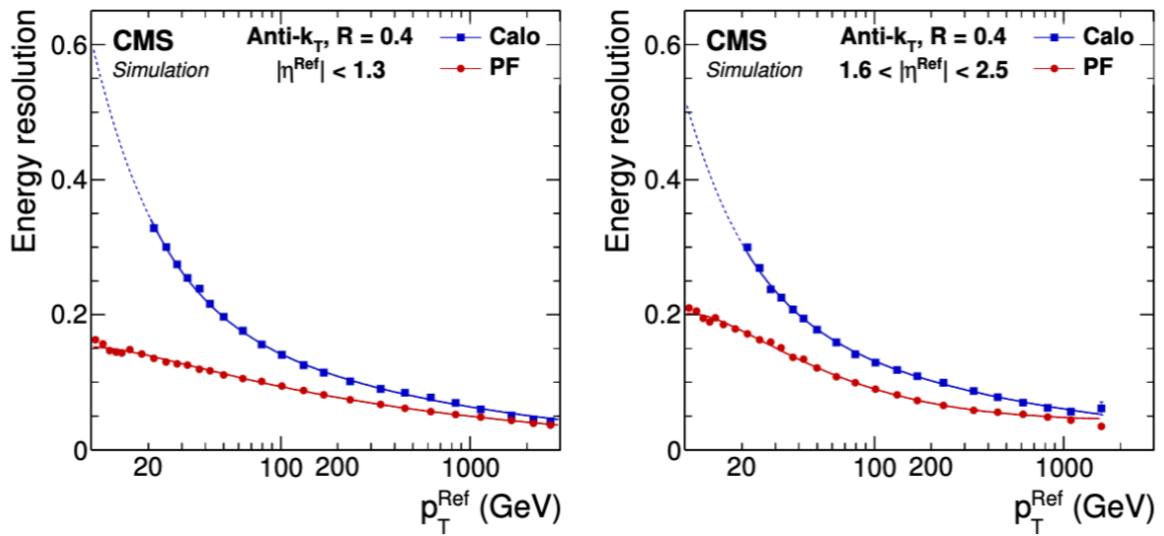


**Figure 4:** Jet energy resolution as a function of the reference transverse momentum ( $p_T^{Ref}$ ) in the barrel (left) and in the endcap (right) regions of the CMS experiment. The lines, added to guide the eye, correspond to fitted functions with ad hoc parametrizations.[32]

## Analog HCAL (AHCAL)

The CALICE AHCAL prototype is a scintillator-based sampling calorimeter with steel absorbers (Fe-AHCAL) [34]. The active layers consist of 5-mm-thick scintillator tiles read out by silicon photomultipliers (SiPMs). To reduce the number of channels (the cost of the prototype), the tiles' size is increased from the center outwards:  $3 \times 3$ ,  $6 \times 6$ , and  $12 \times 12$  cm<sup>2</sup>. The schematic and a photo of one module are shown in Figure

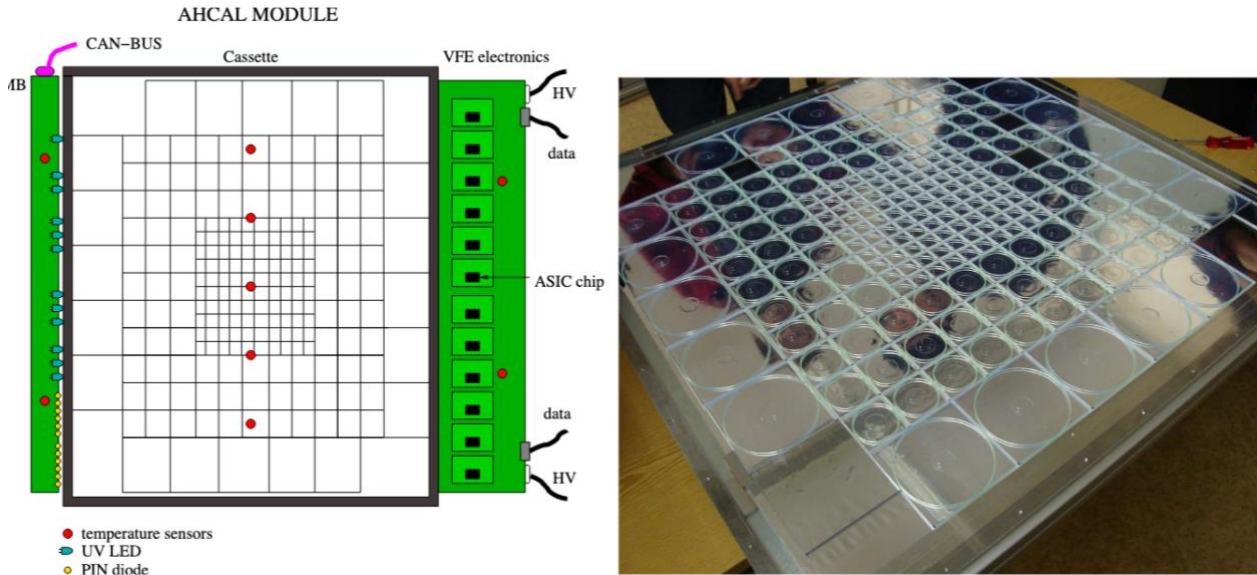


**Figure 5:** A schematic of the tile layout of a scintillator module (left) and a photograph of the module's tiles (right) [34].

5. Figure 6 shows the performance of a 38-layers Fe-AHCAL prototype measured in pion beam in comparison to GEANT4 simulations with different physics lists [35]. The relative pion energy resolution parametrization (eq. 5) fit to the Fe-AHCAL data yields

$$\frac{\sigma}{\langle E[\text{GeV}] \rangle} = \frac{(57.6 \pm 0.4)\%}{\sqrt{E[\text{GeV}]}} \oplus (1.6 \pm 0.3)\% \oplus \frac{0.18}{E[\text{GeV}]}$$

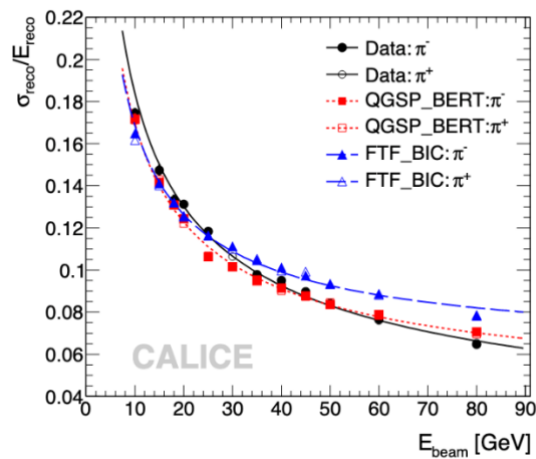


**Figure 6:** Uncorrected relative pion energy resolution versus beam energy for data and simulations using the physics lists QGSP\_BERT and FTF\_BIC [35].

## Digital HCAL (DHCAL) and Semi-Digital HCAL (SDHCAL)

These days, (S)DHCAL is considered for many future experiments, mainly in future electron-positron accelerators. The most advanced prototype was built and tested by the CALICE collaboration for the two experiments considered for the ILC: the SiD [36] and the ILD [37]. More recent is the idea of incorporating (S)DHCAL in the CEPC detector [8]. (S)DHCAL is also a possible solution for the  $e^-e^+$ -FCC; however, it is unclear whether it could also be valid in the high pileup environment foreseen in typical proton collider experiments, specifically the pp-FCC. A large number of pileup hits could degrade substantially the linear relation between the number of hits fired and the incoming particle energy.

The baseline design of CEPC and ILC DHCAL systems [1, 29] comprises 40–50 layers of absorber plates (either stainless steel or tungsten, corresponding to 20.42 cm and 11.33 cm pion interaction length, respectively) separated by 8-mm-thick active sampling elements with  $1\times 1$  cm<sup>2</sup> readout pads. High single-particle (MIP) detection efficiency and low average pad-multiplicity (number of readout pads activated per crossing particle) are essential in this application, as is a uniform response. In DHCAL, detection efficiency uniformity is sufficient, while SDHCAL requires also gain uniformity. To the best of our knowledge, no detailed study was conducted, which shows the exact relation between these parameters and the jet-energy resolution in the context of particle flow calorimetry.

Several detector technologies were suggested as candidates for sampling elements for (S)DHCAL: Resistive Plate Chamber (RPC) [38], Micro-Mesh Gaseous Structure (Micromegas, MM) [39], and Gaseous Electron Multiplier (GEM) [40]. Using  $1\times 1$  cm<sup>2</sup> square readout pads, the RPC has yielded so far an average pad-multiplicity of 1.6 at 98% efficiency [41]. MM-based sampling elements have demonstrated superior properties: 98% efficiency with a 1.1 average pad-multiplicity [42]. Resistive-MM prototypes, introduced to reduce the probability of discharges induced by highly ionizing particles, demonstrated MIP detection efficiency of 95% at similar average pad-multiplicity [43]. Elements based on double GEM showed a multiplicity of  $\sim 1.2$  at 95% efficiency [44].

Based on the single sampling element performance mentioned above, two DHCAL [45] and an SDHCAL [46] prototypes have been built by the CALICE collaboration with RPC sampling elements. In another experiment, 4 MM layers were incorporated into an RPC-based SDHCAL to evaluate their performance. The 1 m<sup>2</sup> RPC-based DHCAL prototype was built with  $1\times 1$  cm<sup>2</sup> readout pads. It was tested with two different absorbing materials: steel (Fe-DHCAL) and tungsten (W-DHCAL). Some tests were carried out without absorbing layers. The Fe-DHCAL was tested at the Fermilab test beam facility [20].

The number of hits as a function of the pion energy is shown in Figure 9 left, and the resulting pion energy resolution is shown in Figure 9 right. The W-DHCAL was tested at the CERN’s Proton-Synchrotron (PS) and Super Proton-Synchrotron (SPS) test beam facilities. Its response to different particles, the number of hits as a function of the particle energy, is shown in Figure 9 [47]. As discussed in subsection 2.1.1, a slightly different response is measured for pions and protons. The measured average response of a MM-DHCAL is shown in Figure 9 [39].

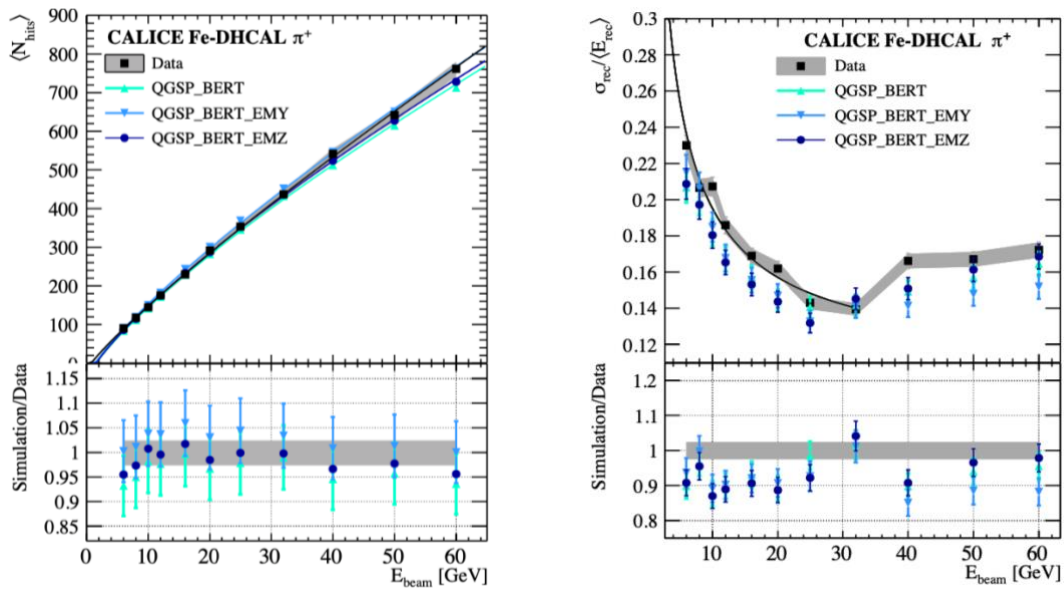


**Figure 9:** The response of the RPC Fe-DHCAL to pions (left) and the relative pion energy resolution (right) [20].

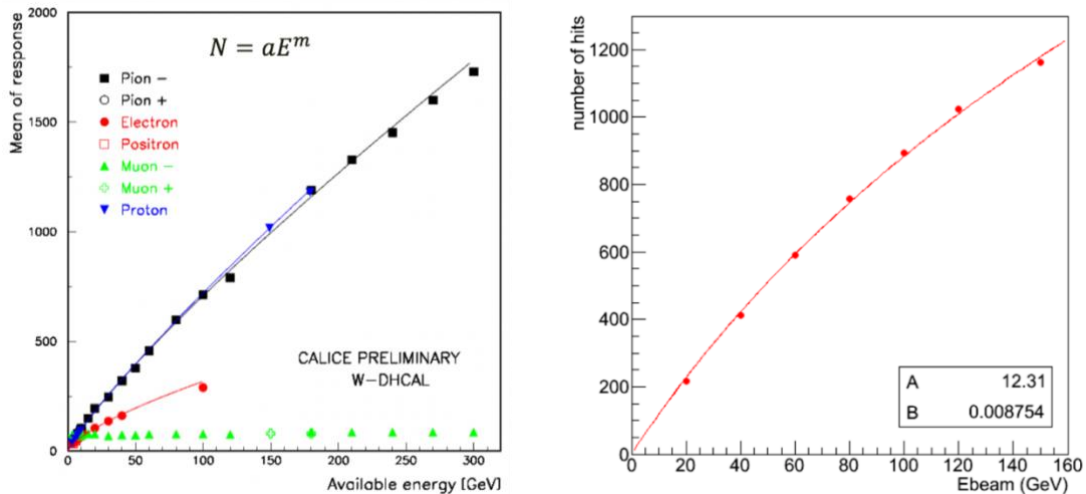


**Figure 9:** The mean response of the RPC W-DHCAL as a function of beam energy over the entire momentum/energy range of the PS and SPS beamlines [47].

**Figure 9:** Pion response deduced from a shower profile in a virtual MM SDHCAL as measured with 4 prototypes inside the CALICE steel RPC-SDHCAL [39].

## 2.3 The Resistive-Plate WELL for DHCAL

In the last decade, the WIS group investigated sampling elements based on the thick-GEM (THGEM) detector technology [17–19, 49–52]. Studies were carried out in the laboratory and in muon and pion beams. In collaboration with groups from Coimbra and Aveiro universities in Portugal and the University of Texas Arlington, single- and double-stage configurations based on the Segmented-Resistive-WELL concept demonstrated an average pad-multiplicity of  $\sim 1.1$ – $1.2$  at detection efficiency greater than 98% [48]. However, these prototypes also demonstrated a high discharge probability –  $\sim 10^{-6}$  in the presence of an intense hadron beam. The single-stage RPWELL concept was introduced [16] to achieve discharge-free operation.

### 2.3.1 The Resistive-Plate WELL

A schematic description of the RPWELL is given in Figure 10. It is a THGEM-based [49] detector consists of a single-sided Cu-clad THGEM (WELL electrode) coupled to a readout anode through a layer of material with high bulk and surface resistivity. High voltage is applied on the drift cathode ( $V_{drift}$ ) and on the WELL electrode ( $V_{RPWELL}$ ) while the readout anode is grounded via front-end readout electronics. Clusters of electrons produced by traversing particles drift along the field lines into the WELL electrode holes. There, they are multiplied through a gaseous avalanche process. Signals are induced by the motion of the charge inside the THGEM's holes. The charge evacuates through the readout anode.

The usage of the resistive plate (RP) was inspired by the RPC. A high resistivity plate ( $\rho = \sim 10^{10}$ – $10^{13}$   $\Omega\text{cm}$ ) limits the discharges to a relatively small area of  $10 \text{ mm}^2$  and small magnitude [50]. The resistive plate, together with the anode and the multiplication gap, creates an effective RC circuit with relaxation time  $\tau = \rho\epsilon$  ( $\epsilon$  is the material permittivity). Resistivity values at the order of  $10^{10}$ – $10^{12}$   $\Omega\text{cm}$  yield  $\tau$  at the order of milliseconds. This is significantly longer than the typical time scale needed to maintain a discharge, which is at the order of nanoseconds. Hence, the electrodes act, de facto, as insulators and the discharge is self-extinguished [51].

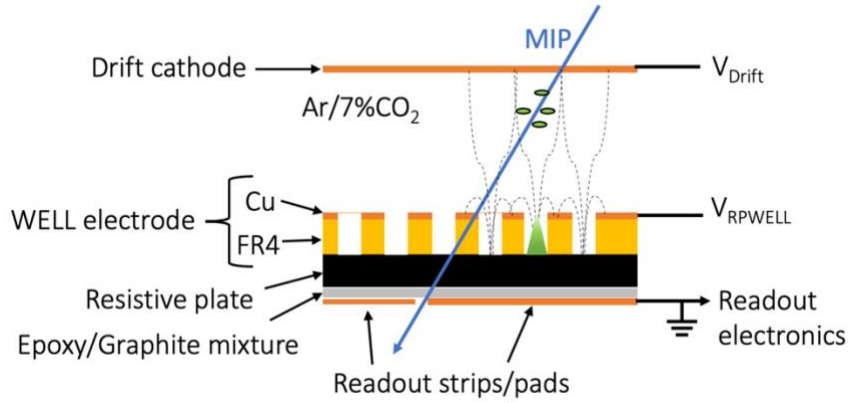


**Figure 10:** The Resistive-Plate WELL (RPWELL) configuration. The WELL electrode is coupled to a readout anode via a resistive plate. MIP induced primary electrons drift along the field lines to the RPWELL holes, where they undergo charge avalanche multiplication. Signals are induced on a segmented readout electrode by the movement of the charge. The drift and the WELL electrode are biased with  $V_{\text{Drift}}$  and  $V_{\text{RPWELL}}$ , respectively. The readout strips/pads are grounded through the front-end readout electronics.

### 2.3.2 RPWELL as a DHCAL Sampling Element

The WIS group characterized the RPWELL performance both in a generic context [16, 52–56] and in the context of the (S)DHCAL sampling element [18, 57, 58]. The latter studies were carried out at the CERN/SPS test beam facility with muon and high-rate pion beams. A medium-size ( $30 \times 30 \text{ cm}^2$ ) RPWELL-based sampling element has demonstrated more than 98% detection efficiency at less than 1.2 average pad-multiplicity in a completely discharge-free operation, also in argon-based gas mixtures [18]. Larger,  $50 \times 50 \text{ cm}^2$ , RPWELL prototypes were studied as part of this thesis.

Table 3 summarizes the performance of Sampling elements of different technologies. As can be seen, the average pad-multiplicity of the RPC prototype is significantly larger than the others. This difference can be attributed to its charge evacuation scheme. In the RPC, the charge reaching the RP is evacuated sideways and induces signals on more pads. In contrast, in the MPGD-based prototypes (RPWELL, MM, and GEM) the charge is evacuated through the readout pads. In addition, The MPGD-based prototypes are compatible to work in the same environment-friendly Argon-based gas mixture, while the RPC is not. The above performance of the RPWELL under harsh hadronic conditions places it as a suitable candidate for an (S)DHCAL sampling element.

**Table 3:** A summary of the average pad-multiplicity and MIP detection efficiency measured with sampling elements of different technologies [18, 20, 44, 59, 60].

|              | Average Pad-Multiplicity | Efficiency |
|--------------|--------------------------|------------|
| Glass RPC    | 1.6                      | 98%        |
| MM           | 1.1                      | 98%        |
| Resistive MM | ~1.1                     | 95%        |
| Double GEM   | ~1.2                     | 95%        |
| RPWELL       | 1.2                      | 98%        |

### 2.3.3 Small MPGD-based DHCAL Prototype

The performance measured with the RPWELL and MM sampling elements paved the way for constructing the first MPGD-based DHCAL prototype combining the two technologies. The decision to combine the two technologies originated from practical considerations. It allowed joining forces with groups of other expertise and testing two technologies.

Figure 11 shows the expected performance<sup>1</sup> (relative pion energy resolution) of 50×50 cm<sup>2</sup> DHCAL prototypes for different depths (number of layers). A sufficient shower containment can be achieved with a depth of ~25 layers of 2-cm-thick steel absorber plates (corresponding to ~2.5  $\lambda_\pi$ ).

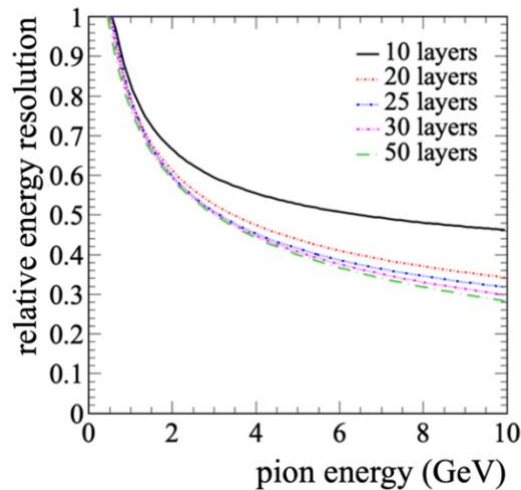


**Figure 11:** The simulated relative energy resolution as a function of pion energy for different number of calorimeter layers. Pion resolution is calculated for showers initiated in the first absorber layer.

<sup>1</sup> Based on GEANT4 simulations conducted by our colleagues at LAPP

# Chapter 3: The Development of Large Area RPWELL Sampling Elements

In this study, we aimed at constructing thin, large area ( $50 \times 50 \text{ cm}^2$ ) prototypes with maximum area coverage. The main challenge is providing a robust coupling of the WELL electrode to the RP (*RP-WELL coupling*). We present the evolution of the design and construction methods of such prototypes. All the prototypes have a similar RPWELL structure, consisting of 0.8-mm-thick WELL electrodes with mechanically drilled 0.5-mm-diameter holes in a uniform square pattern of 1 mm pitch. The electrodes are chemically etched, leaving a 0.1 mm insulating rim on the top side of the electrodes. They are coupled to a 0.7-mm-thick RP made of four  $25 \times 25 \text{ cm}^2$  tiles of silicate glass with a bulk resistivity of  $10^{10} \text{ }\Omega\text{cm}$ . The glass tiles are glued to the readout anode (segmented to strips or pads) using a thin layer of an epoxy/graphite mixture with a resistivity at the order of  $\sim 100 \text{ M}\Omega/\text{sq}$ . The drift gap is 3 mm, which allows a MIP to produce on average 30 ion-electron pairs in an Ar/7%CO<sub>2</sub> gas mixture [61]. This amount of primary electrons is sufficient for optimal MIP detection efficiency [19].

Three prototypes with 1-mm-pitch strip anode (Prototypes I-III) were tested with an analog readout data acquisition (DAQ) system comprising of the APV25 chips and the RD-51 scalable readout system (SRS) [62, 63]. The first RPWELL-based DHCAL prototype with  $1 \times 1 \text{ cm}^2$  readout pads was built with the active sensor unit (ASU) semi-digital embedded readout electronics based on the Micromegas readout chip (MICROROC) [64] (Prototype IV). Prototypes I-III mainly defer in the method of the RP-WELL coupling. In Prototype I, we used 34 spacers and a central spoke to provide mechanical coupling. This internal structure results in a total dead area of about 4%, which motivated the transition to adhesive RP-WELL coupling methods. Different adhesive coupling methods were used in Prototypes II, III, and IV.

Section 3.1 presents the design and performance study of the Prototypes I-III, followed by the design and performance study of Prototype IV in section 3.2. These results are discussed in section 3.3.

## 3.1 RPWELL prototypes with analog strips readout (Prototypes I-III)

### 3.1.1 Experimental setup

The prototypes' response was characterized in terms of gain and efficiency uniformity across the detector. We tested the prototypes at the CERN/SPS H4 beamline with 150 GeV/c muons. We placed them on a remotely controlled X-Y table along the beamline after a tracking system and irradiated the detectors in steps of 5 cm in two directions perpendicular to the beam line.

#### The slow control, tracking, and readout systems

A detailed description of the tracking and readout systems can be found in [57]. The tracking system consists of three MM chambers and three scintillators. The MM chambers were used for precise track reconstruction, and the scintillators provided a clean trigger signal in an acceptance region of  $6 \times 6 \text{ cm}^2$ . The beam's full shape was  $\sim 10 \times 20 \text{ cm}^2$ . The electrodes of all the detectors (the MMs and the RPWELL) were biased individually – via low-pass filters – by CAEN A1833P and A1821N HV power supply boards controlled, monitored, and stored with a CAEN SY2527 mainframe unit. The MMs and the RPWELL were operated in an Ar/7%CO<sub>2</sub> mixture and read out with the APV25/SRS.

#### The data acquisition and analysis framework

The signals from the tracking system and the tested prototype were read using the mmDAQ software [65]. Before each physics run, dedicated pedestal runs with a random trigger were performed. For each channel, the mmDAQ used the pedestal to extract the baseline and noise level. A common Zero-order Suppression Factor (ZSF) was used to adjust the baseline and create an online threshold for each channel. The raw data was kept in a ROOT tree [66], and we used a dedicated offline analysis software [67] to map each channel to its specific position in the relevant detector.

#### The method of charge-cluster Measurements

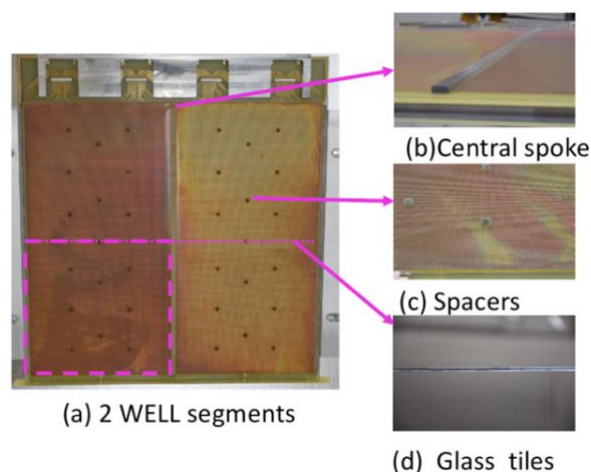
In each event, signals from the RPWELL strips were recorded if the measured charge was above a given threshold. Neighboring fired strips were grouped into a cluster. The cluster's charge was the sum of the charge measured on all the cluster's strips, and its position was defined as the charge-weighted average of

the strips' position. The muons tracks were reconstructed from the signals recorded by the MMs. They were used to determine an interception point of the muon with the RPWELL plane. Matching a cluster in the RPWELL to a muon track was confirmed if its position was close to the interception point (less than 10 mm).

### 3.1.2 Prototype I – Mechanical Coupling

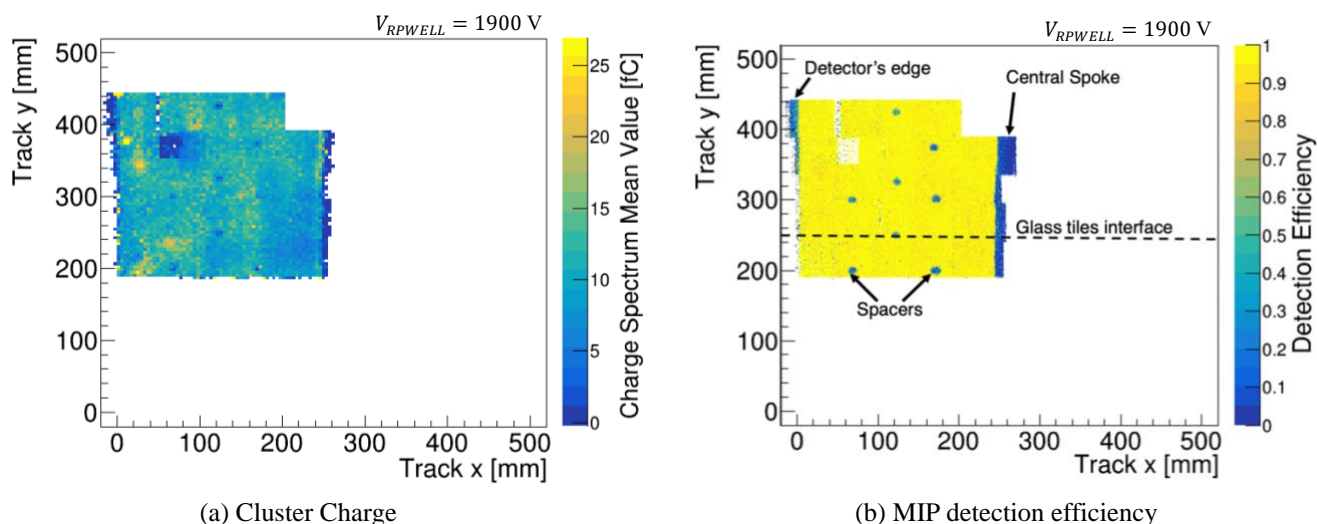
Our first large area prototype was based on the mechanical pressing concept. Relying on an idea developed for the Thin-Gap Chambers (TGC) [68] and the Compass Ring Imaging Cherenkov (RICH) detector scheme [69], support buttons and one central spoke were positioned on dedicated regions in the WELL electrode (Figure 12) and pressed from the top by the cathode. Concretely, the prototype was built from two  $25 \times 50 \text{ cm}^2$  WELL electrodes mechanically pressed to the glass using a support structure made of 34 spacers and a spoke.

Figure 12 shows the components of the detector. Figure 12-a shows the two WELL electrodes placed on the glass RP. The magenta-colored square represents a single glass tile placed underneath. Figure 12-b, c, and d show the central spoke, spacers, and interface region between two adjacent glass tiles, respectively.



**Figure 12:**  $50 \times 50 \text{ cm}^2$  RPWELL single sampling elements comprised (a) two segments of 0.8-mm-thick WELL electrodes separated by (b) a central spoke. (c) Spacers keep a 3 mm drift gap from the drift cathode. Each WELL segment was coupled to a segmented strip readout anode through (d) two adjacent 0.7-mm-thick glass of high bulk resistivity.

Figure 13 shows the 2D map of the performance along the irradiated region of Prototype I in terms of the (a) local mean cluster-charge and (b) MIP detection efficiency. The white region indicates areas that were not scanned due to range limitations of the X-Y table used in this test. The prototype demonstrated high and uniform MIP detection efficiency across the scanned active region (Figure 13-b). Large gain non-uniformity is observed in Figure 13-a. Some of them are attributed to the detector's instabilities (high charge points) and others to WELL electrode's thickness variations. Nevertheless, since the efficiency is fairly uniform, we can also conclude that the signals in the low charge regions were separated from the noise.



**Figure 13:** 2D-map of the (a) local mean cluster charge and (b) MIP detection efficiency of prototype I. The white region indicates regions which were not scanned.

In terms of the detector design, there is no visible effect around the interface of the glass tiles. The central spoke and the spacers are well observed as dead-areas in this map. The total acceptance of such a prototype is about 96%.

### 3.1.3 Prototype II – Adhesive Coupling (Spray)

We developed a special gluing technique for RP-WELL coupling, transitioning to a detector design without an internal support structure. The main risk in gluing electrodes with many small holes is glue penetrating them, resulting in residues of insulating material in the high multiplication region – a known source for electrical discharges. Therefore, a small and controlled amount of glue should be applied such that it is in contact only with the bottom of the electrode.

Prototype II was the first glued  $50 \times 50$  cm<sup>2</sup> RPWELL sampling element. It was built from two  $25 \times 50$  cm<sup>2</sup> 0.8-mm-thick WELL electrodes (with thickness variations of 5% and 10%) with holes for spacers<sup>2</sup>. A thin layer of 3M 75 spray adhesive<sup>3</sup> was sprayed on a plastic sheet. The WELL electrodes were placed on the sheet, transferring a small amount of glue to their bottom side sheet avoiding glue penetration in the holes, and then were glued to the RP tiles.

Figure 14 shows the 2D map of the local mean cluster charge of Prototype II. This coupling attempt was unsuccessful, and the electrodes were detached from the glass – indicated by the large white region in the upper part of the map caused by a deficient gas gain (signals were observed, but they were below the set threshold). In addition, we observe gain variations in a clear vertical-line pattern, which could be related to thickness variations of the electrode. Another possibility is that this vertical-line pattern, aligned with the direction of the readout strips, was caused by non-uniformities of the epoxy/graphite mixture used to couple the glass tiles to the readout strips. Such non-uniformity could change the capacitance of the readout strips and introduce non-uniform signal induction.

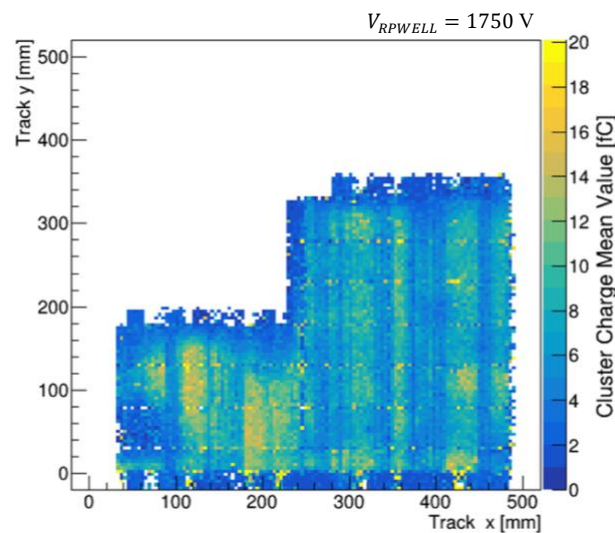


**Figure 14:** 2D map of the average cluster charge of Prototype II. The white region is a low gain region due to the detachment of the WELL electrode from the glass.

<sup>2</sup> We exercised the procedure using two available electrodes instead of one.

<sup>3</sup> [https://www.3m.com/3M/en\\_US/p/d/b40069398/](https://www.3m.com/3M/en_US/p/d/b40069398/)

### 3.1.4 Prototype III – Adhesive Coupling (Epoxy)

The poor performance of Prototype II motivated searching for a more robust adhesive material and improving the glue spreading technique. The epoxy family was an immediate candidate. We tested a few types of epoxy-based glue; we spread them on the electrode with an improved glue-transfer procedure developed in the assembly of Prototype II – this time, a dedicated glass plate was used instead of a plastic sheet. Using a microscope, we examined the gluing quality in the hole's vicinity, ensuring no glue penetrated the holes. We found that the Araldite® AY103+HY991 mixture was suitable, while Araldite® 2011 was not – its large viscosity at room temperature did not allow spreading a thin layer in a controlled way with a roller.

We constructed two  $50 \times 50 \text{ cm}^2$  RPWELL chambers (Prototype III and IV). We used the Araldite® AY103+HY991 to glue the WELL electrode to the RP and to prepare the mixture with the graphite, which assures conductive coupling of the RP to the strips readout anode. In addition, this was the first time we built the RPWELL prototypes using a single  $50 \times 50 \text{ cm}^2$  WELL electrode.

The three-year-long shutdown of the LHC and the test-beam facilities at CERN dictated an intensive experimental program and forced some compromises. In particular, the WELL electrodes used to construct these chambers had thickness variations of more than 20%, affecting the chambers' maximum operation voltage and uniformity. According to [70], standard THGEM with  $\sim 25\%$  thickness variation can have a 240% gain variation, limiting the RPWELL operation voltage range.

We measured signals from the full  $50 \times 50 \text{ cm}^2$  active area of Prototype III. Figure 15 shows the 2D map of the local mean cluster-charge along the detector plane. These results reveal two main observations: 1) some locations are prone to high charge events, and 2) the charge non-uniformity has a vertical-line pattern. The first is demonstrated in Figure 16, which depicts an example of cluster charge local distribution measured in one of these sensitive locations. In this example, about 0.15% of the recorded events are of high charge and characterized by signals above 8000 ADC. These could be attributed to low-energy discharges, as they were not correlated with an increase in the current monitoring of the HV power supply (resolution of 10 nA). They were measured in about 40% of the detector area. These high-charge events were caused by either glue residuals that penetrated the multiplication holes or the non-uniformity of the electrode.

Regarding the vertical-line pattern, this resembles the one observed in the previous prototype (Figure 14). This pattern calls for further improvement of the WELL electrode thickness uniformity and perhaps the RP coupling to the readout strips.

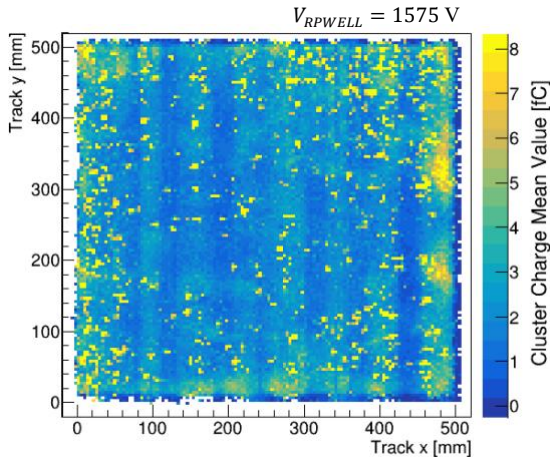


**Figure 15:** 2D map of prototype III's local mean cluster charge.

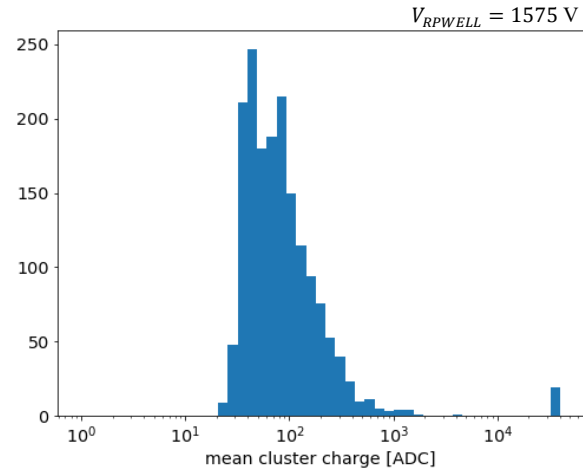


**Figure 16:** The distribution of the cluster charge for tracks in  $(x[\text{mm}], y[\text{mm}]) = (124-128, 484-488)$ .

## 3.2 RPWELL with Semi-Digital Pads Readout

Prototype IV was the first RPWELL prototype coupled to a semi-digital readout system. It was constructed following the same method as Prototype III but with an ASU-based anode. Therefore, its characterization requires a different experimental methodology.

### 3.2.1 Experimental Setup and Methodology

#### The MICROROC/ASU Semi-Digital Readout System

The 28 MICROROC semi-digital readout chips were embedded in a single ASU, reading signals induced on squared shaped  $1 \times 1 \text{ cm}^2$  pads. To reduce the cost of the prototypes, the pad-matrix had circular geometry (48 cm diameter) following the hadronic shower geometry. The data flow in the MICROROC/ASU system follows the one described in [71] and is shown schematically in Figure 17. The signals are induced on the readout pads and are processed by the MICROROC chip with a fixed shaping time of 200 ns. A *hit* is

defined as a recorded signal above one of the set thresholds. Once a channel detects a hit, its recovery time is  $1 \mu\text{s}$ . The digitized signals are stored in the chip's random-access memory (RAM) buffer. The stored data is transmitted from the RAM to a DAQ PC through the detector interface card (DIF). This transmission is triggered by the trigger system.

We operated the prototypes in a semi-digital mode, setting three thresholds at the level of 0.8, 1.4, and  $3.8 \text{ fC}$ . The first threshold is equivalent to three standard deviations above the mean noise value. We did not optimize the higher thresholds. Thus, the majority of the results are presented in digital mode, which uses only the lowest threshold.

Prototype IV was read out either in a standalone or a multi-chamber mode. In both readout modes, the system was controlled via a LabView software. In the standalone mode, the software communicated directly with the DIF, while in the multi-chamber mode, it communicated with an additional clock-cycle distribution module (DCC). The role of the DCC was to synchronize the communication and DAQ from the individual DIFs. The data transmitted by the DIF contained all the hits information stored in the buffer, meaning that hits that were not correlated, in time or space, with the trigger were also included.

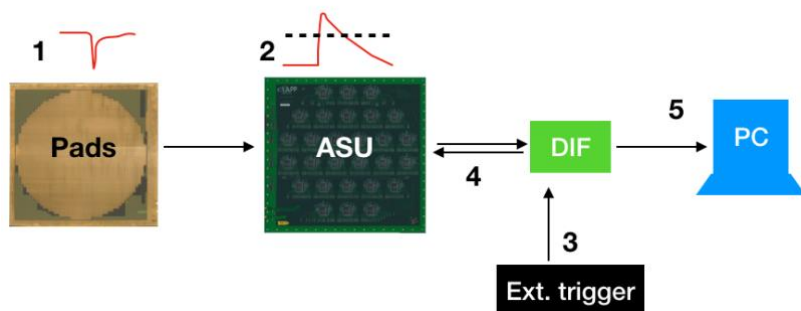


**Figure 17:** Data flow description in MICROROC-based readout system. 1) A signal is induced on the readout pads; 2) the MICROROC chip in the ASU is shaping the signal, and if it passed a threshold, it is stored in the chip's RAM; 3) An external trigger signals the detector interface card (DIF); 4) the DIF reads the RAM of the Chips, and (5) a LabView software writes the data to a file.

The analysis framework and methodology developed for analyzing the data rely on the information stored by the DAQ system for each event. These are mainly the hit position, threshold level, hit time ( $t_{hit}$ ), and trigger time ( $t_{trigger}$ ). Only trigger-correlated hits, arriving within  $\pm 600 \text{ ns}$  from the  $t_{trigger}$ , were selected for analysis.

The  $1 \mu\text{s}$  recovery time of the MICROROC was optimized for the MM technology and performance, but not for the RPWELL. Since the typical rise-time of a 0.8-mm-thick RPWELL is about  $2 \mu\text{s}$ , some signals could still be above the set threshold after the recovery time, potentially resulting in the measurement of a second hit with a  $1 \mu\text{s}$  delayed time. This effect did not impact our analysis as we

considered only trigger-correlated hits. Future prototypes will incorporate 0.4-mm-thick WELL electrodes with a typical signal rise-time of  $\sim 1 \mu\text{s}$ , thus avoiding this problem altogether.

## Experimental setup

We operated Prototype IV in two modes: standalone and multi-chamber modes. In the standalone mode, we placed the prototype on a remotely controlled X-Y table along the beamline and used three scintillators with an overlap *trigger region* of  $\sim 6 \times 6 \text{ cm}^2$  to trigger on muons. This region captures the central part of the beam, which had a total area of  $\sim 10 \times 20 \text{ cm}^2$ . In the multi-chamber mode, we positioned the RPWELL prototype after three  $48 \times 48 \text{ cm}^2$  resistive MM (provided by our collaborators from LAPP) coupled to the same type of ASU. All the chambers were placed on a remotely controlled X-Y table along the beamline and were read simultaneously from the same MICROROC-based readout system. The chambers were irradiated with 150 GeV muons at CERN/SPS H4 beamline. A drawing of the test beam setup is presented in Figure 18.

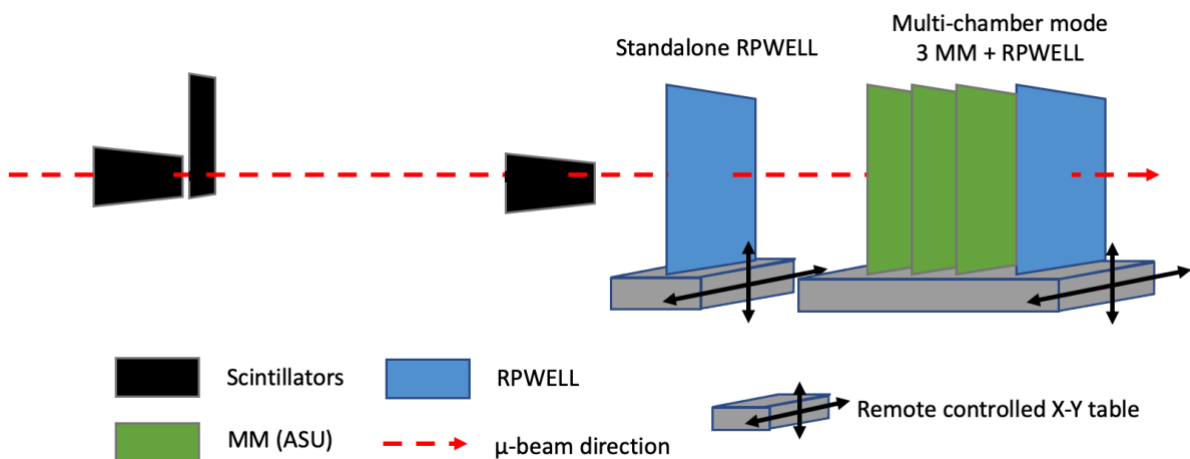


**Figure 18:** Schematics of the experimental setup. In the standalone operation mode, the RPWELL prototype is mounted on a remote-controlled X-Y table, and the scintillators trigger its readout. In the multi-chamber mode, the RPWELL prototype is positioned after three  $48 \times 48 \text{ cm}^2$  resistive MM prototypes; the same semi-digital readout system reads out the four chambers. The multi-chamber setup is placed on a remote-controlled X-Y table with a limited range of 25 cm on each axis.

## Event Cleaning

Figure 19 shows a comparison of the distribution of the number of hits per event recorded by one of the MMs detectors and the RPWELL prototype. A significant fraction of the events recorded by Prototype IV consists of more than 1000 hits. Investigations of the hits in these events have shown that they were not correlated with the trigger. They originated from spontaneous high-charge depositions in space (also observed in Prototype III, subsection 3.1.4), which resulted in the activation of all the ASU channels. Only events with less than 100 hits recorded by the RPWELL were selected in the analysis.

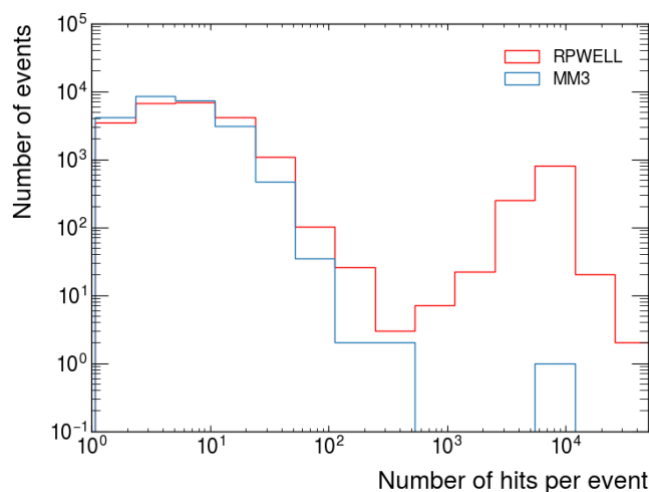


**Figure 19:** The distribution of the total number of hits per event as recorded by the ASU of the third MM chamber (blue) and the RPWELL Prototype IV (red).

## Methods for MIP Detection Efficiency and Pad-Multiplicity measurements

For the two modes of operations, the MIP detection was defined as follows:

**Standalone mode:** The *MIP detection efficiency* was defined as the ratio of the number of events with muon hits and the total number of triggered events. Muon hits are those in the trigger region. We measured the MIP detection efficiency as a function of the RPWELL operation voltage at five different locations on the active area. The maximal voltage applied in each location was defined by the onset of high current, more than 100 nA, in the HV power supply monitor. The average pad-multiplicity could not be evaluated in this mode.

**Multi-chamber mode:** The MIP detection efficiency was defined as the ratio of the number of events with a matching muon cluster and the total number of selected muon tracks. Using the Hough transform [72], Muon tracks were reconstructed from hits measured by the three MMs. Tracks were only selected if each MM had one or two adjacent hits close to the track (less than a single pad away). A group of hits sharing borders formed a cluster. A cluster’s position was defined by the averaged hit positions. It was matched to a muon track if its position was within a pad’s distance from the interception point of the track with the RPWELL. Figure 20 depicts examples of an efficient event and two inefficient ones. In the former, a muon cluster is matched with a track. While in the latter, no hits are measured by the RPWELL, or the measured cluster is not matched to the track. The pad-multiplicity per event was defined by the number of hits in the cluster of an efficient event.

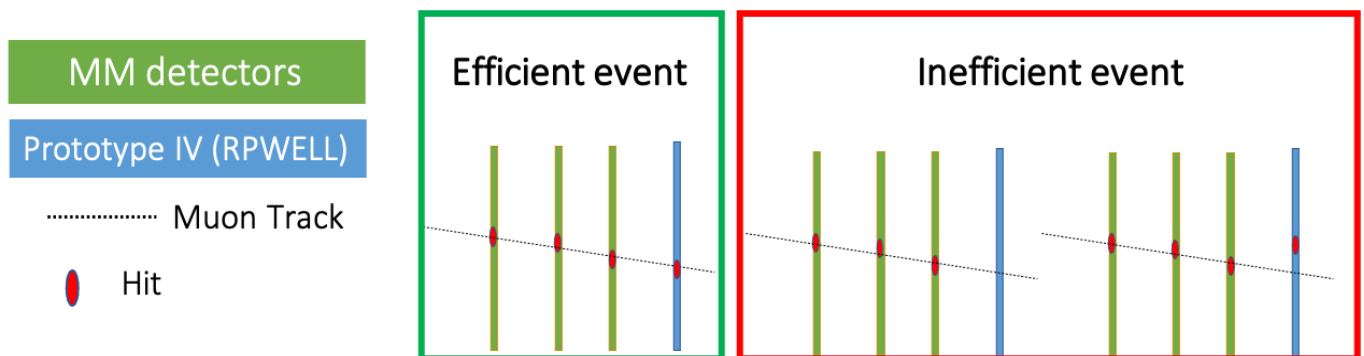


**Figure 20:** Examples of an efficient event (green box) and two ineffective ones (red box) in multi-chamber mode. Muon tracks (dotted line) are reconstructed from hits (red ovals) measured by the three MM chambers (green). An efficient event occurs when a hit cluster measured by the Prototype IV (blue) is matched to a muon track. The inefficient events consist of one with no hits are measured by the RPWELL, or the measured cluster is not matched to the track.

### 3.2.2 Results

A 2D hit beam profile measured with Prototype IV is shown in Figure 21 for the three thresholds (0.8, 1.4, and 3.8 fC) before (top) and after (bottom) selecting the trigger-correlated hits. The selection reveals the squared trigger region used to estimate the MIP detection efficiency in the standalone operation mode.

The MIP detection efficiency in different positions, measured in the standalone mode, as a function of the RPWELL operation voltage, is shown in Figure 23. The large efficiency variations (up to 50%) seen between different points are attributed to the thickness non-uniformity (gain variations, subsection 3.1.4). The efficiency plateau has not been reached at any of the measured points since instabilities occurred at a relatively low operation voltage.

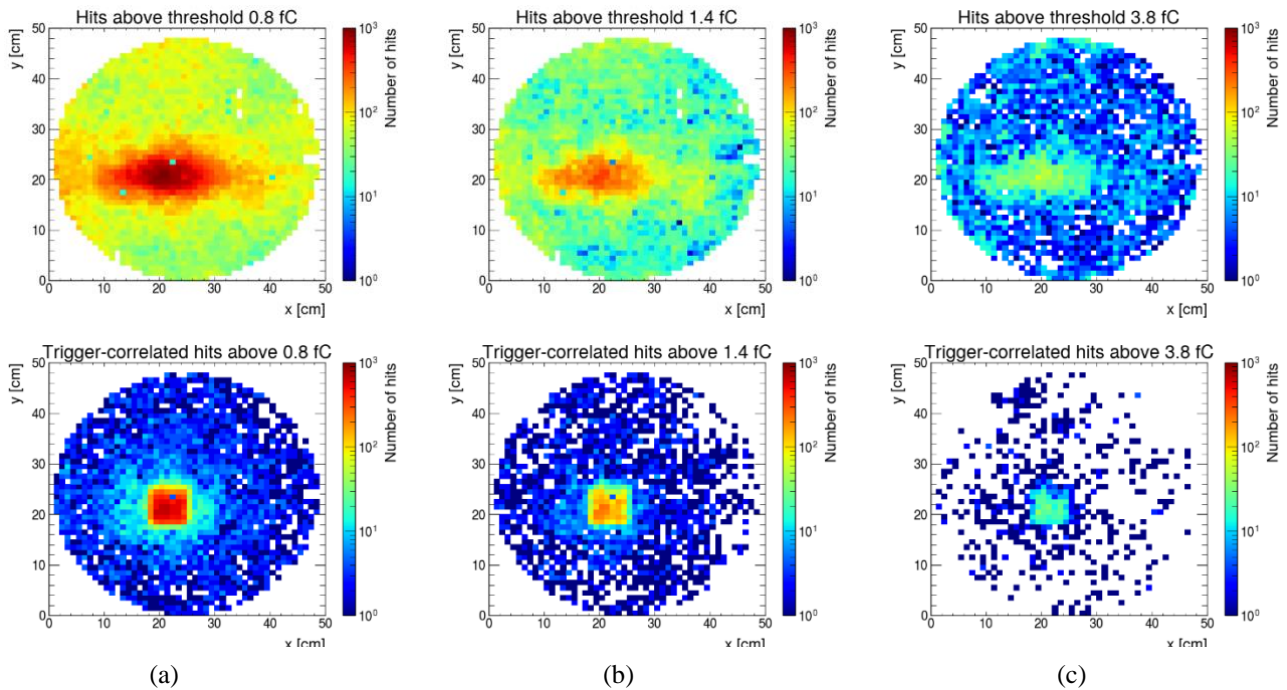


**Figure 21:** 2D hit map before (top row) and after (bottom row) selecting trigger-correlated hits. Maps are shown for the three semi-digital thresholds: (a) 0.8 fC , (b) 1.4 fC, and (c) 3.8 fC .

The MIP detection efficiency and pad-multiplicity measured in the multi-chamber mode are shown in Figure 22, in the area that could be assessed with our setup. The significant non-uniformity of Prototype IV is pronounced in the distribution of the MIP detection efficiency (top left) and its 2D map (top right). The average MIP detection efficiency of 77% (obtained with an RPWELL voltage of 1575 V) is in agreement with the results of the standalone mode. A low pad-multiplicity of  $\sim 1.1$  is shown in Figure 22's bottom plot.

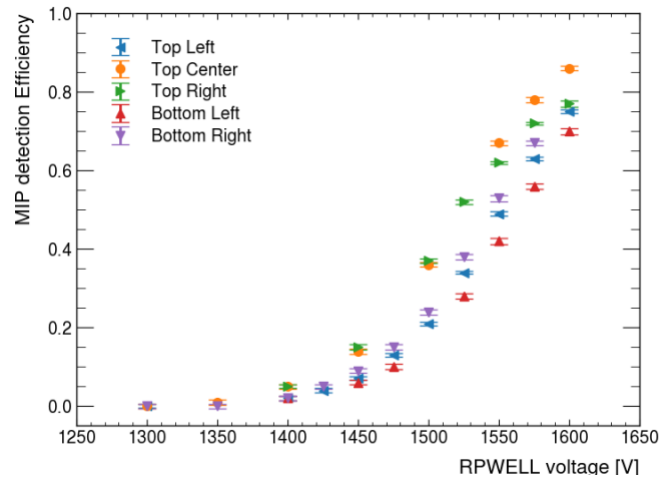


**Figure 23:** The MIP detection efficiency as a function of the RPWELL voltage at different positions on the detector; measured in standalone operation mode.

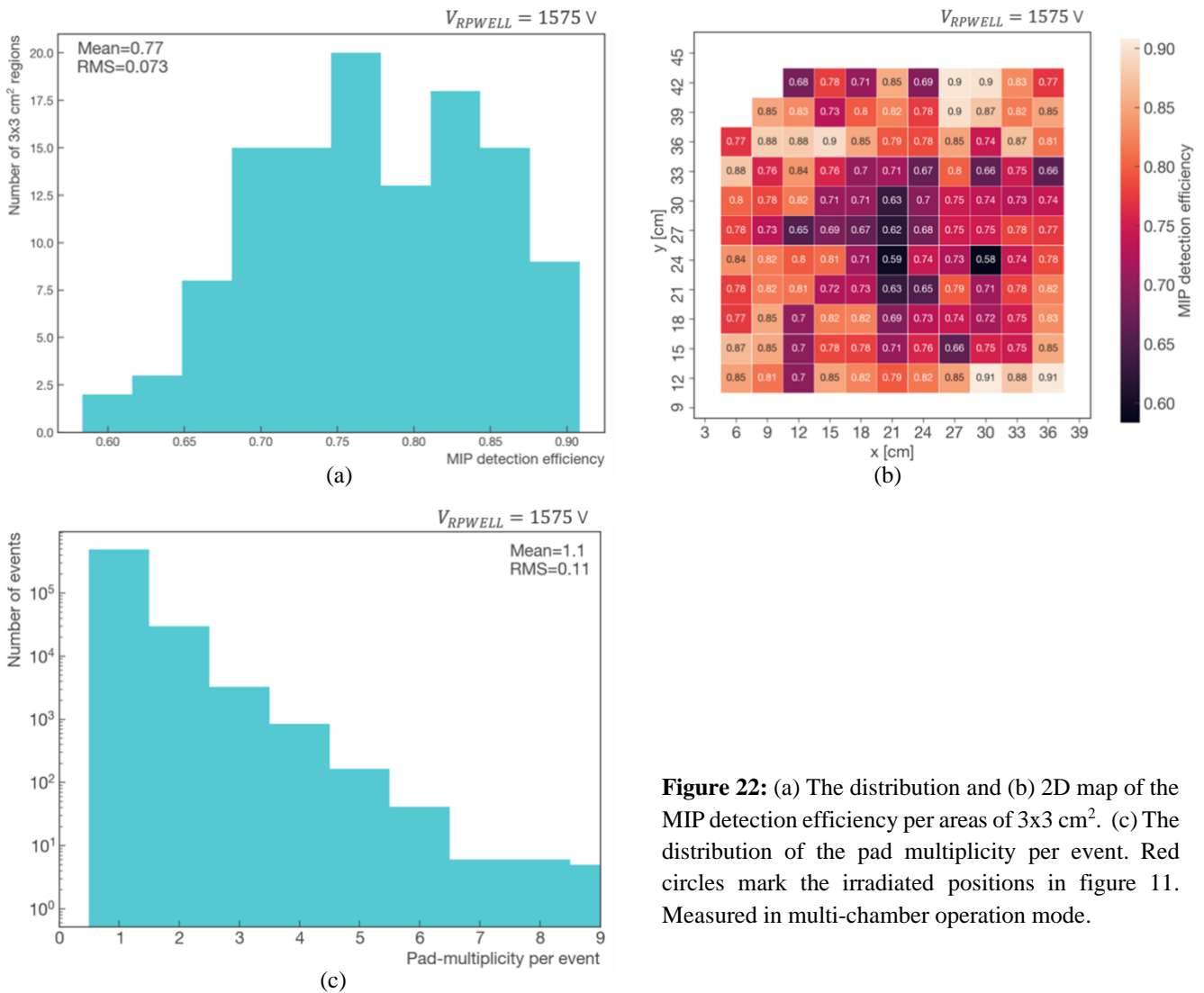


**Figure 22:** (a) The distribution and (b) 2D map of the MIP detection efficiency per areas of  $3 \times 3$  cm<sup>2</sup>. (c) The distribution of the pad multiplicity per event. Red circles mark the irradiated positions in figure 11. Measured in multi-chamber operation mode.

### 3.3 Discussion and Conclusions

This chapter presents the progress towards assembling a  $50 \times 50$  cm<sup>2</sup> RPWELL-based sampling element. In particular, it focuses on the transition from an acceptance-limited mechanical coupling, between the RP with the WELL electrode, to an acceptance-full adhesive one. While mechanically, the adhesive (epoxy) coupling was sufficiently robust, the performance was far from satisfying; instabilities, non-uniformities, and low efficiency were observed. These are attributed to two main effects. The first is the large thickness non-uniformities of the WELL electrode. New detectors (beyond the scope of this thesis) have been assembled using thinner (0.4 mm) electrodes with controlled thickness variations of up to 5%. The second is the glue penetration to the electrode's holes. A new gluing technique, limiting the gluing area to points far from the holes, is used in the assembly of the new detectors. Preliminary analysis of the test beam data collected with these new detectors shows improved performance – gain uniformity better than 10% and efficiency better than 90% at a stable operation.

## Chapter 4: A Study of a Small MPGD-based DHCAL

After the test of Prototype IV, we had only three months before the long shutdown of the LHC, which did not allow for significant modifications. Thus, we used the available non-uniform WELL electrodes and the same gluing technique to construct two additional prototypes of  $50 \times 50 \text{ cm}^2$  RPWELL sampling elements with MICROROC/ASU readout pad boards. Naturally, these prototypes had similar limitations. We combined these detectors with six MM sampling elements, provided by our colleagues from LAPP, creating the first small MPGD-based DHCAL prototype. This eight-layer prototype was tested in low-energy (2-6 GeV/c) pion beams at the CERN/PS T10 beamline. This experiment provided the first MPGD-based DHCAL data to develop an analysis methodology and validate the GEANT4-based simulation of future DHCAL prototypes. The test beam setup and the methodology of measuring the MIP detection efficiency and pad-multiplicity are detailed in section 4.1. The GEANT4 simulation and the validation methods are described in section 4.2. Experimental results and their comparison to simulation are presented in sections 4.3, followed by a discussion in section 4.4.

### 4.1 Experimental Setup and Methodology

#### 4.1.1 Experimental Setup

The small MPGD-based DHCAL prototype comprises eight alternating layers of absorber plates and sampling elements. The former consists of 2 cm thick steel plates, providing a calorimeter depth of  $\sim 16 \text{ cm}$ , corresponding to  $0.8 \lambda_\pi$  and  $\sim 8.9 X_0$ . This depth is thinner than the minimum depth required for sufficient energy containment (subsection 2.3.3) and yields a 45% (99.9%) chance of a pion (electron) shower to start within the calorimeter. The sampling elements consist of three  $16 \times 16 \text{ cm}^2$  bulk MM (two non-resistive and one resistive), three  $48 \times 48 \text{ cm}^2$  resistive MM, and two  $50 \times 50 \text{ cm}^2$  RPWELL (Figure 24). All eight sampling elements were equipped with semi-digital readout electronics based on the MICROROC/ASU [64]. The small bulk MMs comprised a squared geometry pad-matrix, while the large MM and the RPWELL were equipped with a circular geometry pad-matrix (48 cm diameter) following the hadronic shower geometry. All the readout pads were  $1 \times 1 \text{ cm}^2$  squares. The chambers were operated in a digital mode, where only the

lowest threshold of the MICROROC (set to 0.8 fC) was used. All the chambers were read out with a single DAQ system in a multi-chamber mode (see subsection 3.2.1). Three scintillators define a trigger region of  $1 \times 1 \text{ cm}^2$ , covering the center of the DHCAL X-Y plane to minimize the transverse energy leakage of the measured showers. The total beam area was  $\sim 40 \times 80 \text{ cm}^2$ .

Given the limitations discussed above, to ensure stable operation, the RPWELL chambers were operated at  $V_{RPWELL} = 1525 \text{ V}$  and  $V_{drift} = 1675 \text{ V}$ — below the efficiency plateau, where the efficiency was measured to be less than 55% (Figure 23). The MM chambers were operated at  $V_{mesh} = 480 \text{ V}$  and  $V_{drift} = 550 \text{ V}$ .

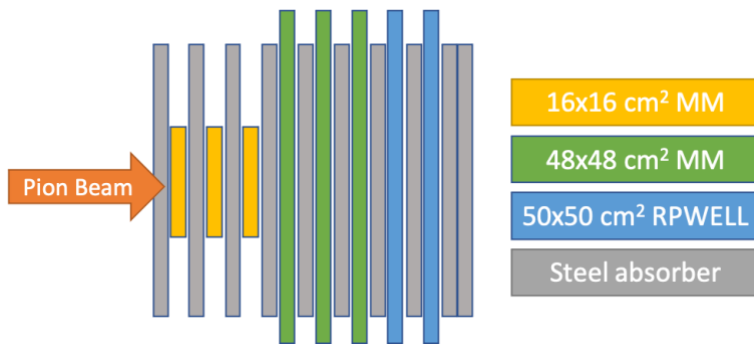


**Figure 24:** Schematic description of a small-DHCAL prototype comprising three  $16 \times 16 \text{ cm}^2$  and three  $48 \times 48 \text{ cm}^2$  resistive MM followed by two  $50 \times 50 \text{ cm}^2$  RPWELL sampling elements. 2-cm-thick steel absorber plates were inserted between neighboring sampling elements.

### 4.1.2 Data sample

We acquired a sample of  $\sim 30\text{k}$  events per beam energy. Figure 25 presents an example of the profile of a 5 GeV pion beam captured by the different sampling elements of the prototype. The limited acceptance of the first three layers is pronounced. It covers  $\sim 14\%$  of the acceptance region of the large sampling elements. Figure 26 depicts an example of a pion shower recorded by the DHCAL prototype. The shadowed (peach-colored) area in the two bottom plots indicates the region outside of the acceptance of the first three small sampling elements. This limited acceptance degraded the prototype's response since part of the shower was not sampled. This effect was mitigated by dedicated event selection criteria (discussed in subsection 4.2.4)

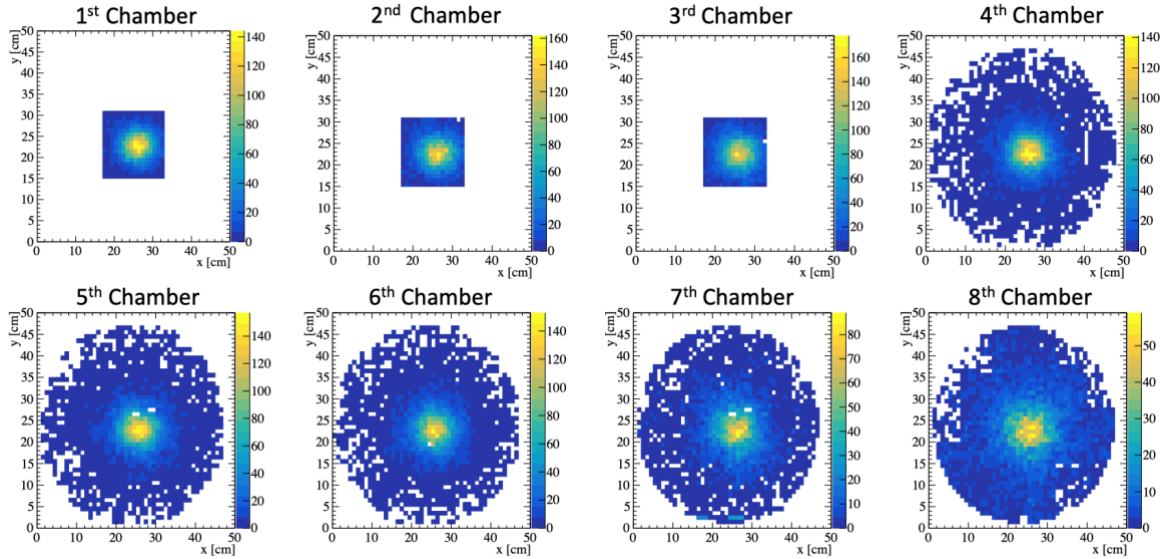


**Figure 25:** The profile of 5 GeV pion beam recorded by each sampling element of the small-DHCAL prototype (Figure 24).

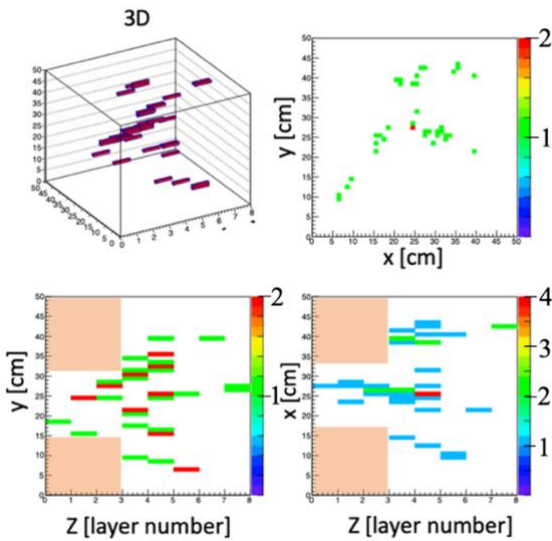


**Figure 26:** 4 GeV/c pion shower recorded with the small-DHCAL prototype (Figure 24). From top left clockwise: 3D display, X-Y projection, Z-X projection, Z-Y projection. The peach-colored surfaces mark regions outside of the chambers active area. The color map indicates the number of hits per coordinate.

### 4.1.3 Measuring Detection Efficiency and Pad-Multiplicity

Let us consider an energy deposit of a traversing particle in a sampling element. Such energy deposit is typically in the form of a cluster of electrons. The electrons are multiplied and induce signals on the readout pads. The *true pad-multiplicity* is defined as the number of pads with induced signals (including signals below a set threshold). The *hit detection efficiency* (HDE) is defined as the probability of a pad to detect a

hit, i.e., a signal above threshold. We estimated the true pad-multiplicity and the HDE from the measurements of the distribution of the pad-multiplicity and the MIP detection efficiency. The methodology presented in section 3.2 defines the measured pad-multiplicity as the number of hits (pads with signal above threshold) induced by a MIP. In other words, the measured pad-multiplicity incorporates the effect of the HDE on the true pad-multiplicity. The MIP detection efficiency is distinguished from the HDE. The former relies on detecting hits in the *vicinity* of the interception of the MIP's track and the detector, i.e., more than a single firing pad contributes to this efficiency. Appendix C: presents the calculation of the true pad-multiplicity and the HDE from a given measured distribution of pad-multiplicity and MIP detection efficiency. The true pad-multiplicity and the HDE are used in the simulation framework to emulate the response of the sampling elements.

The methodology for measuring the MIP detection efficiency and average pad-multiplicity of each sampling element in the DHCAL follows the method described for the multi-chamber operation mode in section 3.2. For each tested sampling element, the other seven sampling elements served as reference layers, providing the hit information to reconstruct the MIP tracks (energetic pions). Since pions interact more with the calorimeter material, we used stricter track selection to select quality MIP tracks, considering only those parallel to the beam axis with one hit in each reference layer.

## 4.2 Simulation Framework

We developed a GEANT4-based (version 10.06.p01 [73]) simulation to investigate the expected performance of an RPWELL-based DHCAL and optimize the sampling element design. It was validated by comparing the simulation results to the data measured in the beam. The simulation comprises three modeling stages: calorimeter modeling, physics modeling of pion interactions, and detector output.

## 4.2.1 Calorimeter Modeling

A schematic description of the DHCAL modules is given in Figure 27. It consists of alternating absorber (iron) layers, air gaps, and sampling elements. The RPWELL layers are defined by a support mask (epoxy), printable circuit board (PCB), gas (Ar/7% CO<sub>2</sub>), FR4, electrodes (Cu), and silicate glass (SiO<sub>2</sub>), while the MM layers consist of PCB, gas, and steel covers.

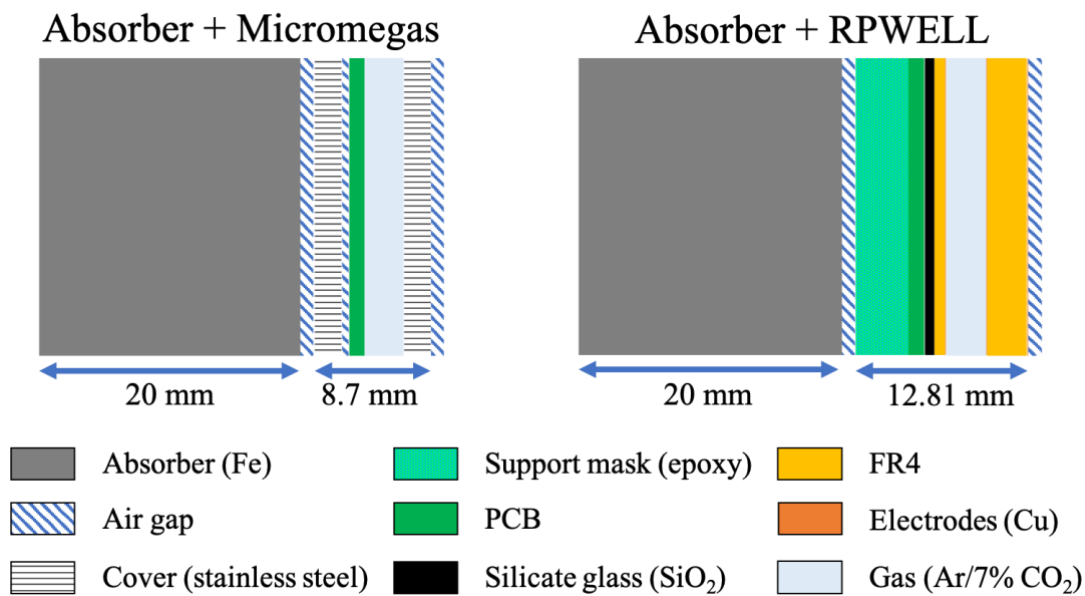


**Figure 27:** Schematics of the MM (left) and RPWELL (right) DHCAL modules as described in the GEANT4 simulation code.

## 4.2.2 Physics Modeling of Pion interactions

In the GEANT4 simulation, the physics models of the particle interactions are grouped into *physics lists*, which balance physics precision and CPU performance. Each model in a list is valid in a specific energy range and for multiple particles. In the energy ranges where two hadronic models overlap, the choice of the model is made randomly, with a probability varying linearly from 0 to 100% over the range of the overlap. Further details on the physics lists can be found in [74, 75]. We tested three physics lists to get the best agreement between the data and the simulation:

1. QGSP\_BERT: In this list, the Bertini (BERT) cascade model is used to handle nucleons, pions, and kaons with kinetic energies of up to 9.9 GeV. For 9.5 to 25 GeV, it uses the low energy parametrized (LEP) model. And the quark-gluon string pre-compound (QGSP) model for energies above 12 GeV.
2. QGSP\_BERT\_EMZ: This list is similar to the QGSP-BERT, but the parameters of the EM processes are tuned to yield better precision at the cost of using more CPU resources.
3. FTFP\_BERT\_EMZ: In this list, the Bertini cascade model is applied up to 5 GeV, while the Fritiof pre-compound (FTFP) model is used for energies higher than 4 GeV.

### 4.2.3 Digitization – from Energy Deposits to Digital Signals

The detector response, the translation of energy deposits into electronic signals, depends on its performance, particularly its detection efficiency and pad-multiplicity. It yields a set of digital electronic signals associated with specific pads for each particle. This response is not modeled by the GEANT4 simulation but with a dedicated digitization script that uses the output of the GEANT4 as an input. For each particle, the latter contains, among others, the particle ID and the information regarding its energy deposits (magnitude, position, and time).

The digitization is implemented using the following steps. First, the energy deposits outside the acceptance region are ignored, and those that are inside that region are assigned a pad position based on geometrical considerations. In the second step, hits in neighboring pads are added, reflecting the true pad-multiplicity distribution. Finally, HDE is applied to all the hits, which means that inefficient hits are deleted.

### 4.2.4 Validation Methodology

The simulation framework was validated by comparing the simulated response to a measured one. In accordance with the DHCAL prototype (subsection 4.1.1), we built an eight-layers DHCAL prototype (Figure 24) and simulated its response to low-energy pions (2, 3, 4, 5, and 6 GeV). For each beam energy, we simulated 50k single pion events. The validation of the simulation consists of two steps. In the first, which can be thought of as a closure test, we verified that the performance of each simulated sampling element (MIP detection efficiency and average pad-multiplicity) is consistent with the experimentally measured values. The second step compares the calorimeter's response – i.e., the distribution of the total

number of hits per event for a given pion energy. Two types of event selections were applied to minimize uncertainties originating from the limited acceptance of our DHCAL prototype:

- (a) **MIP-like selection:** events with a single hit in the first and last sampling element and not more than 3 hits per sampling element (Figure 28-a).
- (b) **Generic selection:** events with exactly one hit in each of the three small sampling elements and no hits outside the expected shower-cone region (marked in yellow in Figure 28-b).

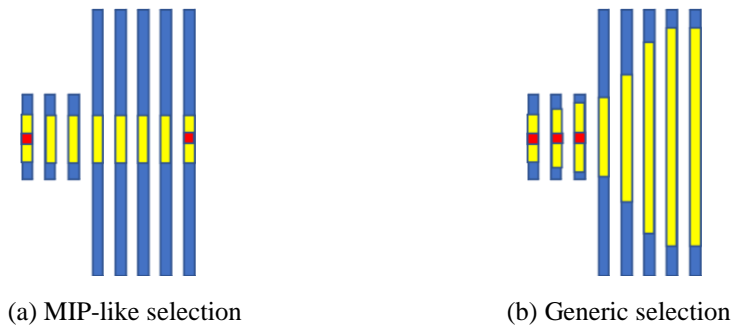


**Figure 28:** (a) A schematic description of a MIP-like selection – events with a single hit in the first and last sampling elements and not more than 3 hits per sampling element. (b) A schematic description of a generic selection – events with exactly one hit in each of the three small sampling elements and no hits outside the expected shower-cone region. The red squares represent the single-hit requirements, the yellow rectangles represent the acceptance regions.

## 4.3 Results

### 4.3.1 Examples of Recorded Events

Given the CERN/PS T10 beam profile, recorded events can contain a single hadronic pion shower, a MIP (if the pion did not shower), an EM shower (initiated by an electron), or any combination of these objects. Figure 29 shows examples of pion events: (a) a single hadronic shower event, (b) an event with two MIP-like tracks, and (c) an event of a shower starting before the calorimeter. In these examples, the 3D image (top left) is accompanied by its 2D projections on X-Y (top right), Z-Y (bottom left), and Z-X (bottom right) planes. The color-coding of the projections indicates the number of hits per coordinate.

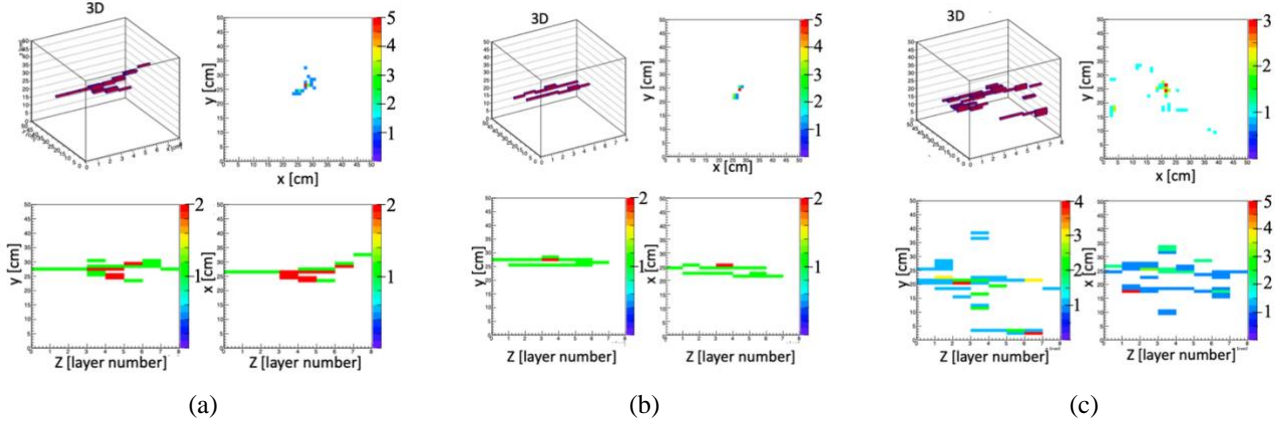


**Figure 29:** Examples of pion events: (a) a single hadronic shower, (b) two MIP-like tracks, and (c) a shower starting before the calorimeter. In these examples the 3D image (top left) is accompanied by its 2D projections on X-Y (top right), Z-Y (bottom left), and Z-X (bottom right) planes. The color-coding of the projections indicates the number of hits per coordinate. The events were recorded with the small-DHCAL prototype (Figure 24) in 4 GeV pion beam.

### 4.3.2 Experimental Data vs. Simulation

Figure 30 depicts the measured MIP-detection efficiency (left) and the average pad-multiplicity (right) per sampling element using the same estimation method (subsection 4.1.3) on the test beam data and the simulation. As can be seen, the efficiency and the average pad multiplicity measured in the simulation are in good agreement (within statistical fluctuations) with the experimental measurements. These results conclude the closure test. It confirms that the performance of each simulated sampling element is consistent with the experimental values used to determine its performance in the simulation.

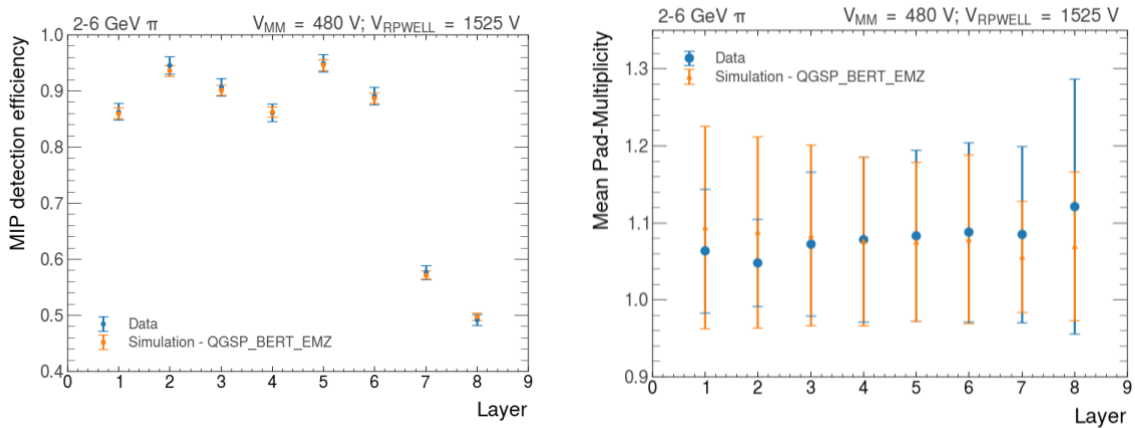
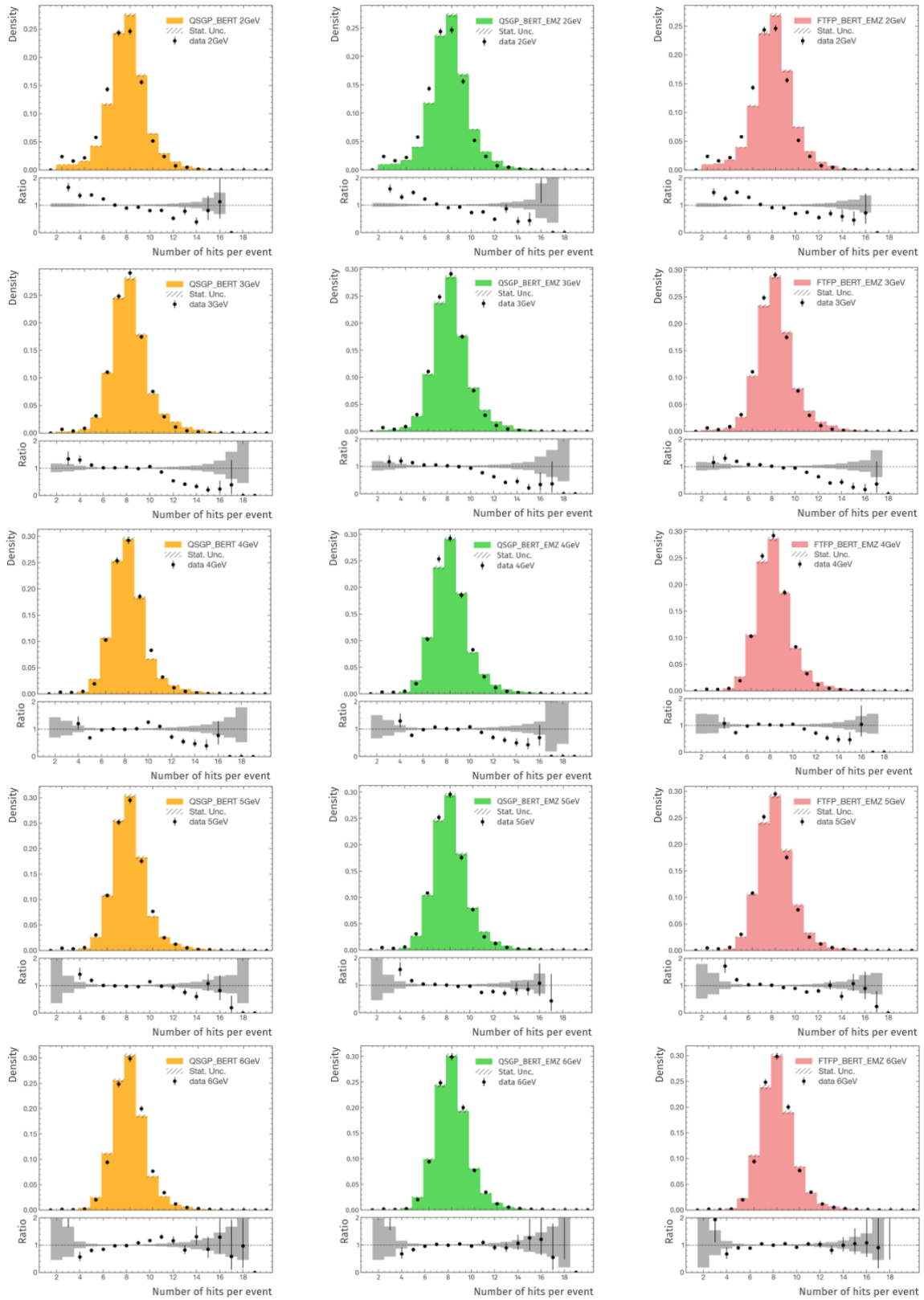


**Figure 30:** Comparison of the MIP detection efficiency (left) and average pad-multiplicity (right) of each layer as estimated from the data (blue dots), and simulation using QGSP\_BERT\_EMZ (orange triangles).

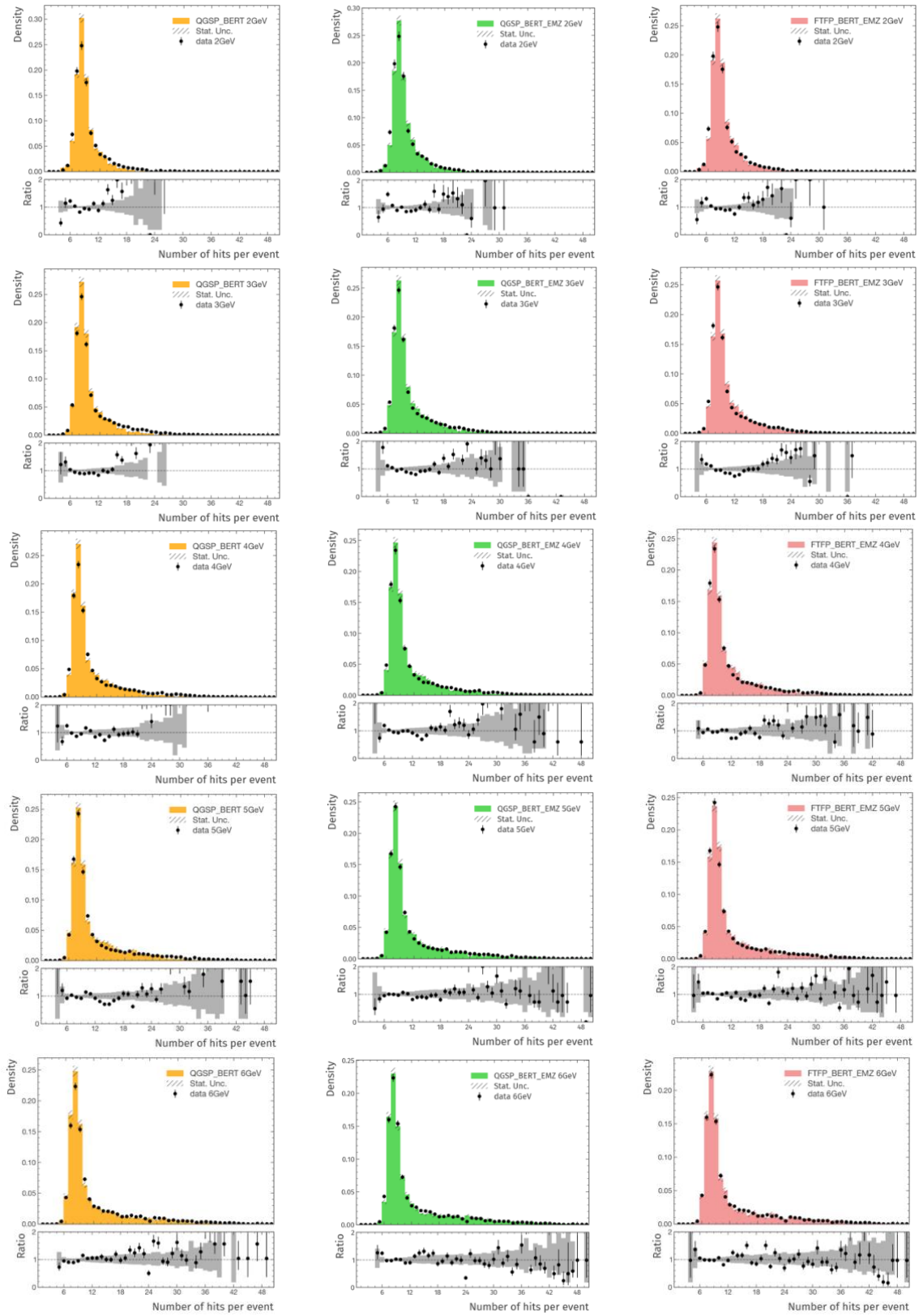
---

Figure 31 shows the distribution of the number of hits per MIP-like event (Figure 28-a) at different pion energies. The black points correspond to the measured data, and the colored regions correspond to the simulation results using the QGSP\_BERT (orange), QGSP\_BERT\_EMZ (green), and FTFP\_BERT\_EMZ (red) physics lists. Figure 32 shows the distributions for the generic event selection (Figure 28-b).

In both event selections, the agreement between the data and the simulation was improved as the beam energy increased. The agreement at the lower energies did not improve when electron impurities were simulated. At the larger number of hits, a better agreement between the data and the simulation is obtained with the physics lists containing the EMZ modeling. For MIP-like events, the distribution peak is expected at eight hits per event – single hit per sampling element. This peak is validated in both event selections at all the tested pion energies and the three physics lists.



**Figure 31:** The distribution of the number of hits per event in the test-beam data (black dots) and the simulation using QGSP\_BERT (orange), QGSP\_BERT\_EMZ (green), and FTFP\_BERT\_EMZ (red) for different energy values of the pion-beam. The events are selected by applying the MIP-like event selection (Figure 28-a). The bottom plots show the ratio of the data with respect to the simulation results.



**Figure 32:** The distribution of the number of hits per event in the test-beam data (black dots) and the simulation using QGSP\_BERT (orange), QGSP\_BERT\_EMZ (green), and FTFP\_BERT\_EMZ (red) for different energy values of the pion-beam. The events are selected by applying the generic event selection (Figure 28-b). The bottom plots show the ratio of the data with respect to the simulation results.

## 4.4 Discussion and Conclusions

We operated an eight-layers MPGD-based DHCAL in a low-energy (2–6 GeV) pion beam at the CERN/PS T10 beamline. The DHCAL imaging capability was demonstrated. We measured the MIP detection efficiency and average pad-multiplicity of each sampling element. The low MIP detection efficiency measured with the RPWELL sampling elements (below 60% when operating at 1525 V) is consistent with the one measured with Prototype IV and much lower than the 85%–95% measured with the MM sampling elements. The average pad-multiplicity measured with the two technologies is  $\sim 1.1$ , consistent with previous RPWELL and MM prototypes.

We devised a GEANT4-based framework to simulate the response of the DHCAL test beam setup assuming a uniform response of each sampling element. The particle interactions with the calorimeter material were modeled using three physics lists. The energy deposits were digitized into electronic signals based on the true pad-multiplicity and the HDE – estimated from the distribution of the pad-multiplicity and the MIP detection efficiency measured in the test beam.

We compared the results of the simulation to those of the data. The closure test confirms similar average pad-multiplicity and MIP detection efficiency. Looking at the total number of hits per event, a better agreement was found between the data and the simulation for higher energies and for the two types of event selections. The best agreement was obtained with the physics lists that include the EMZ model, as reported by the CALICE collaboration [20]. With this level of agreement, we used the simulation framework to study the expected performance of a complete RPWELL-based Fe-DHCAL module consisting of 50 layers and corresponds to a total depth of  $5\lambda_\pi$  – presented in Chapter 5.

# Chapter 5: A Simulation Study of a 50-layers RPWELL-based DHCAL module

Using the simulation framework presented in Chapter 4, we modeled a fully-equipped (50 layers) RPWELL-based DHCAL with 2-cm-thick steel absorbers, using the QGSP-BERT-EMZ physics list. These 50 layers correspond to a total depth of  $\sim 5\lambda_\pi$ , inferring a 99.3% chance for a pion to initiate a shower within the module, thus ensuring minimal energy leakage. This depth is consistent with the baseline design HCALs proposed for future collider experiments [1, 29]. We simulated the response of the module to single pions at an energy range of 2–36 GeV, similar to the one tested with the RPC Fe-DHCAL prototype [20]. 50k single pion events were simulated for each energy. The expected performance of the DHCAL was evaluated for different MIP detection efficiencies and pad-multiplicity distributions to study their effect on the pion energy resolution. MIP detection efficiency in the range of 70–98% was considered; based on the efficiency measured with smaller RPWELL prototypes, the high value represents a realistic target. Two pad-multiplicity distributions with average values of 1.1 and 1.6 were tested. The former was measured with a smaller RPWELL sampling element prototype using analog readout at a 150 GeV muon beam [19]. The latter was inspired by the value quoted for the RPC sampling elements [20].

The methodology used for the pion energy reconstruction and the estimation of the pion energy resolution is discussed in section 5.1. The results are detailed in section 5.2, followed by a discussion in section 5.3.

## 5.1 Methodology

### 5.1.1 Event selection

The event selection aims to reduce the energy leakage by considering only pion showers that start in the first ten layers of the calorimeter. This selection relies on identifying the *interaction layer* – i.e., the first layer in a hadronic shower. Supported by the study of the average longitudinal profile of pion showers that shows an increase in the number of hits per layer across the first three layers of the shower [20], the

interaction layer was identified following the methodology presented in [76]. We define each three consecutive layers as a triplet. The average number of hits in the  $i^{\text{th}}$  triplet is expressed as  $N_{trip}^i = (N_{hits}^i + N_{hits}^{i+1} + N_{hits}^{i+2})/3$ , where  $N_{hits}^i$  is the number of hits in the  $i^{\text{th}}$  layer. The  $i^{\text{th}}$  layer is defined as the interaction layer, if it has more than two hits and is the first layer that fulfills:

$$\frac{N_{trip}^i}{N_{trip}^{i-1}} > 1.1, \frac{N_{trip}^{i+1}}{N_{trip}^i} > 1.1, \frac{N_{trip}^{i+2}}{N_{trip}^{i+1}} > 1.1$$

Ten layers of the calorimeter are equivalent to about one  $\lambda_\pi$ . In agreement with the expectation, for pion energies of 6–36 GeV, this selection results in  $\sim 64\%$  efficiency. Pion events of lower energies resulted in lower efficiencies and were excluded from the analysis.

### 5.1.2 Energy Reconstruction and Energy Resolution

We define the *calorimeter response* as the relation between the average number of hits per event and the beam energy. Given the observed non-linear response (saturation), a few parametrizations have been proposed. These were not derived from fundamental principles. Two power-law parametrizations were considered in the studies of the RPC-based DHCAL prototypes [20, 77]:

$$\langle N_{hits} \rangle = a \cdot E_{beam}^b \quad ; \quad b < 1 \quad (6)$$

$$\langle N_{hits} \rangle = a \cdot E_{beam}^b - c \quad ; \quad b < 1 \quad (7)$$

Here,  $\langle N_{hits} \rangle$  is the mean value of the Gaussian fit to the distribution of  $N_{hits}$ ,  $E_{beam}$  is the pion beam energy, and a, b, and c are free parameters. A positive offset term (c) sets an energy threshold below which a pion does not yield hits in the calorimeter. The most recent works adapt the parametrization in equation (6, in which, on average, hits will be measured in the HCAL for any pion with non-zero energy.

In the context of the MM-based DHCAL studies, a logarithmic parametrization has been used [39]:

$$\langle N_{hits} \rangle = \frac{a}{b} \log(1 + bE_{beam}) \quad (8)$$

Reversing the equations above allows expressing the reconstructed energy ( $E_{rec}$ ) as a function of the measured number of hits in an event ( $N_{hits}$ ):

$$E_{rec} = \sqrt{\frac{b N_{hits}}{a}} \quad (9)$$

$$E_{rec} = \sqrt[b]{\frac{N_{hits} + c}{a}} \quad (10)$$

$$E_{rec} = \frac{1}{b} \left[ \exp\left(\frac{b}{a} N_{hits}\right) - 1 \right] \quad (11)$$

Using these equations, the energy of each impinging particle is reconstructed from its total number of deposited hits in the calorimeter. For each beam energy, the average reconstructed energy ( $\langle E_{rec} \rangle$ ) its associated error ( $\varepsilon_{\langle E_{rec} \rangle}$ ), as well as the width of the distribution ( $\sigma_{rec}$ ) are extracted with a Gaussian fit to the reconstructed energy distribution.

The *energy reconstruction bias* is defined by the relative difference between  $\langle E_{rec} \rangle$  from  $E_{beam}$  :

$$bias = \frac{\langle E_{rec} \rangle - E_{beam}}{E_{beam}}$$

The relative energy resolution is defined as the ratio between the width of the reconstructed energy distribution over its mean. Its parametrization as a function of the beam energy is based on equation (5):

$$\frac{\sigma_{rec}}{\langle E_{rec} \rangle} = \frac{S}{\sqrt{E_{beam}}} \oplus C$$

Following [20], the noise term is neglected as the DHCAL threshold is typically set well above the noise level, and the simulation does not include noise.

For simplicity, we refer to the response parametrizations (eqs. 6–8) and their corresponding energy reconstruction methods (eqs. 9–11) as the *power-law*, *power-law with an offset*, and *logarithmic* parametrizations.

### 5.1.3 Uncertainty Estimation

**The average number of hits:** As mentioned above, for each beam energy,  $\langle N_{hits} \rangle$  is extracted with a Gaussian fit to the number of hits distribution. Thus, its error is given by:

$$\sigma_{\langle N_{hits} \rangle, E} = \frac{\sigma_E}{\sqrt{N_E}} \quad (12)$$

where  $\sigma_E$  is the standard deviation of the Gaussian corresponding to a pion beam at energy  $E$ , and  $N_E$  is the number of simulated pions at that specific energy. This is the only error considered when fitting the response functions (eqs. 6–8).

**The response function:** The uncertainties associated with parameters a, b, and c of the fitted response functions are used to model *up* and *down* variations of the response functions.

**The relative energy resolution** has two contributions. The first ( $\varepsilon_v, v \in \{up, down\}$ ) relates to the uncertainty on the response function and is estimated exploiting its up and down variations. The second ( $\varepsilon_{res}$ ) relates to the uncertainty on the mean value of the nominal reconstructed energy distribution ( $\varepsilon_{\langle E_{rec} \rangle}$  is defined in section 5.1.2).

$\varepsilon_v$  is given by:

$$\varepsilon_v = \frac{\sigma_{rec}}{\langle E_{rec} \rangle} - \frac{\sigma_{rec,v}}{\langle E_{rec} \rangle_v} \quad (13)$$

$\frac{\sigma_{rec}}{\langle E_{rec} \rangle}$  and  $\frac{\sigma_{rec,v}}{\langle E_{rec} \rangle_v}$  are the relative energy resolutions calculated with the nominal response function and its up or down variations, respectively.

$\varepsilon_{res}$  is obtain from  $\varepsilon_{\langle E_{rec} \rangle}$  as a standard error propagation and is given by:

$$\varepsilon_{res} = \frac{\sigma_{rec}}{\langle E_{rec} \rangle^2} \varepsilon_{\langle E_{rec} \rangle} \quad (14)$$

Finally, the total up and down uncertainties associated with the nominal relative energy resolution is given by a quadratic sum of  $\varepsilon_v$  and  $\varepsilon_{res}$ :

$$\varepsilon_{res}^v = \varepsilon_v \oplus \varepsilon_{res} ; v \in \{up, down\} \quad (15)$$

## 5.2 Results

### 5.2.1 An Optimal RPWELL-based DHCAL

Based on [19], we can target an optimal RPWELL-based DHCAL consisting of sampling elements with 98% MIP detection efficiency and 1.1 average pad-multiplicity. Figure 33 shows the  $N_{hits}$  distributions for different pion beam energies and the curves of their Gaussian fits.

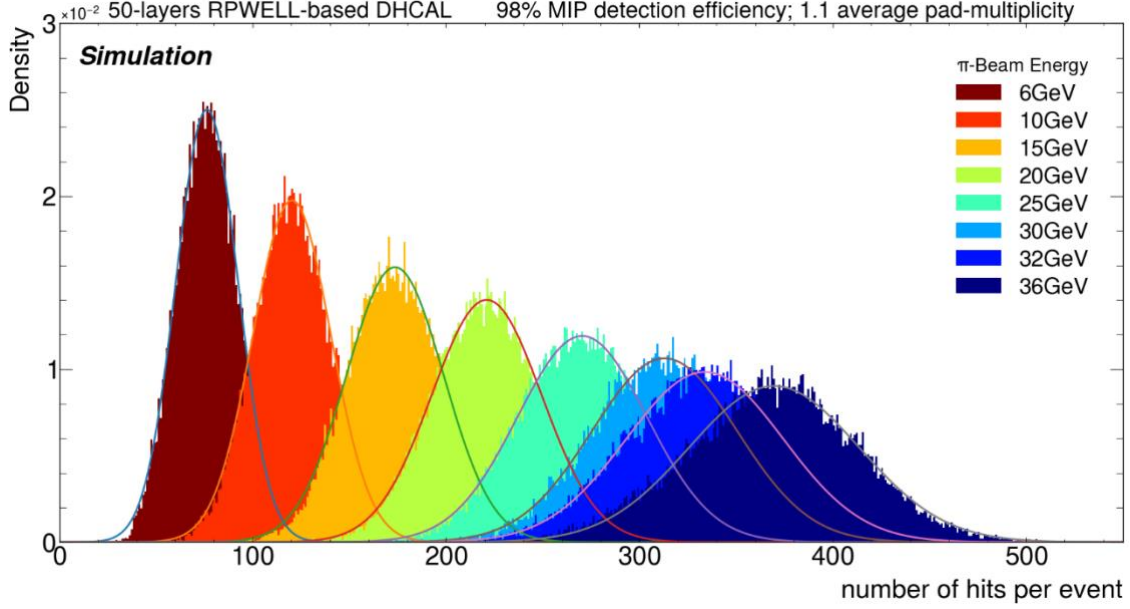


**Figure 33:** The distributions of the number of hits per event for different simulated pion-beam energy and the corresponding Gaussian fits.

The calorimeter response is shown in Figure 34 with its three parametrizations; the fit parameters are summarized in Table 4. The energy reconstruction bias and relative energy resolution as a function of the pion beam energy are shown for the three parametrizations in Figure 35 and Figure 36, respectively. The power-law parametrizations yield similar bias values (smaller than 2% with an average of 0.7%), better than those of the logarithmic one (with a maximum bias of 3.5% and an average of 1.2%). The relative energy resolution was obtained with the power-law parametrization,  $\frac{\sigma}{E[\text{GeV}]} = \frac{(50.8 \pm 0.3)\%}{\sqrt{E[\text{GeV}]}} \oplus (10.3 \pm 0.06)\%$ . It is similar to the one of the power-law with an offset,  $\frac{\sigma}{E[\text{GeV}]} = \frac{(47.6 \pm 3.7)\%}{\sqrt{E[\text{GeV}]}} \oplus (11.1 \pm 0.03)\%$ , and superior to that obtained with the logarithmic parametrization,  $\frac{\sigma}{E[\text{GeV}]} = \frac{(42 \pm 0.5)\%}{\sqrt{E[\text{GeV}]}} \oplus (12.5 \pm 0.4)\%$ , at pion energies higher than 15 GeV.

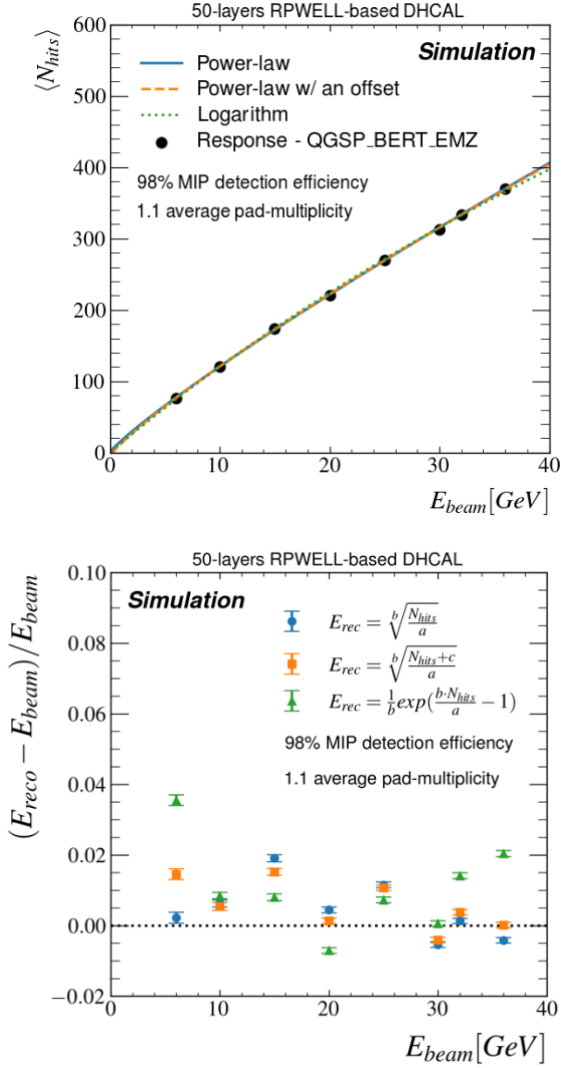


**Figure 35:** The energy reconstruction bias as a function of the beam energy obtained with the power-law (blue dots), power-law with an offset (orange squares), and logarithmic (green triangles) parametrizations.

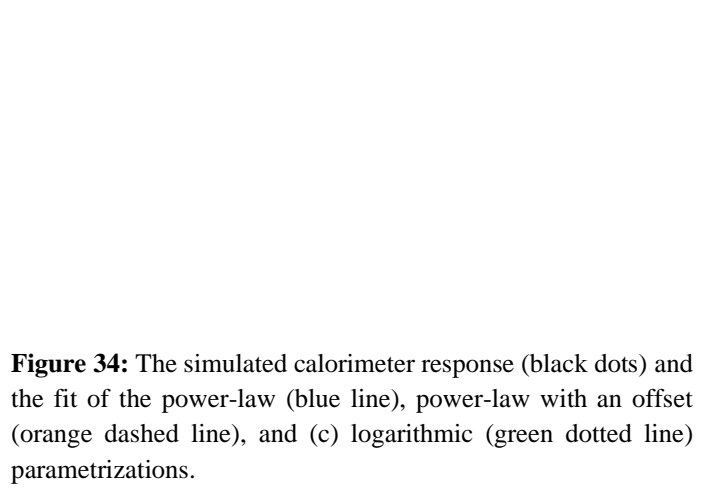


**Figure 34:** The simulated calorimeter response (black dots) and the fit of the power-law (blue line), power-law with an offset (orange dashed line), and (c) logarithmic (green dotted line) parametrizations.

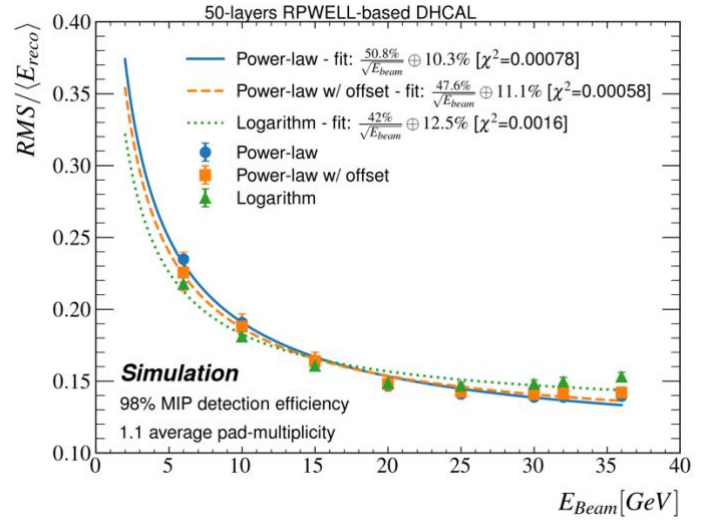


**Figure 36:** The relative energy resolution as a function of the beam energy obtained with the power-law (blue dots), power-law and an offset (orange squares, dashed line), and logarithmic (green triangles) parametrizations. Their corresponding fits are marked with a full line, dashed line, and dotted line, respectively.

## 5.2.2 The Effect of MIP Detection Efficiency

We evaluated the effect of the MIP detection efficiency on the DHCAL performance at a fixed pad-multiplicity distribution with an average of 1.1. The calorimeter response for different MIP detection efficiency values is shown in Figure 37 for (a) the power-law, (b) the power-law with an offset, and (c) the

logarithmic parametrizations. The fit parameters are summarized in Table 4. Fits of good qualities were obtained as indicated by their corresponding  $\chi^2$  values.

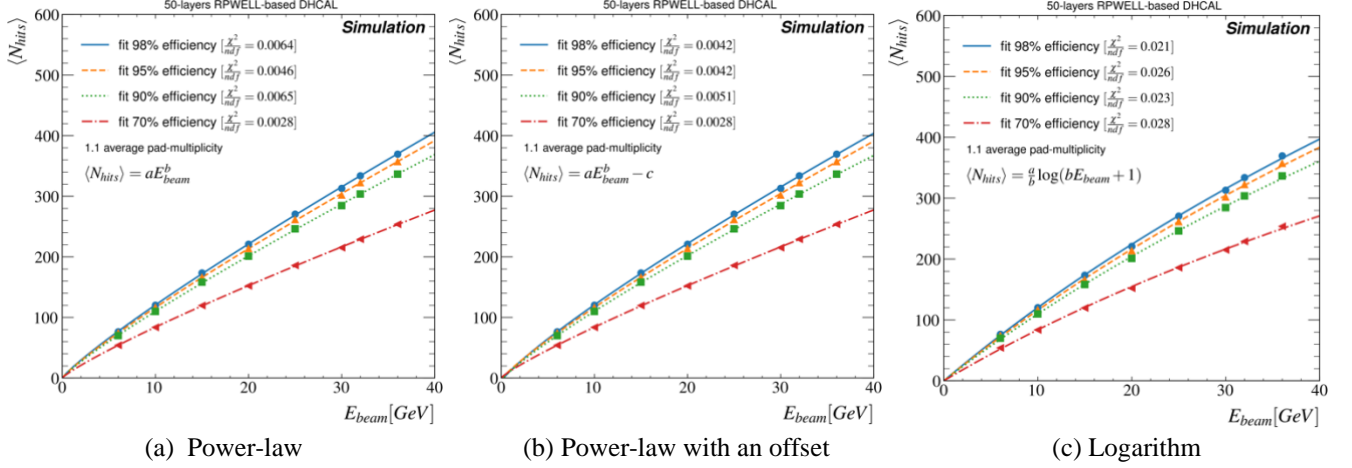


**Figure 37:** The calorimeter response with 98% (blue dots), 95% (orange up-pointing triangles), 90% (green squares), and 70% (red left-pointing triangles) MIP detection efficiency. The response is obtained using (a) power-law, (b) power-law with an offset, and (c) logarithmic parametrizations.

**Table 4:** A summary of the fit parameters of the calorimeter response (Figure 37).

| Response Function  | MIP-Detection Efficiency | a                | b                 | c               | $\frac{\chi^2}{ndf}$ |
|--|--------------------------|------------------|-------------------|-----------------|----------------------|
| $\langle N_{hits} \rangle = a \cdot E_{beam}^b$              | 98%                      | $16.04 \pm 0.23$ | $0.88 \pm 0.005$  |                 | 0.0064               |
|  | 95%                      | $15.45 \pm 0.19$ | $0.88 \pm 0.004$  |                 | 0.0046               |
|  | 90%                      | $14.72 \pm 0.22$ | $0.87 \pm 0.005$  |                 | 0.0065               |
|  | 70%                      | $11.51 \pm 0.13$ | $0.86 \pm 0.004$  |                 | 0.0028               |
| $\langle N_{hits} \rangle = a \cdot E_{beam}^b - c$          | 98%                      | $17.95 \pm 1.2$  | $0.85 \pm 0.02$   | $5.7 \pm 3.4$   | 0.0042               |
|  | 95%                      | $16.27 \pm 1.07$ | $0.86 \pm 0.02$   | $2.5 \pm 3.2$   | 0.0042               |
|  | 90%                      | $16.23 \pm 1.23$ | $0.85 \pm 0.02$   | $4.5 \pm 3.5$   | 0.0051               |
|  | 70%                      | $11.35 \pm 0.75$ | $0.87 \pm 0.02$   | $-0.49 \pm 2.2$ | 0.0028               |
| $\langle N_{hits} \rangle = \frac{a}{b} \log(1 + bE_{beam})$ | 98%                      | $13.04 \pm 0.18$ | $0.017 \pm 0.002$ |                 | 0.021                |
|  | 95%                      | $12.55 \pm 0.20$ | $0.017 \pm 0.002$ |                 | 0.026                |
|  | 90%                      | $11.91 \pm 0.18$ | $0.018 \pm 0.002$ |                 | 0.023                |
|  | 70%                      | $9.17 \pm 0.18$  | $0.020 \pm 0.002$ |                 | 0.028                |

The fit of the power-law with an offset to the calorimeter response yields variations in the offset term for different MIP detection efficiencies without a consistent trend and with substantial uncertainties. It seems that the additional degree of freedom of this parametrization weakens the fit, which might explain why the CALICE collaboration abandoned it. The rest of our analysis concentrates on the reconstruction methods based on the power-law and the logarithmic parametrizations.

Figure 38 shows the bias of the pion energy reconstruction as a function of the beam energy for the (a) power-law and (b) logarithmic parametrizations. The bias measured with the former is smaller than the one measured with the latter, for which large bias is measured at low and high energy values.

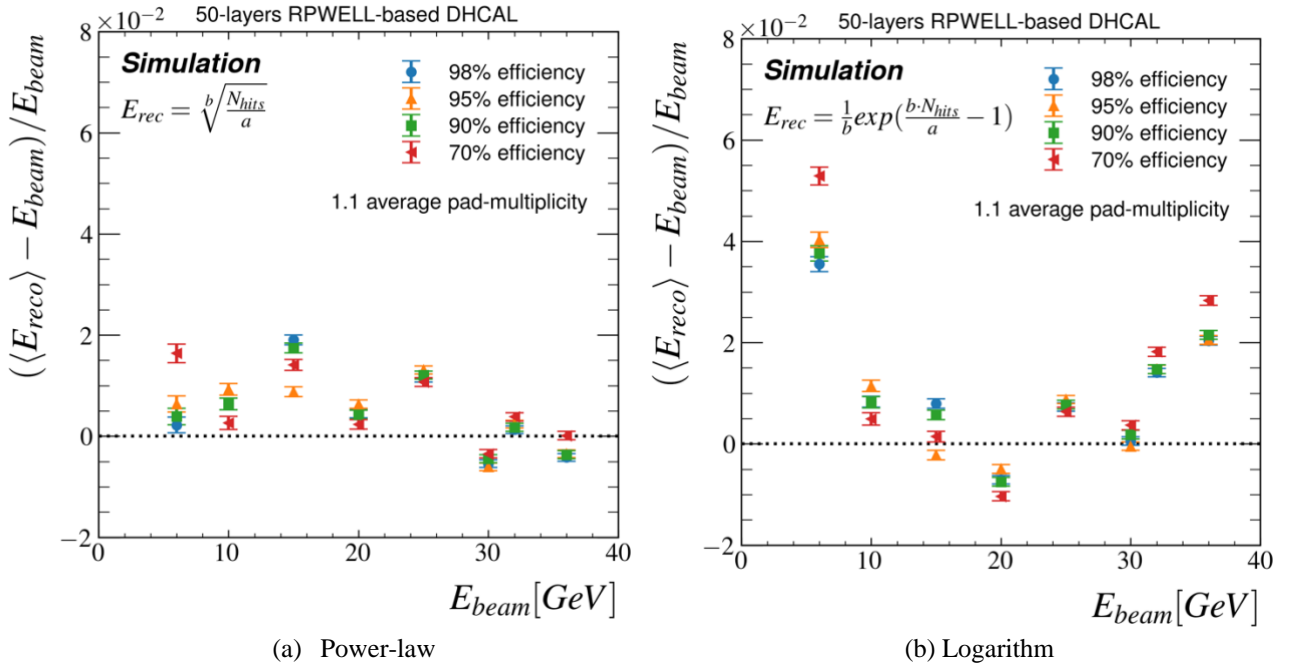


**Figure 38:** The pion energy reconstruction bias of the (a) power-law and (b) logarithmic parametrizations. Results obtained with 98% (blue dots), 95% (orange up-pointing triangles), 90% (green squares), and 70% (red left-pointing triangles) MIP-detection efficiencies.

Figure 39 presents the relative energy resolution for the different MIP detection efficiency values of the (a) power-law and (b) logarithmic parametrizations. Table 5 lists the fit parameters and their corresponding uncertainties. Comparing the relative energy resolution obtained with the 98% and 70% MIP detection efficiency values, we assess the effects of the MIP detection efficiency. A difference of 0.4% (1.4%) and 1.1% (1.3%) is measured with the power-law (logarithmic) parametrization for the stochastic and constant terms, respectively. This indicates that under the power-law parametrization, the relative energy resolution is less sensitive to uniform changes in the MIP detection efficiency in the tested energy range. Moreover,

the relative energy resolution obtained with the power-law parametrization is superior to that obtained with the logarithmic one, as indicated by a 2% smaller constant term.

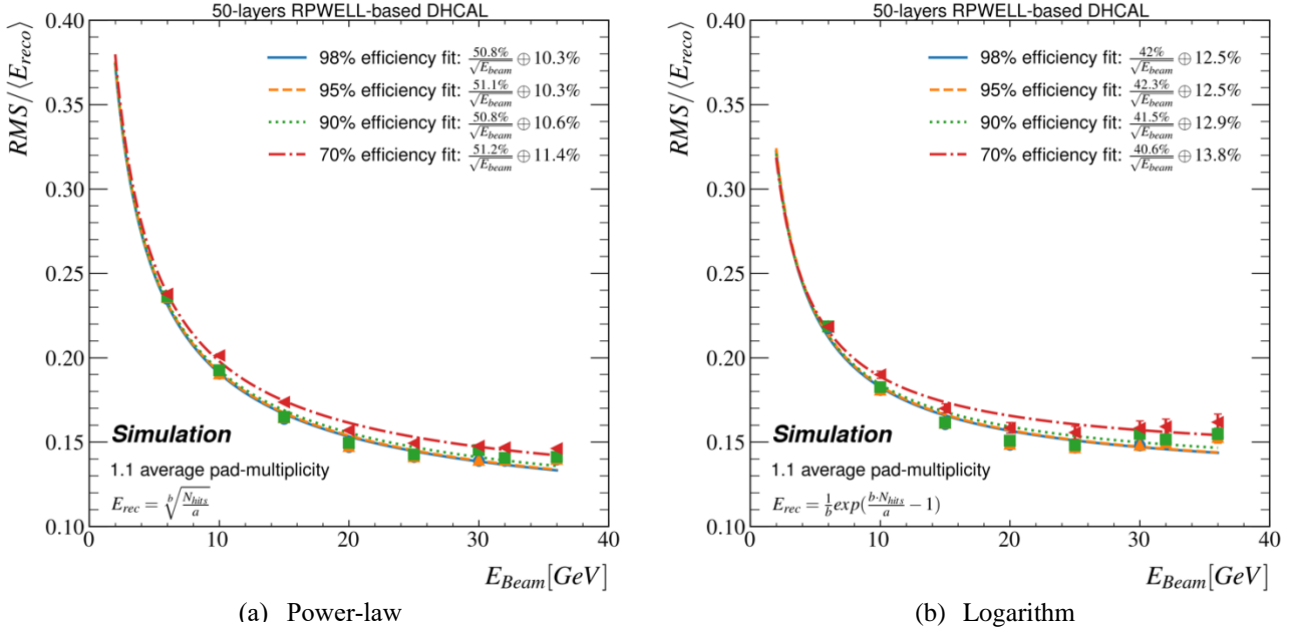


**Figure 39:** The energy resolution extracted using the (a) the power-law and (b) the logarithmic parametrizations; Simulated with 98% (blue dots), 95% (orange up-pointing triangles), 90% (green squares), and 70% (red left-pointing triangles) MIP-detection efficiency.

**Table 5:** A summary of the relative energy resolution using 98%, 95%, 90%, and 70% MIP-detection efficiency for the power-law and logarithmic parametrizations.

| Calorimeter Response Parametrization | MIP-Detection Efficiency | S [% GeV]          | C [%]              | $\frac{\chi^2}{ndf}$ |
|--------------------------------------|--------------------------|--------------------|--------------------|----------------------|
| Power-law                            | 98%                      | 50.8 + (0.2, -0.3) | 10.3 ± 0.06        | 0.00078              |
|                                      | 95%                      | 51.1 + (0.3, -0.2) | 10.3 ± 0.04        | 0.00079              |
|                                      | 90%                      | 50.8 ± 0.2         | 10.6 ± 0.07        | 0.00085              |
|                                      | 70%                      | 51.2 ± 0.2         | 11.4 ± 0.05        | 0.00041              |
| Logarithm                            | 98%                      | 42 + (0.4, -0.5)   | 12.5 ± 0.4         | 0.0016               |
|                                      | 95%                      | 42.3 + (0.4, -0.5) | 12.5 ± 0.4         | 0.0016               |
|                                      | 90%                      | 41.5 + (0.5, -0.6) | 12.9 ± 0.4         | 0.0017               |
|                                      | 70%                      | 40.6 + (0.7, -0.8) | 13.8 + (0.6, -0.5) | 0.001                |

### 5.2.3 The Effect of Pad-Multiplicity

We evaluated the DHCAL performance with two pad-multiplicity distributions (average values of 1.1 and 1.6) at a fixed 98% MIP detection efficiency. The distribution with an average of 1.1 was measured with an RPWELL-based sampling element in a test-beam experiment described in [58]. The average pad-multiplicity of 1.6 was reported for the RPC sampling elements used by the CALICE collaboration [20]. Figure 40 shows the used pad-multiplicity distributions used.

Yielding the best performance in subsection 5.2.2, the power-law parametrization is used in the following. Figure 41 shows the calorimeter response to pions, using the two distributions of pad-multiplicity. The ratio between the average number of hits per event measured with the two distributions is compatible with the ratio of their average values (1.6:1.1). Figure 42 shows their (a) energy reconstruction bias and (b) relative energy resolution. The energy reconstruction bias is similar in both pad-multiplicity distributions, while the relative energy resolution is worse with the higher pad multiplicity.

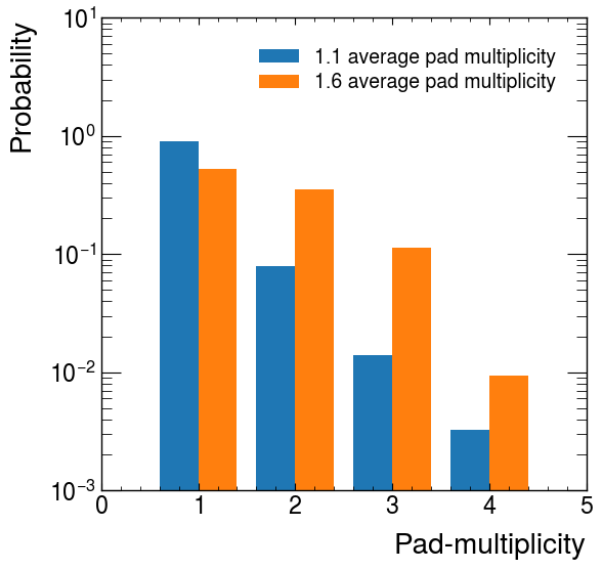


**Figure 40:** The pad-multiplicity distributions used for simulating average pad-multiplicity of 1.1 and 1.6.

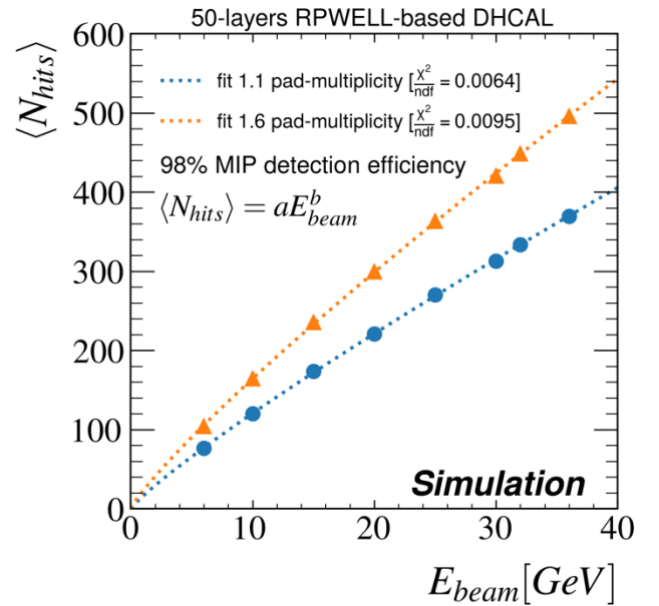


**Figure 41:** Calorimeter response with an average pad-multiplicity of 1.1 (blue circles) and 1.6 (orange triangles).

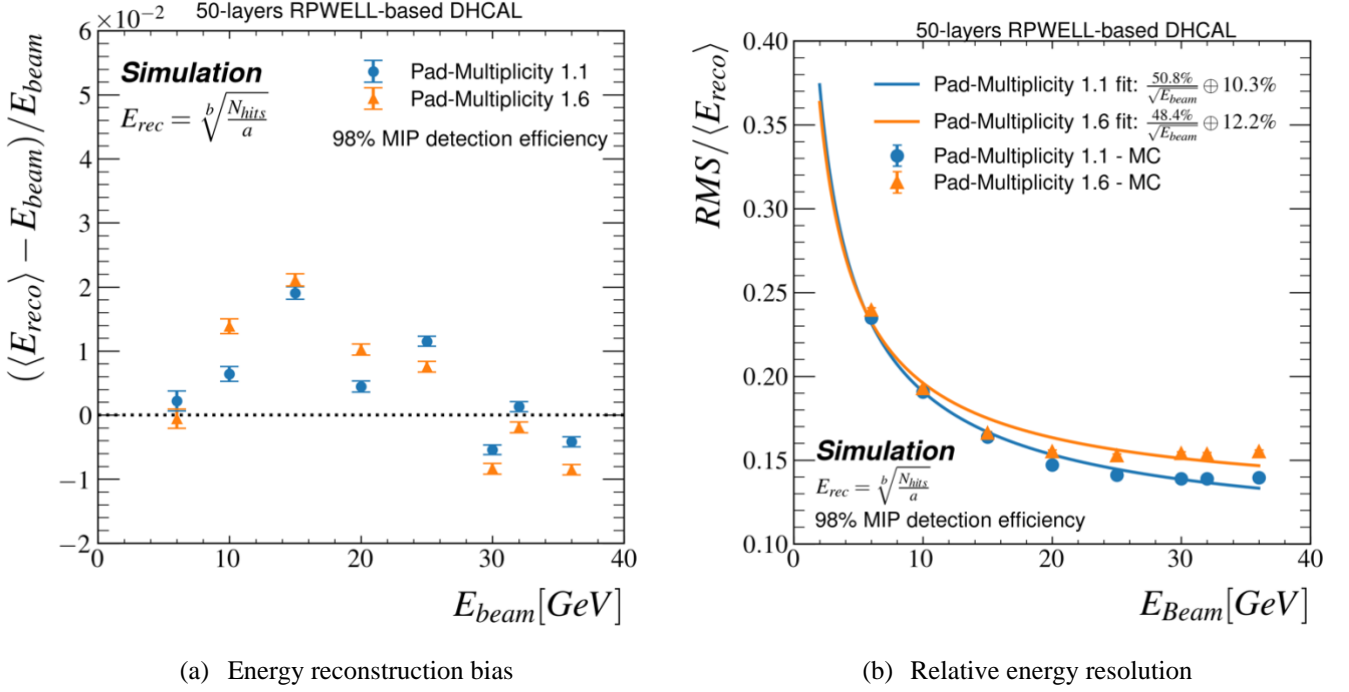


**Figure 42:** The (a) energy reconstruction bias and (b) relative energy resolution of an average pad-multiplicity of 1.1 (blue circles) and 1.6 (orange triangles) obtained with the power-law response parametrization.

### 5.3 Discussion

We studied the expected performance of a 50-layers RPWELL-based DHCAL module using a GEANT4-based simulation. We evaluated the expected pion energy resolution resulting from an energy reconstruction based on three different parametrizations, various MIP detection efficiency values, and two distributions of pad-multiplicity. In the context of particle flow calorimetry, we focused on pions at an energy range of 6–36 GeV [20].

Following [20, 39, 77], we used three optional parametrizations for the calorimeter response: a power-law (eq. 6), a power-law with an offset (eq. 7), and a logarithmic (eq. 8) one. The power-law parametrization is shown to be superior, providing the most accurate energy reconstruction in terms of bias and relative energy resolution.

Table 6 summarizes the expected relative pion energy resolution of an RPWELL-based DHCAL with sampling elements with various MIP detection efficiencies and pad-multiplicity distributions using the power-law parametrization. The measured performance of an RPC Fe-DHCAL is also shown. Efficiency values at the range of 70% to 98% were tested. The former serves as an extreme and non-realistic case

study, and the latter represents a close to optimal performance. For these values, the effect of the MIP detection efficiency on the DHCAL relative energy resolution is about  $\sim 1.1\%$  (dominated by the constant term). The relative energy resolution degrades by  $\sim 2\%$  for pad multiplicity distribution with an average of 1.6 compared to 1.1.

For larger average pad-multiplicity, the probability of two nearby shower fragments overlapping is larger. In a digital readout scheme, such overlap results in the loss of information. This effect is more pronounced for the EM component in the hadronic showers, saturating, even more, this component relative to the hadronic one. Such non-compensating calorimeters are more sensitive to the fluctuations of the EM component fraction, contributing to the constant term of the relative energy resolution [22] – consistent with our observations.

**Table 6:** A summary of the energy resolution of different MIP detection efficiency and average pad-multiplicity values. The energy reconstruction is based on the power-law parametrization. For comparison, the last row includes the results of the CALICE RPC Fe-DHCAL, which includes offline software compensation [20].

| Average Pad-Multiplicity  | MIP-Detection Efficiency | S [% GeV]            | C [%]           |                |
|---------------------------|--------------------------|----------------------|-----------------|----------------|
| 1.1                       | 98%*                     | $50.8 + (0.2, -0.3)$ | $10.3 \pm 0.06$ |                |
| 1.1                       | 95%*                     | $51.1 + (0.3, -0.2)$ | $10.3 \pm 0.04$ |                |
| 1.1                       | 90%*                     | $50.8 \pm 0.2$       | $10.6 \pm 0.07$ |                |
| 1.1                       | 70%*                     | $51.2 \pm 0.2$       | $11.4 \pm 0.05$ |                |
| 1.6                       | 98%*                     | $48.4 \pm 0.3$       | $12.2 \pm 0.1$  |                |
| CALICE<br>Fe-DHCAL [20]** | 1.69                     | 97%                  | $51.5 \pm 1.5$  | $10.6 \pm 0.5$ |

\* Uniform detection efficiency    \*\* Using software compensation

In these studies, we assumed uniform MIP detection efficiency and pad-multiplicity across the 50 sampling elements (a perfect calibration). A realistic simulation should take into account also non-uniformities in the response. We expect that non-uniformities will broaden the distribution of the number of hits for given pion energy (e.g., Figure 33), resulting in a degradation of the relative energy resolution. Finally, in order to optimize the properties of future DHCAL, they should be studied within a complete particle flow experiment framework [30, 31]. E.g., the MIP detection efficiency and average pad-multiplicity are expected to affect the DHCAL performance also in its contribution to the confusion term and the jet energy resolution.

Relative to the RPC-based Fe-DHCAL [20] (Table 6), an RPWELL-based DHCAL with 98% MIP detection efficiency and 1.1 average pad-multiplicity is expected to yield similar stochastic and constant

terms. It should be noted that the data analysis of the CALICE collaboration is more advanced [20]. It considers the hit-density across adjacent layers to compensate for the saturation in events with a large fraction of the EM component.

The MM studies focused on the DHCAL response [39], and the relative energy resolution is not reported. Thus, the RPWELL- and MM-DHCAL are compared in terms of their response. The operation principle of the two technologies is similar, and they have minor differences in the material budget (see section 4.2). Therefore, as expected, Table 7 shows that their calorimetric response is similar.

**Table 7:** A comparison of the calorimeter response to pions with simulated results of RPWELL technology and measured results of virtual MM DHCAL [39]. The measurements of the virtual MM were conducted by measuring for a single sampling element the average number of hits per pion energy as a function of the distance of the sampling element from the shower start. The response is presented using the logarithmic parametrization.

| Technology | Response Function  | MIP-Detection Efficiency | a                | b                 |
|------------|--|--------------------------|------------------|-------------------|
| RPWELL     | $\langle N_{hits} \rangle = \frac{a}{b} \log(1 + bE_{beam})$ | 98%*                     | $13.04 \pm 0.18$ | $0.017 \pm 0.002$ |
|            |  | 95%*                     | $12.55 \pm 0.20$ | $0.017 \pm 0.002$ |
|            |  | 90%*                     | $11.91 \pm 0.18$ | $0.018 \pm 0.002$ |
| MM [39]    |  | 96.6%                    | 12.31            | 0.0088            |

\* Assuming uniform detection efficiency



## Chapter 6: Conclusions and Outlook

The presented research targets the development of an RPWELL-based DHCAL. It is a part of an ongoing R&D effort towards particle flow calorimetry, aiming at jet energy resolution superior to the one measured in today's state-of-the-art particle physics experiments.

The DHCAL sampling elements are required to have high MIP detection efficiency and low pad-multiplicity – ideally of a single hit (channel with signal above threshold) per particle. Our group at WIS has already demonstrated that an RPWELL detector could meet the requirements of a DHCAL sampling element. The robust detector was operated at harsh radiation conditions, demonstrating discharge-free operation and 1.1 average pad-multiplicity at 98% average MIP detection efficiency, while operated using an environment-friendly gas mixture.

In direct continuation, this work consists of three projects:

- a) The development of a large-area RPWELL sampling element. Including detector design, construction techniques, prototypes assembly, and tests with analog readout and semi-digital readout electronics in test beam facilities
- b) The construction of a small MPGD-based DHCAL prototype, its testing in low energy pion beam, and a detailed comparison to GEANT4-based simulation
- c) Simulation study of the expected performance of a 50-layers RPWELL-based DHCAL module

The main achievements of this work are summarized below:

1. **The construction of the first large (50×50 cm<sup>2</sup>) RPWELL detector with a maximum acceptance (no dead areas in the gas volume):** Testing a few prototypes in muon beam, we proved the robustness of the epoxy-based coupling of the WELL electrode to the RP. Nevertheless, two problems are yet to be solved. The first is the significant gain non-uniformity caused by large thickness variations of the electrodes. The second is occasional electrical discharges attributed to epoxy residuals in the WELL

electrode holes. These problems were addressed by our group. This study resulted in one publication [78].

2. **The operation of the first RPWELL-based sampling element with a semi-digital readout system:** We reached a significant milestone proving the effective RPWELL/MICROROC coupling. This paved the way towards operating a small MPGD-based DHCAL prototype and motivated replacing the 0.8-mm-thick WELL electrode with a 0.4 mm thick one.
3. **The operation of the first MPGD-based DHCAL prototype, comprising MM and RPWELL sampling elements:** The small DHCAL prototype, comprising six MM and two RPWELL sampling elements, was assembled and tested in a low-energy pion beam. Despite being operated at low-efficiency conditions, the data collected with the small MPGD-based DHCAL prototype was successfully used to validate the simulation framework we developed. This study resulted in two publications [78, 79]. A third publication is in preparation.
4. **The development and validation of a GEANT4-based DHCAL simulation framework:** A good agreement was shown between the data and the simulation for a DHCAL with a configuration resembling the one used in the test beam. This proves the validity and effectiveness of the simulation framework, which can be used for advanced optimization studies.
5. **The first estimation of the expected performance of a 50-layers RPWELL-based DHCAL:** We simulated the response of full-size DHCAL comprising 50 alternating layers of steel plates and RPWELL-based sampling-element to pions at the energy range of 6-36 GeV. Assuming 98% MIP detection efficiency and 1.1 average pad-multiplicity, the obtained relative pion energy resolution,  $\frac{\sigma}{E[GeV]} = \frac{(50.8 \pm 0.3)\%}{\sqrt{E[GeV]}} \oplus (10.3 \pm 0.06)\%$ , suggests that an RPWELL-based DHCAL could enable the targeted jet-energy resolution using particle flow calorimetry [13]. This performance is comparable to other studied technologies, RPC and MM. Relative to the RPC, the main advantage of an RPWELL is the lower average pad-multiplicity and its operation using environment-friendly gas mixtures. Being a robust and cost-effective detector, the RPWELL could be advantageous relative to the MM. A publication summarizing this work is in preparation.
6. **The evaluation of the effects of MIP detection efficiency and pad-multiplicity on single pion energy resolution:** DHCAL Sampling elements are often characterized in terms of MIP detection efficiency and average pad-multiplicity. Nevertheless, to the best of our knowledge, their effect the single pion energy resolution of a DHCAL was not quantified. Assuming uniform response, we have

shown that sampling elements with a MIP detection efficiency of 70% results in a relative energy resolution that is only 1% inferior, relative to 98% efficiency. For sampling elements with 98% MIP detection efficiency, about 2% degradation in resolution is expected when increasing the average pad-multiplicity from 1.1 to 1.6. Future studies should focus on the performance of the DHCAL prototype, mainly MIP detection efficiency and pad-multiplicity, in the context of the confusion term – the ability to correctly associate energy deposition in the calorimeter with the original impinging particle. Their impact on the jet energy resolution should be tested and studied as part of a complete particle flow algorithm.

The work presented in this thesis motivates improving the detector design and tightening the quality control criteria in its assembly procedure. Since the completion of this work, new and improved sampling elements were built and tested under muon beam at CERN. They are based on 0.4-mm-thick WELL electrodes with less than 5% thickness variations and employ a new electrode design and gluing technique. Preliminary analysis of the test beam data shows an improved gain uniformity (less than 10% variations) and MIP detection efficiency (higher than 90%). A study of a new and improved DHCAL module will follow.



# References

- [1] T. C. S. Group, *CEPC Conceptual Design Report: Volume 2 - Physics & Detector*, (2018).
- [2] G. Apollinari, I. Béjar Alonso, O. Brüning, P. Fessia, M. Lamont, L. Rossi and L. Tavian, *High-Luminosity Large Hadron Collider (HL-LHC): Technical Design Report V. 0.1*, CERN, Geneva, (2017).
- [3] G. Aad, T. Abajyan, B. Abbott, J. Abdallah, S. Abdel Khalek, O. Abdinov, R. Aben, B. Abi, O. AbouZeid, et al., *Technical Design Report for the Phase-I Upgrade of the ATLAS TDAQ System*, (2013).
- [4] T. Kawamoto, S. Vlachos, L. Pontecorvo, J. Dubbert, G. Mikenberg, P. Iengo, C. Dallapiccola, C. Amelung, L. Levinson, et al., *New Small Wheel Technical Design Report*, (2013).
- [5] H. Baer, T. Barklow, K. Fujii, Y. Gao and A. Hoang, *The International Linear Collider Technical Design Report - Volume 2: Physics, ... Prepr. arXiv13066352 2*, (2013).
- [6] T. Behnke, J. E. Brau, B. Foster, J. Fuster, M. Harrison, J. M. Paterson, M. Peskin, M. Stanitzki, N. Walker, et al., *The International Linear Collider Technical Design Report - Volume 1: Executive Summary*, (2013).
- [7] *CLIC Conceptual Design Report (CDR)*<http://project-clic-cdr.web.cern.ch/project-clic-cdr/> (8 December 2017).
- [8] Volume I - Physics & Detector, *CEPC-SPPC: Preliminary Conceptual Design Report; Volume I - Physics & Detector*, (2015).
- [9] *FCC-ee | The FCC-ee design study*<http://tlep.web.cern.ch/> (8 December 2017).
- [10] A. Bernstein, T. Bienz, A. Caldwell, L. Chen, M. Derrick, I. Gialas, A. Hamri, R. Imlay, S. Kartik, et al., *Beam tests of the ZEUS barrel calorimeter*, *Nucl. Instruments Methods Phys. Res. Sect. A Accel. Spectrometers, Detect. Assoc. Equip.* **336**, North-Holland, (1993) 23.
- [11] M. Aaboud, G. Aad, B. Abbott, O. Abdinov, B. Abeloos, S. H. Abidi, O. S. AbouZeid, N. L. Abraham, H. Abramowicz, et al., *Determination of jet calibration and energy resolution in proton–proton collisions at  $\sqrt{s} = 8\text{ TeV}$  using the ATLAS detector*, *Eur. Phys. J. C* **2020 8012 80**, Springer, (2020) 1.
- [12] V. Khachatryan, A. M. Sirunyan, A. Tumasyan, W. Adam, E. Asilar, T. Bergauer, J. Brandstetter, E. Brondolin, M. Dragicevic, et al., *Jet energy scale and resolution in the CMS experiment in pp collisions at 8 TeV*, *J. Instrum.* **12**, (2017) P02014.
- [13] M. A. Thomson, *Particle flow calorimetry and the PandoraPFA algorithm*, *Nucl. Instrum. Methods Phys. Res. A* **611**, (2009) 25.
- [14] *The CALICE Collaboration*<https://twiki.cern.ch/twiki/bin/view/CALICE/SoftwareMain> (18 December 2017).
- [15] S. C. Di Lorenzo, S. Callier, J. Fleury, F. Dulucq, C. De La Taille, G. M. Chassard, L. Raux and N. Seguin-Moreau, *SPIROC: design and performances of a dedicated very front-end electronics for an ILC Analog Hadronic CALorimeter (AHCAL) prototype with SiPM read-out*, *J. Instrum.* **8**, IOP Publishing, (2013) C01027.
- [16] A. Rubin, L. Arazi, S. Bressler, L. Moleri, M. Pitt and A. Breskin, *First studies with the Resistive-Plate WELL gaseous multiplier*, *J. Instrum.* **8**, (2013) P11004.

- 
- [17] L. Moleri, P. Bhattacharya, A. E. C. Coimbra, A. Breskin and S. Bressler, *On the localization properties of an RPWELL gas-avalanche detector*, *J. Instrum.* **12**, (2017) P10017.
- [18] L. Moleri, F. D. Amaro, L. Arazi, C. D. R. Azevedo, A. Breskin, A. E. C. Coimbra, E. Oliveri, F. A. Pereira, D. S. Renous, et al., *In-beam evaluation of a medium-size Resistive-Plate WELL gaseous particle detector*, *J. Instrum.* **11**, IOP Publishing, (2016) P09013.
- [19] L. Moleri, F. D. Amaro, L. Arazi, C. D. R. Azevedo, E. Oliveri, M. Pitt, J. Schaarschmidt, D. Shaked Renous, J. M. F. dos Santos, et al., *The Resistive-Plate WELL with Argon mixtures – A robust gaseous radiation detector*, *Nucl. Instruments Methods Phys. Res. Sect. A Accel. Spectrometers, Detect. Assoc. Equip.* **845**, (2016) 262.
- [20] M. Chefdeville, J. Repond, J. Schlereth, J. R. Smith, D. Trojand, L. Xia, Q. Zhang, J. Apostolakis, C. Grefe, et al., *Analysis of Testbeam Data of the Highly Granular RPC-Steel CALICE Digital Hadron Calorimeter and Validation of Geant4 Monte Carlo Models* The CALICE Collaboration, (2019).
- [21] P.A. Zyla et al. (Particle Data Group), *Prog. Theor. Exp. Phys.* 2020, 083C01 (2021) and 2021 update.
- [22] R. Wigmans, *Calorimetry: Energy Measurement in Particle Physics*, 2nd ed., Oxford University Press, 2017, (2017).
- [23] CALICE Collaboration, *A New Approach to Software Compensation for the CALICE AHCAL*, (2010).
- [24] S. Lee, M. Livan and R. Wigmans, *Dual-Readout Calorimetry*, (2017).
- [25] F. Cavallari, *Performance of calorimeters at the LHC*, *J. Phys. Conf. Ser.* **293**, Institute of Physics Publishing, (2011).
- [26] A. Ebrahimi and I. Arsanjan, *Jet Energy Measurements at ILC: Calorimeter DAQ Requirements and Application in Higgs Boson Mass Measurements; Jet Energy Measurements at ILC: Calorimeter DAQ Requirements and Application in Higgs Boson Mass Measurements*, University of Hamburg, (2017).
- [27] M. Ruan, *Arbor, a new approach of the Particle Flow Algorithm*, *arXiv Prepr. arXiv1403.4784*, (2014).
- [28] D. Jeans, J.-C. Brient and M. Reinhard, *GARLIC: GAMMA Reconstruction at a Linear Collider experiment*, *J. Instrum.* **7**, (2012) P06003.
- [29] T. Behnke, J. E. Brau, P. N. Burrows, J. Fuster, M. Peskin, M. Stanitzki, Y. Sugimoto, S. Yamada and H. Yamamoto, *The International Linear Collider Technical Design Report - Volume 4: Detectors*, in *ArXiv e-prints* **1306**, (2013).
- [30] F. A. Di Bello, S. Ganguly, E. Gross, M. Kado, M. Pitt, L. Santi and J. Shlomi, *Towards a computer vision particle flow*, *Eur. Phys. J. C* **81**, (2021) 107.
- [31] J. Pata, J. Duarte, J.-R. Vlimant, M. Pierini and M. Spiropulu, *MLPF: efficient machine-learned particle-flow reconstruction using graph neural networks*, *Eur. Phys. J. C* **81**, (2021) 381.
- [32] A. M. Sirunyan, A. Tumasyan, W. Adam, E. Asilar, T. Bergauer, J. Brandstetter, E. Brondolin, M. Dragicevic, J. Erö, et al., *Particle-flow reconstruction and global event description with the CMS detector*, *J. Instrum.* **12**, IOP Publishing, (2017) P10003.
- [33] ATLAS Collaboration, *Jet energy scale and resolution measured in proton-proton collisions at  $\sqrt{s}=13$  TeV with the ATLAS detector*, *Eur. Phys. J. C* **81**, Springer Science and Business Media Deutschland GmbH, (2020).
- [34] C. Adloff, Y. Karyotakis, J. Repond, A. Brandt, H. Brown, K. De, C. Medina, J. Smith, J. Li, et al., *Construction and commissioning of the CALICE analog hadron calorimeter prototype*, *J. Instrum.* **5**, IOP Publishing, (2010) P05004.
- [35] C. Adloff, J. Blaha, J.-J. Blaising, C. Drancourt, A. Espargilière, R. Gaglione, N. Geffroy, Y. Karyotakis, J. Prast, et al., *Hadronic energy resolution of a highly granular scintillator-steel hadron calorimeter using software compensation*

- techniques, J. Instrum.* **7**, (2012) P09017.
- [36] H. Aihara, P. Burrows and M. Oreglia, *SiD Letter of Intent, arXiv.org*, (2009).
- [37] T. I. C. The ILD Concept Group, *The International Large Detector: Letter of Intent*, (2010).
- [38] S. Mannai, K. Manai, Y. Haddad, I. Laktineh and E. Cortina, *High granularity Semi-Digital Hadronic Calorimeter using GRPCs, Nucl. Instruments Methods Phys. Res. Sect. A Accel. Spectrometers, Detect. Assoc. Equip.* **718**, North-Holland, (2013) 91.
- [39] M. Chefdeville, *Micromegas for Particle Flow Calorimetry*, in *Proceedings, Int. Conf. Calorim. High Energy Front. (CHEF 2013) Paris, Fr. April 22-25, 2013*, (2013).
- [40] J. Yu, E. Baldeomar, K. Park, S. Park, M. Sosebee, N. Tran and A. P. White, *Application of Large Scale GEM for Digital Hadron Calorimetry*, in *Phys. Procedia* **37**, (2012).
- [41] J. Repond, *Analysis of DHCAL Muon Events*, in *TIPP 2011 Conf. Chicago* **4**, (2011).
- [42] C. Adloff, J. Blaha, J. -J. Blaising, M. Chefdeville, A. Dalmaz, C. Drancourt, A. Espargilière, R. Gaglione, N. Geffroy, et al., *Recent results of Micromegas sDHCAL with a new readout chip*, (2012).
- [43] M. Chefdeville, Y. Karyotakis, N. Geffroy, R. Gaglione, C. Adloff, G. Vouters, J. Jacquemier, F. Peltier, A. Dalmaz, et al., *Micromegas for sampling calorimetry, PoS, SISSA*, (2014) 54.
- [44] D. Hong, Y. Zhou, J. Liu, B. Yu, G. Song, L. Shang, Y. Wang, Z. Shen, C. Feng, et al., *Development of compact micro-pattern gaseous detectors for the CEPC digital hadron calorimeter, J. Instrum.* **15**, IOP Publishing, (2020) C09032.
- [45] B. Bilki, F. Corriveau, B. Freund, C. Neubüser, Y. Onel, J. Repond, J. Schlereth and L. Xia, *Tests of a novel design of Resistive Plate Chambers, J. Instrum.* **10**, (2015) P05003.
- [46] C. Collaboration and Others, *First results of the CALICE SDHCAL technological prototype, J. Instrum.* **11**, IOP Publishing, (2016) P04001.
- [47] J. Repond, *Resistive Plate Chambers for Imaging Calorimetry - The DHCAL*, in *J. Instrum.* **9**, (2014).
- [48] L. Arazi, C. D. R. Azevedo, A. Breskin, S. Bressler, L. Moleri, H. N. da Luz, E. Oliveri, M. Pitt, A. Rubin, et al., *Beam studies of the segmented resistive WELL: A potential thin sampling element for digital hadron calorimetry, Nucl. Instruments Methods Phys. Res. Sect. A Accel. Spectrometers, Detect. Assoc. Equip.* **732**, Elsevier, (2013) 199.
- [49] R. Chechik, A. Breskin, C. Shalem and D. Mörmann, *Thick GEM-like hole multipliers: properties and possible applications, Nucl. Instruments Methods Phys. Res. Sect. A Accel. Spectrometers, Detect. Assoc. Equip.* **535**, (2004) 303.
- [50] R. Cardarelli, R. Santonico, A. Di Biagio and A. Lucci, *Progress in resistive plate counters, Nucl. Instruments Methods Phys. Res. Sect. A Accel. Spectrometers, Detect. Assoc. Equip.* **263**, (1988) 20.
- [51] J. T. Bromley, *Investigation of the Operation of Resistive Plate Chambers*, The University of Manchester, (1994).
- [52] S. Bressler, L. Arazi, L. Moleri, M. Pitt, A. Rubin and A. Breskin, *Recent advances with THGEM detectors, J. Instrum.* **8**, (2013) C12012.
- [53] D. Shaked Renous, A. Roy, A. Breskin and S. Bressler, *Gain stabilization in Micro Pattern Gaseous Detectors: methodology and results, J. Instrum.* **12**, IOP Publishing, (2017) P09036.
- [54] L. Moleri, P. Bhattacharya, A. E. C. Coimbra, A. Breskin and S. Bressler, *On the localization properties of an RPWELL gas-avalanche detector, J. Instrum.*, (2017).
- [55] P. Bhattacharya, L. Moleri and S. Bressler, *Signal formation in THGEM-like detectors, Nucl. Instruments Methods Phys.*

- Res. Sect. A Accel. Spectrometers, Detect. Assoc. Equip.*, (2019).
- [56] P. Bhattacharya, A. Tesi, D. Shaked-Renous, L. Moleri, A. Breskin and S. Bressler, *Single-electron spectra in RPWELL-based detectors*, *J. Instrum.* **16**, IOP Publishing, (2021) P05004.
- [57] S. Bressler, L. Moleri, M. Pitt, S. Kudella, C. D. R. Azevedo, F. D. Amaro, M. R. Jorge, J. M. F. dos Santos, J. F. C. de A. Veloso, et al., *First in-beam studies of a Resistive-Plate WELL gaseous multiplier*, *J. Instrum.* **11**, (2016) P01005.
- [58] L. Moleri, F. D. Amaro, L. Arazi, C. D. R. Azevedo, E. Oliveri, M. Pitt, J. Schaarschmidt, D. Shaked Renous, J. M. F. dos Santos, et al., *The Resistive-Plate WELL with Argon mixtures – A robust gaseous radiation detector*, *Nucl. Instruments Methods Phys. Res. Sect. A Accel. Spectrometers, Detect. Assoc. Equip.* **845**, (2017) 262.
- [59] C. M., *Micromegas for Particle Flow Calorimetry*, (2013).
- [60] C. Adloff, M. Chefdeville, A. Dalmaz, C. Drancourt, R. Gaglione, N. Geffroy, J. Jacquemier, Y. Karyotakis, I. Koletsou, et al., *PoS(TIPP2014)054 Resistive Micromegas for Sampling Calorimetry PoS(TIPP2014)054*, in *Technol. Instrum. Part. Phys.*, (2014).
- [61] F. Sauli, *Principles of Operation of Multiwire Proportional and Drift Chambers*, European Organization for Nuclear Research, (1977).
- [62] S. Martoiu, H. Muller, A. Tarazona and J. Toledo, *Development of the scalable readout system for micro-pattern gas detectors and other applications*, *J. Instrum.* **8**, (2013) C03015.
- [63] M. J. French, L. L. Jones, Q. Morrissey, A. Neviani, R. Turchetta, J. Fulcher, G. Hall, E. Noah, M. Raymond, et al., *Design and Results from the APV25, a Deep Sub-Micron CMOS Front-End Chip for the CMS Tracker*, in *Nucl. Instruments Methods Phys. Res. Sect. A Accel. Spectrometers, Detect. Assoc. Equip.*, (2001).
- [64] C. Adloff, J. Blaha, M. Chefdeville, A. Dalmaz, C. Drancourt, F. Dulucq, A. Espargilière, R. Gaglione, N. Geffroy, et al., *MICROROC: MICRO-mesh gaseous structure Read-Out Chip*, *J. Instrum.* **7**, (2012) C01029.
- [65] M. Bianco, P. Loesel, S. Martoiu, O. Sidiropoulou and A. Zibell, *Development and test of a versatile DAQ system based on the ATCA standard*, *Proc. Sci.* **213**, SISSA Medialab, (2015) 202.
- [66] R. Brun and F. Rademakers, *ROOT - An object oriented data analysis framework*, *Nucl. Instruments Methods Phys. Res. Sect. A Accel. Spectrometers, Detect. Assoc. Equip.* **389**, North-Holland, (1997) 81.
- [67] K. Karakostas, T. Alexopoulos and G. Tsipolitis, *A Tracking Program for the RD51 Telescopes*, (2012).
- [68] E. Etzion, Y. Benhammou, J. Ginzburg, M. Ishino, L. Levinson, G. Mikenberg, N. Panikashvili, D. Primor and V. Smakhtin, *The Certification of ATLAS Thin Gap Chambers Produced in Israel and China*, in *IEEE Symp. Conf. Rec. Nucl. Sci. 2004.* **1**, (2004).
- [69] M. Alexeev, R. Birsa, F. Bradamante, A. Bressan, M. Büchele, M. Chiosso, P. Ciliberti, S. Dalla Torre, S. Dasgupta, et al., *THGEM-based photon detectors for the upgrade of COMPASSRICH-1*, *Nucl. Instrum. Methods Phys. Res. A* **732**, (2013) 264.
- [70] M. Alexeev, R. Birsa, F. Bradamante, A. Bressan, M. Büchele, M. Chiosso, P. Ciliberti, S. Dalla Torre, S. Dasgupta, et al., *The gain in Thick GEM multipliers and its time-evolution*, *J. Instrum.* **10**, IOP Publishing, (2015) P03026.
- [71] C. Adloff, J. Blaha, M. Chefdeville, A. Dalmaz, C. Drancourt, A. Espargilière, R. Gaglione, N. Geffroy, D. Girard, et al., *Construction and test of a  $1 \times 1$  m<sup>2</sup> Micromegas chamber for sampling hadron calorimetry at future lepton colliders*, *Nucl. Instruments Methods Phys. Res. Sect. A Accel. Spectrometers, Detect. Assoc. Equip.*, (2013).

- 
- [72] R. O. Duda and P. E. Hart, *Use of the Hough Transformation to Detect Lines and Curves in Pictures*, *Commun. ACM* **15**, ACM PUB27 New York, NY, USA, (1972) 11.
- [73] S. Agostinelli, J. Allison, K. Amako, J. Apostolakis, H. Araujo, P. Arce, M. Asai, D. Axen, S. Banerjee, et al., *GEANT4 - A simulation toolkit*, *Nucl. Instruments Methods Phys. Res. Sect. A Accel. Spectrometers, Detect. Assoc. Equip.* **506**, North-Holland, (2003) 250.
- [74] J. Apostolakis, G. Folger, V. Grichine, A. Howard, V. Ivanchenko, M. Kosov, A. Ribon, V. Uzhinsky and D. H. Wright, *GEANT4 Physics Lists for HEP*, in *IEEE Nucl. Sci. Symp. Conf. Rec.*, (2008).
- [75] *Electromagnetic physics constructors — PhysicsListGuide 10.7 documentation*<https://geant4-userdoc.web.cern.ch/UsersGuides/PhysicsListGuide/html/electromagnetic/index.html> (14 May 2021).
- [76] C. G. Reichelt, J. F. Strube and C. Grefe, *CERN-European Organization for Nuclear Research Particle ID Studies in a Highly Granular Hadron Calorimeter*, (2013).
- [77] B. Bilki, *DHCAL Response to Positrons and Pions*, *Phys. Procedia* **37**, (2012) 317.
- [78] S. Bressler, P. Bhattacharya, A. Breskin, A. E. C. Coimbra, D. Shaked-Renous, A. Tesi, L. Moleri, M. Chefdeville, G. Vouters, et al., *Novel Resistive-Plate WELL sampling element for (S)DHCAL*, *Nucl. Instruments Methods Phys. Res. Sect. A Accel. Spectrometers, Detect. Assoc. Equip.* **958**, (2020).
- [79] D. Shaked Renous, P. Bhattacharya, M. Chefdeville, C. Drancourt, L. Moleri, A. Tesi, A. Coimbra, A. Breskin, S. Bressler, et al., *Towards MPGD-Based (S)DHCAL*, in *J. Phys. Conf. Ser.* **1498**, Institute of Physics Publishing, (2020).
- [80] C. Lippmann, *Particle identification*, *Nucl. Instrum. Methods Phys. Res. A* **666**, (2012) 148.



# Appendix A: Large Area Precision Cathode Boards for ATLAS NSW

The largest phase-I upgrade project for the ATLAS Muon System (Figure A.1) was replacing the present first station in the forward regions with the so-called New Small Wheels (NSWs) during the long-LHC shutdown of 2019-21. Alongside my work on the RPWELL-based DHCAL investigations, I contributed a large amount of time to the NSW sTGC cathode boards quality assurance/quality control (QA/QC) as part of my ATLAS authorship qualification. This appendix includes a concise description of the NSW upgrade

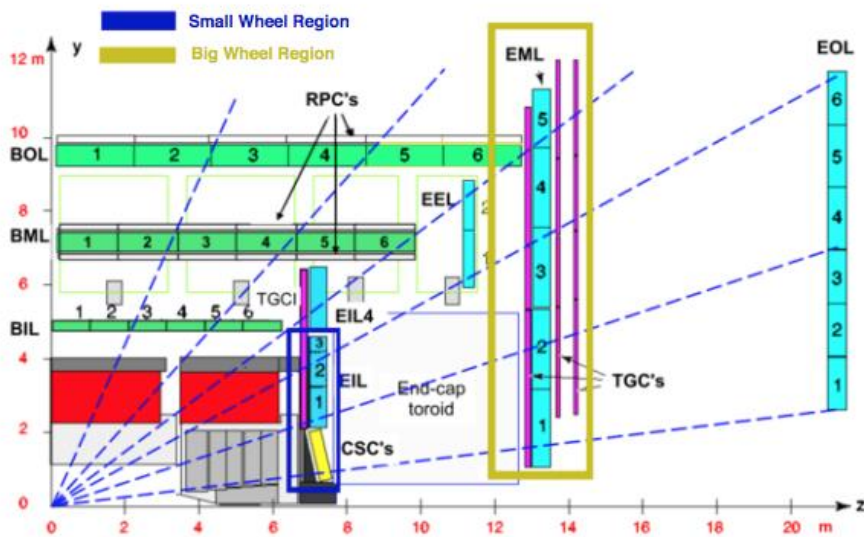


**Figure A.1:** A cross-section of one-fourth of the ATLAS Muon system. The Small Wheel region is marked in a blue frame.

and the significance of the QA/QC for the precision of the muon track reconstruction.

The NSWs (Figure A.2, left) are equipped with eight small and eight large sectors. Each sector contains eight layers of small-strip thin gap chambers (sTGC) arranged in two wedges, “pivot” and “confirm,” for a total active surface area of more than 2500 m<sup>2</sup>. The small and large wedges (Figure A.2, middle and right respectively) consist of three quadruplets.

The sTGC detectors (Figure A.3) consist of a grid of 50  $\mu$ m gold plated tungsten wires at a potential at the order of 2.9 kV, with a 1.8 mm pitch, sandwiched between two cathode planes at a distance of 1.4 mm

from the wire plane. The cathode planes consist of a graphite-epoxy mixture with a typical surface resistivity of 100-200 k $\Omega$ /square sprayed on a 150-200  $\mu\text{m}$  thick prepreg plane. The prepreg is pressed onto a 1.6 mm thick printed circuit board (PCB). One of the cathode planes, the PCB, is covered with precision strips (that run perpendicular to the wires and have 3.2 mm pitch), and on the other pads (covering large trapezoidal surfaces), with the shielding ground on the opposite side of the PCB. The sTGC cathode boards have trapezoidal shapes with surface areas up to 2 m<sup>2</sup>.

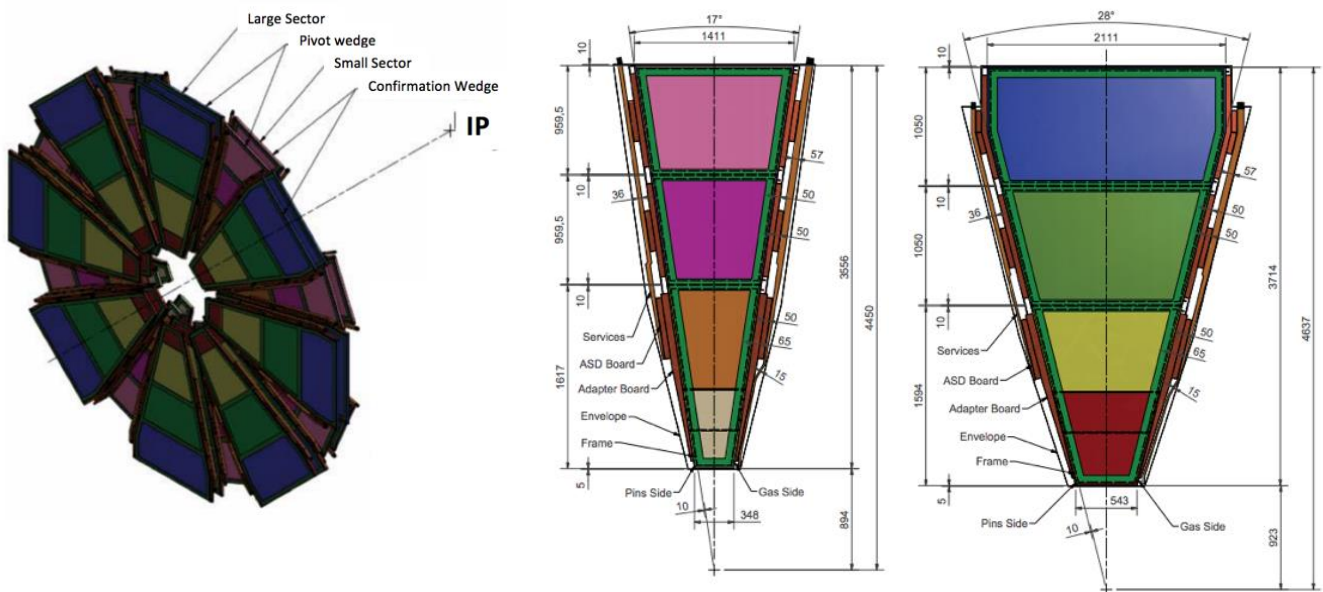


**Figure A.2:** Left: The NSW layout. Middle: The layout of the small sTGC wedge. Right: The layout of the large sTGC wedge.

## sTGC chambers – Precision requirements

The precision requirements imposed on the sTGC cathode boards are derived from the required muon momentum resolution at the trigger and tracking levels:

- Trigger level: track segments should be measured with an angular resolution of approximately one mrad.
- Tracking level: 15%  $p_T$  resolution for 1 TeV muons.

The muon spectrometer measures the momentum of muons through their sagitta in the toroidal magnetic field. A 500  $\mu\text{m}$  sagitta of a 1 TeV muon should be measured with a 10% precision.

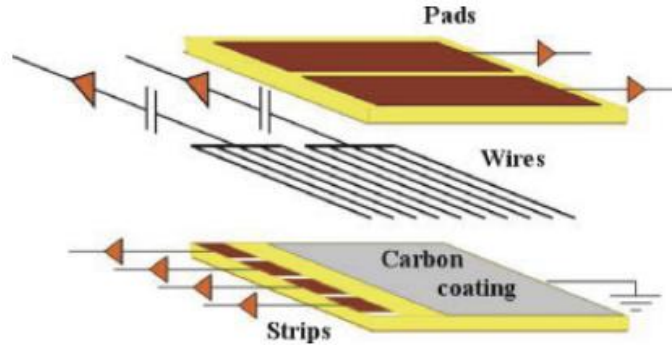


**Figure A.3:** A schematic description of the sTGC detector. A 1.8-mm-pitch grid of 50  $\mu\text{m}$  gold plated tungsten wires positioned between two cathode planes at a distance of 1.4 mm from the wire plane. The cathode planes consist of a graphite-epoxy mixture sprayed on a 150-200  $\mu\text{m}$  thick prepreg plane. The prepreg is pressed onto a PCB. One of the cathode planes, the PCB is covered with strips (3.2 mm pitch), and on the other trapezoidal pads.

For three equidistant wheels,  $i = 1, 2, 3$ , the sagitta can be approximated as  $S = \frac{(k_1 + k_3)}{2} - k_2$ , where  $k_i$  is the measured precision coordinate in each wheel. The error is dominated by the measurement accuracy in the middle station  $\Delta S = \sqrt{\frac{1}{4}\Delta k_1^2 + \Delta k_2^2 + \frac{1}{4}\Delta k_3^2}$  allowing for somewhat poorer precision in the NSW (wheel 1) relative to the precision chambers in the two big wheels (wheels 2 and 3, see Figure A.1). The error in each wheel has three main contributions: the construction precision, the precision of each hit measurement, and the relative alignment between the layers is  $\Delta k_i = \frac{\sigma_{chamber} \oplus \sigma_{hit}}{\sqrt{n} \oplus \sigma_{alignment}}$ .

Given the sTGC hit precision (better than 100  $\mu\text{m}$ ) and the alignment precision in ATLAS (about 40  $\mu\text{m}$ ), the needed precision can be achieved with an accuracy of 40  $\mu\text{m}$  RMS along the precision coordinate (strip position) and 80  $\mu\text{m}$  RMS along the beam direction.

## Cathode boards – Precision requirements

The precision to which the strips and pads patterns are positioned onto the boards is critical for enabling a precise measurement by the assembled quadruplet. The cathode boards are produced in the industry by either CNC machining or chemical etching of copper-plated FR4 boards. An insulating pre-preg layer is pressed on top of the copper readout elements. The material flow of the underlying FR4 boards during the cathode board mechanical and chemical manufacturing and pressing have been found to have a significant

impact on the placement of the copper readout elements. This production feature leads to different kinds of potential non-conformities, i.e., the difference between the design and the actual strip/pad patterns.

Production tolerances are defined for four non-conformities (Table A.1):

- Constant *offset* by which the entire strip pattern is moved up/down along the y-axis
- Pitch *scale* for which the distance between adjacent strips changes gradually while the new pattern stays parallel to the original one
- *Non-parallelism* for which the distance between adjacent strips changes gradually, e.g., at only one edge of the layer, breaking the parallelism of the original pattern
- *Rotation* in the x y plane where the entire pattern is rotated around a specific axis during manufacturing of the layers, e.g., around the axis defined by brass insert

In addition, the position in the beam direction is controlled through the board *thickness* and *flatness*.

The tolerances specified for the production are based on the manufacturers' capabilities and are summarized in Table A.1. These are insufficient for achieving the required tracking momentum resolutions, and software correction is required. Thus, as part of the QA/QC procedure, each stripboard is measured with CMM or FaroArm. The values of the non-conformities are stored in the database to be used by the correction software.

**Table A.1:** The production tolerances verified as part of the cathode board QA/QC procedure.

| Parameter                        | Limit   |                           | Board type<br>(pad/strip) |
|----------------------------------|---|---------------------------|---------------------------|
|                                  | GS1, GL1<br>boards                                      | GS2, GS3, GL2, GL2 boards |                           |
| Average thickness                | Within $\pm 75 \mu\text{m}$ from nominal                |                           | Pad and strip             |
| Flatness                         | $\frac{\text{max} - \text{min}}{2} \leq 35 \mu\text{m}$ |                           | Pad and strip             |
| Angle deviation from nominal     | $\leq 0.01^\circ$                                       | $\leq 0.005^\circ$        | Strip                     |
| Offset (absolute value)          | $\leq 300 \mu\text{m}$                                  |                           | Strip                     |
| Scale (absolute value)           | $\leq 400 \mu\text{m}$                                  |                           | Pad and strip             |
| Non-Parallelism (absolute value) | $\leq 400 \mu\text{m}$                                  |                           | Pad and strip             |

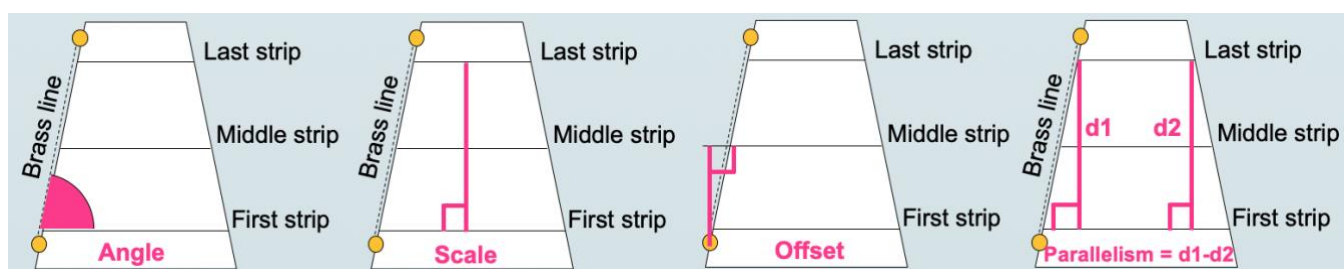


**Figure A.4:** A description of the measured parameters for stripboard QA/QC.

## Cathode board production

There were two production lines: one based on CNC milling and the other on chemical etching. QA/QC assurance tests were performed along with the production. They included visual inspections, electrical tests, and dimension measurements (see QA/QC Tests).

The procedure of the CNC production line at MDT/DAGESH or MDT/Nuova Saltini was as follows:

- Step 1: Production of raw material at MDT Italy; Testing at the Weizmann institute: classification and type of board are decided (strip/pad).
- Step 2: CNC milling at Dagesh Israel; Testing at the Weizmann Institute.
- Step 3: Pre-preg pressing at MDT Italy; Testing at the Weizmann Institute and CERN: repeat set of tests and repair.
- Step 4: Packaging and shipping to the production sites.

The boards produced by MDT/Nuova Saltini are only tested after step 3.

## QA/QC Tests

The QA/QC process of cathode boards arriving from MDT after the pre-preg pressing was under my responsibility. The QA/QC protocol includes the following tests:

- Visual Inspection – verifying there are no visible defects.
- Thickness Measurements (Figure A.5)
- Electrical Testing (Figure A.5)
  - High Voltage Shorts through the pre-preg layer

- Capacitance (Pads)
- Conductivity (strips)

Over 500 boards were processed at CERN as part of the cathode board's production phase. In May and November 2021, the two NSW were installed in the ATLAS experiments, and their commissioning continues in 2022.

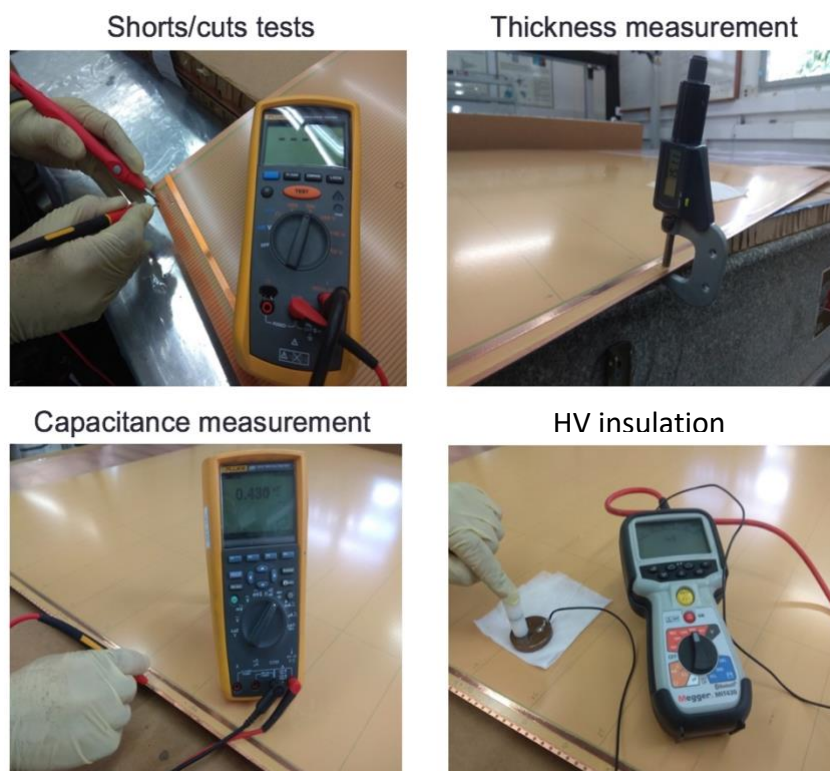


**Figure A.5:** Cathode boards production QA/QC tests

---

## Appendix B: 50×50 cm<sup>2</sup> RPWELL Prototypes Construction Procedure

Four 50×50 cm<sup>2</sup> RPWELL chambers were constructed during this research using the epoxy-based method. In their construction, we used for the first time a single 50×50 cm<sup>2</sup> WELL electrode. The assembly steps are detailed in Figure B.1 (the glass tile assembly) and Figure B.2 (WELL electrode gluing). A summary of the protocol is presented below:

1. Spreading on the anode readout pads a thin and uniform layer of epoxy (Araldite AY103+HY99) mixture with 5% graphite powder (Figure B.1-a and Figure B.1-b).
2. Placing four 25×25 cm<sup>2</sup> tiles of low-resistivity silicate glass, using the frame for alignment (Figure B.1-c).
3. Injecting high-voltage insulation paint into the tiles' interface (Figure B.1-d and Figure B.1-e).
4. Cleaning the excess of the insulation paint from the upper.
5. Manually scanning the interfaces between the tiles with a microscope, verifying coverage of the insulation paint, and minimizing the presence of dust and cleaning cloth's fibers (Figure B.1-f).
6. Using a glass with a thin and uniform layer of epoxy (Araldite AY103+HY99) mixture to transfer a small amount of epoxy to the bottom side of a WELL electrode (Figure B.2-a).
7. Placing the electrode on top of the glass layer, using the frame for alignment (Figure B.2-b).
8. Curing the epoxy under uniform vacuum pressure (Figure B.2-c).
9. Applying conductive epoxy for HV connections between the WELL electrode and an HV-ruler (Figure B.2-d).
10. Closing the chamber by gluing the drift cathode (Figure B.2-e)
11. Curing of the epoxy used for the cathode gluing with weights instead of vacuum (Figure B.2-f) – vacuum pressure warps the cathode in a design lacking internal support structure.

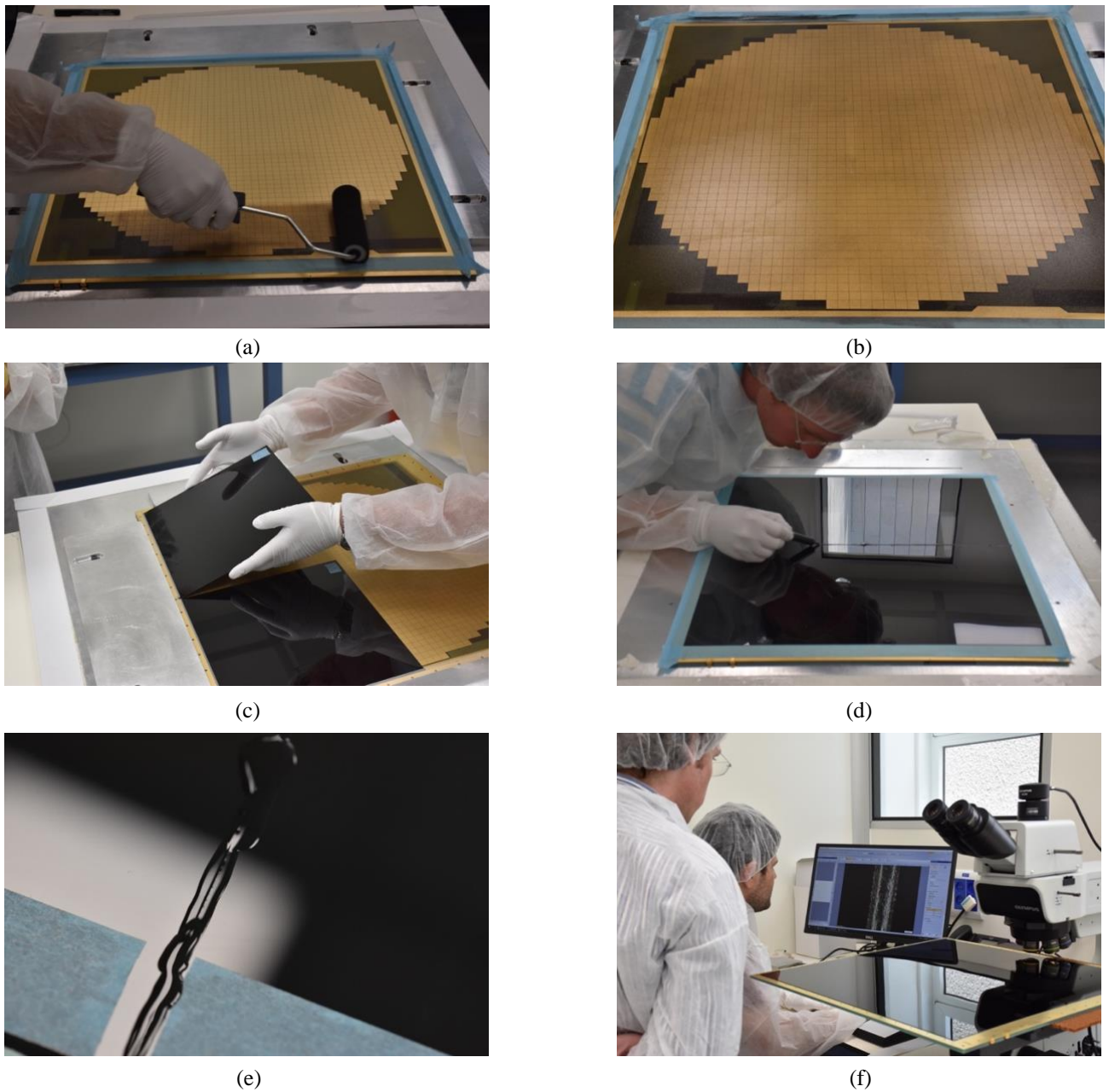
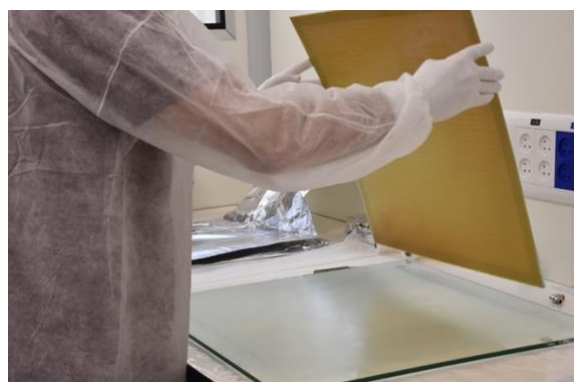
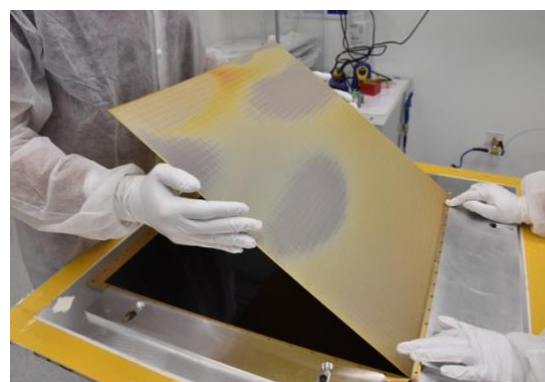


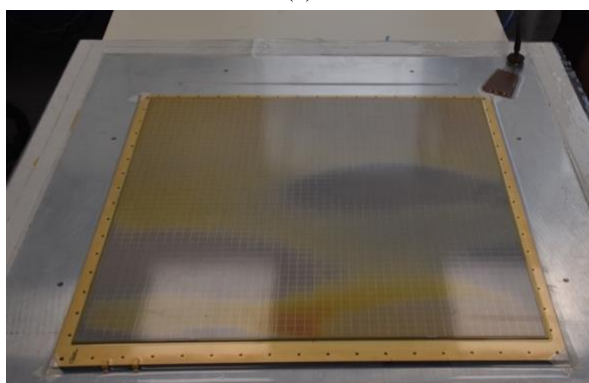
**Figure B.1:** The first part of the construction process of 50×50 cm<sup>2</sup> RPWELL sampling element demonstrated with MICROROC-based readout anode with pads (the same procedure is used for analog strips readout anode). a) spreading on the anode pads a thin and uniform layer of epoxy (Araldite AY103+HY99) mixture with 5% graphite powder; b) picture of the readout pads with the epoxy and graphite mixture; c) placing four 25×25 cm<sup>2</sup> tiles of low-resistivity silicate glass, using the frame for alignment; d) injecting HV insulation paint in the tiles' interface; e) a picture of the interface of two glass tiles, before cleaning the excess from the upper surface; f) manual scanning with a microscope the interface of each pair of tiles, verifying coverage of the insulation paint and minimizing the presence of fibers.



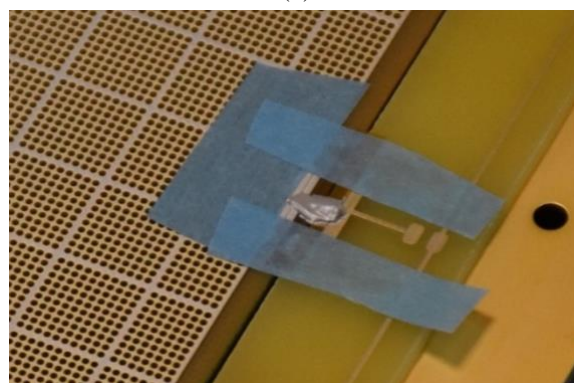
(a)



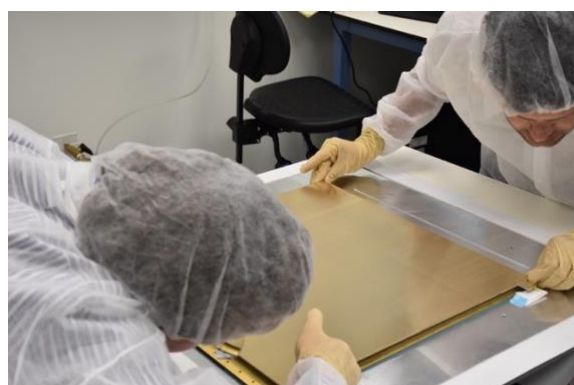
(b)



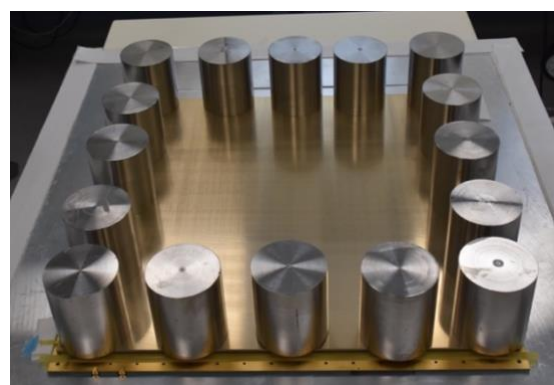
(c)



(d)



(e)



(f)

**Figure B.2:** The second part of the construction process of  $50 \times 50$  cm<sup>2</sup> RPWELL sampling element demonstrated with MICROROC-based readout anode with pads (the same procedure is used for analog strips readout anode). a) glass with a thin and uniform layer of epoxy (Araldite AY103+HY99) mixture is used to transfer a small amount of epoxy to the bottom side of a WELL electrode; b) placing the electrode on top of the glass layer, using the frame for alignment; c) curing the epoxy under uniform vacuum pressure; d) using conductive epoxy to make the HV connections between the WELL electrode and an HV-ruler; e) closing the chamber by placing and gluing the drift cathode; f) curing of the epoxy used for the cathode gluing is done with weights instead of vacuum (vacuum pressure warps the cathode in a design lacking internal support structure).



# Appendix C: Calculation of True Pad-Multiplicity and Hit Detection Efficiency

In subsection 4.1.3, we mention that the true pad-multiplicity and hit detection efficiency (HDE) can be calculated from the experimental measurements of the distribution of the pad-multiplicity and the MIP detection efficiency. In this appendix, we present a method for an analytic calculation of these parameters. The measured distribution of pad-multiplicity incorporates contributions from both the true pad multiplicity (related to the detector's response) and from internal multiplicity originating from the interaction of impinging particle with the detector's material (leaving more than one cluster). Therefore, the calculation consists of two steps:

- 1) Calculation of the HDE and the distribution of pad-multiplicity before the application of HDE
- 2) Calculation of the probability of a hit to have an additional multiplicity due to the impinging particle's interaction with the detector's material

## Calculation of the HDE and the pure pad-multiplicity distribution

Let us consider a specific sampling element in the calorimeter. Let  $\varepsilon_M$  and  $N_m^*$  denote the MIP detection efficiency and the measured number of events with pad-multiplicity  $m$ , respectively. Both  $\varepsilon_M$  and  $N_m^*$  were measured using the methodology of section 4.1.3. Our goal is to extract the pad's hit detection efficiency and the true number of events with pad-multiplicity  $m$  – denoted by  $\varepsilon_h$  and  $N_m$ . In short, we would like to get expressions for the following transformation:

$$\left( \begin{array}{c} \varepsilon_M \\ \{N_m^*\} \end{array} \right) \rightarrow \left( \begin{array}{c} \varepsilon_h \\ \{N_m\} \end{array} \right)$$

The relations can be described as follows:

$$N_m^* = \sum_{n \geq m} \binom{n}{m} N_n \varepsilon_h^m (1 - \varepsilon_h)^{n-m} \quad (\text{C. 1})$$

$$\varepsilon_M = \frac{\sum_{m=1} N_m^*}{N_{events}} \quad (\text{C. 2})$$

The eq. C.2 is a linear combination of the equations derived from eq. C.1, thus, does not contribute to a unique solution. However, we know  $\varepsilon_M$  and the total number of events ( $N_{events}$ ) which yield an expression for the number of inefficient events ( $N_0^*$ ):

$$N_0^* = N_{events}(1 - \varepsilon_M) \quad (C.3)$$

Assuming that the maximal number of true pad-multiplicity is 4, we need to solve the following equation system:

$$N_4^* = N_4 \varepsilon_h^4 \quad (C.4)$$

$$N_3^* = [N_3 + 4N_4(1 - \varepsilon_h)] \varepsilon_h^3 \quad (C.5)$$

$$N_2^* = [N_2 + 3N_3(1 - \varepsilon_h) + 6N_4(1 - \varepsilon_h)^2] \varepsilon_h^2 \quad (C.6)$$

$$N_1^* = [N_1 + 2N_2(1 - \varepsilon_h) + 3N_3(1 - \varepsilon_h)^2 + 4N_4(1 - \varepsilon_h)^3] \varepsilon_h \quad (C.7)$$

$$N_0^* = \sum_{m=1}^4 N_m (1 - \varepsilon_h)^m \quad (C.8)$$

Solution:

$$\text{eq. C. 5: } N_3^* = N_3 \varepsilon_h^3 + 4N_4 \varepsilon_h^3 - 4 \underbrace{N_4 \varepsilon_h^4}_{N_4^*}$$

$$\Rightarrow N_3^* + 4N_4^* = (N_3 + 4N_4) \varepsilon_h^3 \quad (C.9)$$

$$\text{eq. C. 6: } N_2^* = (N_2 + 3N_3 + 6N_4) \varepsilon_h^2 - 3 \underbrace{(N_3 + 4N_4) \varepsilon_h^3}_{N_3^* + 4N_4^*} + 6 \underbrace{N_4 \varepsilon_h^4}_{N_4^*}$$

$$\Rightarrow N_2^* + 3N_3^* + 6N_4^* = (N_2 + 3N_3 + 6N_4) \varepsilon_h^2 \quad (C.10)$$

$$\text{eq. C. 7: } N_1^* = [N_1 + 2N_2 - 2N_2 \varepsilon_h + 3N_3(1 - 2\varepsilon_h + \varepsilon_h^2) + 4N_4(1 - 3\varepsilon_h + 3\varepsilon_h^2 - \varepsilon_h^3)] \varepsilon_h$$

$$= (N_1 + 2N_2 + 3N_3 + 4N_4) \varepsilon_h - 2 \underbrace{\varepsilon_h^2 (N_2 + 3N_3 + 6N_4)}_{N_2^* + 3N_3^* + 6N_4^*} + 3 \underbrace{(N_3 + 4N_4) \varepsilon_h^3}_{N_3^* + 4N_4^*} - 4 \underbrace{N_4 \varepsilon_h^4}_{N_4^*}$$

$$\Rightarrow N_1^* + 2N_2^* + 3N_3^* + 4N_4^* = (N_1 + 2N_2 + 3N_3 + 4N_4) \varepsilon_h \quad (C.11)$$

$$\text{eq. C. 8: } N_0^* = N_1 - N_1 \varepsilon_h + N_2 - 2N_2 \varepsilon_h + N_2 \varepsilon_h^2 + N_3 - 3N_3 \varepsilon_h + 3N_3 \varepsilon_h^2 - n_3 \varepsilon_h^3 + N_4 - 4N_4 \varepsilon_h + 6N_4 \varepsilon_h^2 - 4n_4 \varepsilon_h^3 + N_4 \varepsilon_h^4$$

$$= \underbrace{N_4 \varepsilon_h^4}_{(i)} - \underbrace{(N_3 + 4N_4) \varepsilon_h^3}_{(1)} + \underbrace{(N_2 + 3N_3 + 6N_4) \varepsilon_h^2}_{(2)} - \underbrace{(N_1 + 2N_2 + 3N_3 + 4N_4) \varepsilon_h}_{(1)} + (N_1 + N_2 + N_3 + N_4)$$

$$\Rightarrow N_0^* - (N_1 + N_2 + N_3 + N_4) = N_4^* - (N_3^* + 4N_4^*) + (N_2^* + 3N_3^* + 6N_4^*) - (N_1^* + 2N_2^* + 3N_3^* + 4N_4^*)$$

$$= -N_1^* - N_2^* - N_3^* - N_4^*$$

$$\Rightarrow N_{events} = N_1 + N_2 + N_3 + N_4 \quad (C.12)$$

Eq. C. 12 is the underlying assumption.

We define the parameters  $C_1, C_2, C_3,$  and  $C_4$  using the measurables  $\{N_i^*\}$  as follows:

$$C_4 = N_4^*$$

$$C_3 = N_3^* + 4N_4^*$$

$$C_2 = N_2^* + 3N_3^* + 6N_4^*$$

$$C_1 = N_1^* + 2N_2^* + 3N_3^* + 4N_4^*$$

Using eqs. C. 4, 9 – 12 we get system of linear equations:

$$\text{Eq. C. 4 : } C_4 = N_4 \varepsilon_h^4$$

$$\text{Eq. C. 9 : } C_3 = (N_3 + 4N_4) \varepsilon_h^3$$

$$\text{Eq. C. 10: } C_2 = (N_2 + 3N_3 + 6N_4) \varepsilon_h^2$$

$$\text{Eq. C. 11: } C_1 = (N_1 + 2N_2 + 3N_3 + 4N_4) \varepsilon_h$$

$$\text{Eq. C. 12: } N_{events} = N_1 + N_2 + N_3 + N_4$$

These equations yield a simple linear equation:

$$N_{events} \varepsilon_h^4 - C_1 \varepsilon_h^3 + C_2 \varepsilon_h^2 - C_3 \varepsilon_h + C_4 = 0$$

Its solution yields the values for  $\varepsilon_h$ , and  $N_1, N_2, N_3,$  and  $N_4$ .

## The probability of a hit to have an additional multiplicity due to the detector's response

Let  $\nu_i$  be the number of events with the intrinsic pad-multiplicity  $i$  that is originating only from the interaction of the beam's particle and the detector's material, and  $\mathcal{E}_i$  be the probability of a hit to have  $i$  additional pad-multiplicity due to the detector's response. The following equations express the relations between these parameters:

$$N_1 = \nu_1 \mathcal{E}_0$$

$$N_2 = \nu_2 \mathcal{E}_0^2 + \nu_1 \mathcal{E}_1$$

$$N_3 = \nu_3 \mathcal{E}_0^3 + 2\nu_2 \mathcal{E}_0 \mathcal{E}_1 + \nu_1 \mathcal{E}_2$$

$$N_4 = \nu_4 \mathcal{E}_0^4 + 3\nu_3 \mathcal{E}_1 \mathcal{E}_0^2 + \nu_2 (2\mathcal{E}_2 \mathcal{E}_0 + \mathcal{E}_1^2) + \nu_1 \mathcal{E}_3$$

Thus:

$$\mathcal{E}_0 = \frac{N_1}{v_1}$$

$$\mathcal{E}_1 = \frac{N_2}{v_1} - \frac{v_2}{v_1} \mathcal{E}_0^2$$

$$\mathcal{E}_2 = \frac{N_3}{v_1} - 2 \frac{v_2}{v_1} \mathcal{E}_0 \mathcal{E}_1 - \frac{v_3}{v_1} \mathcal{E}_0^3$$

$$\mathcal{E}_3 = \frac{N_4}{v_1} - \frac{v_2}{v_1} (2\mathcal{E}_2 \mathcal{E}_0 + \mathcal{E}_0^2) - 3 \frac{v_3}{v_1} \mathcal{E}_1 \mathcal{E}_0^2 - \frac{v_4}{v_1} \mathcal{E}_0^4$$

The input parameters that go in to the digitization stage are  $\mathcal{E}_h$ ,  $\mathcal{E}_0$ ,  $\mathcal{E}_1$ ,  $\mathcal{E}_2$ , and  $\mathcal{E}_3$ .